Fabrication, architecture design, and characterization of a new Al/graphite flakes (Gf) composite used for thermal management

Zhengyan Shen

▶ **To cite this version:**

Zhengyan Shen. Fabrication, architecture design, and characterization of a new Al/graphite flakes (Gf) composite used for thermal management. Material chemistry. Université de Bordeaux, 2020. English. NNT : 2020BORD0268 . tel-03904596

HAL Id: tel-03904596

https://theses.hal.science/tel-03904596

Submitted on 17 Dec 2022

THÈSE PRÉSENTÉE POUR OBTENIR LE GRADE DE

DOCTEUR DE L'UNIVERSITÉ DE BORDEAUX

ÉCOLE DOCTORALE DES SCIENCES CHIMIQUES (SC)

SPÉCIALITÉ : Physico-chimie de la matière condensée

Par Zhengyan SHEN

Fabrication, architecture design, and characterization of a new Al/graphite flakes (G_f) composite used for thermal management

---

Sous la direction de : Jean-François SILVAIN et Gang JI

Soutenue le 16 décembre 2020 à 10h

Membres du jury :

M. Mario MAGLIONE	Directeur de recherche CNRS, ICMCB (Bordeaux)	Président
Mme. Anne JOULAIN	Professeur, Université de Poitiers	Rapporteure
M. Pierre-Marie GEFFROY	Chargé de recherche CNRS, IRCER (Limoges)	Rapporteur
Mme. Amélie VEILLERE	Maître de conférences, Bordeaux INP	Examinatrice
M. Gang JI	Chargé de recherche CNRS, UMET (Lille)	Examinateur
M. Yongfeng Lu	Professor, University of Nebraska Lincoln	Examinateur
M. Jean-François SILVAIN	Directeur de recherche CNRS, ICMCB (Bordeaux)	Invité

Abstract

In the microelectronic industry, the ever increase in power density due to miniaturization of electronic components requires heat sink materials with a high thermal conductivity (TC), a low coefficient of thermal expansion (CTE), and specific mechanical properties (MP). Pure metals, such as Al and Cu, have been previously used. However, they have limited TCs (e.g. 240 W/m.K for Al) and their CTEs are too high (e.g. 23×10^{-6}/K for Al), being incompatible with those of electronic components (e.g. 4×10^{-6}/K for Si), leading to failures in service due to thermal fatigue. Regarding this, metal matrix composites have been proven to be promising material where carbon materials, such as graphite, diamond, and carbon fibres, have been introduced as reinforcements because of their excellent thermal properties (i.e. very high TC and low CTE). In this Ph.D. project, Al matrix composites reinforced with low-cost and easily machinable graphite flakes (hereafter called Al/G_f composite) were developed with the aim to maximize TCs, tailor CTEs close to 6×10^{-6}/K, as well as improve MPs.

The intrinsic TCs of G_f are highly anisotropic, i.e. in-plane TC of 1000 W/m.K and out-of-plane TC of 5-10 W/m.K, respectively. It is thus clear that the strong orientation of G_f in the Al matrix ensures the high TCs, along the direction of graphite plane, in the as-produced composite. In this study, a new approach to combining flake powder metallurgy with a step-by-step powder filling process was successfully applied to achieve this conventional 1D arrangement. As such, the highest TC values theoretically predicted can be achieved experimentally. Further, the 2D and 3D arrangements of G_f were made using specifically designed punches in order to tailor the anisotropic CTEs of G_f (i.e. in-plane CTE of -1×10^{-6}/K and out-of-plane CTE of 28×10^{-6}/K), being unavailable in the 1D arrangement. The 2D arrangement allows to achieve the reduced CTEs being compatible with those of the substrate materials while maintaining a high TCs, demonstrating the strong potential for applications. Finally, the efforts were devoted to strengthen the Al matrix by integrating dispersed (ex-situ) SiC and (in-situ) TiB_2 nanoparticles to improve the overall MPs of the Al/G_f composites.

Keywords: Aluminium, graphite flakes, architecture, thermal conductivity, coefficient of thermal expansion, mechanical properties.

Résumé

Dans l'industrie microélectronique, l'augmentation constante de la densité de puissance due à la miniaturisation des composants électroniques nécessite un matériau de dissipation thermique ayant une conductivité thermique élevée (CT), un faible coefficient de dilatation thermique (CTE) et des propriétés mécaniques (PM) appropriées pour une dissipation efficace de la chaleur. Des métaux purs, tels que Al et Cu, ont déjà été utilisés. Cependant, ils ont des CT limitées (ex. 240 W/m.K pour Al) et leurs CTE sont trop élevés (ex. 23 10^{-6}/K pour Al), ce qui est incompatible avec ceux des composants électroniques (ex. 4 10^{-6}/K pour Si), conduisant à une défaillance en service due à la fatigue thermique. À cet égard, les composites à matrice métallique se sont révélés être un matériau prometteur. Les matériaux en carbone, comme le graphite, le diamant et la fibre de carbone, ayant été introduits comme renforts en raison de leurs excellentes propriétés thermiques (c'est-à-dire un CT très élevé et un faible CTE) dans une matrice Al. Dans ces travaux de thèse, des matériaux composites à matrice en Al renforcé par des plaquettes de graphite peu coûteuses et facilement usinables (ci-après appelé composite Al/G_f) ont été développés dans le but de maximiser le CT, d'adapter le CTE proche de 6 10^{-6}/K, ainsi que d'améliorer les PM.

La CT intrinsèque du G_f est hautement anisotrope, c'est-à-dire 1000 W/m.K dans le plan et 5-10 W/m.K hors du plan. Il est donc clair que la bonne orientation de Gf dans la matrice d'Al assure un CT élevée, dans la direction du plan du graphite, ainsi qu'à l'échelle du matériau produit dans cette même direction. Dans cette étude, un procédé de remplissage des poudres étape par étape, a été appliquée avec succès afin d'obtenir cet arrangement 1D conventionnel. Ainsi, les valeurs de CT théoriques prévues les plus élevées peuvent être atteintes expérimentalement. En outre, les matériaux composites 2D et 3D de G_f ont été élaborés à l'aide de pistons spécialement conçus afin d'adapter le CTE anisotrope des G_f (c'est-à-dire -1 10^{-6}/K dans le plan et 28 10^{-6}/K hors plan). La structure 2D permet de réduire la CTE, qui est alors compatible avec celui du matériau du substrat (voisin de 8 10^{-6}/K), tout en maintenant une CT élevée. Enfin, les efforts ont été consacrés à renforcer la matrice Al en intégrant des nanoparticules dispersées (ex-situ) de SiC et (in-situ) de TiB_2 pour améliorer les PM globales du composite Al/G_f.

Mots clés : Aluminium, graphite en plaquette, architecture, conductivité thermique, coefficient de dilatation thermique, propriétés mécaniques.

Acknowledgements

The PhD work presented has been performed with collaboration between the Institute de Chimie de la Matière Condensée de Bordeaux (ICMCB) and Unité Matériaux et Transformations (UMET, Université de Lille). First and foremost, I would like to thank my French and Chinese advisors, Dr. Jean-François SILVAIN and Dr. Gang Ji, for their patient careful and continual guidance.

I would like to thank the members of my thesis committee, particularly, Pr. Anne and Dr. Pierre-Marie, for their time and dedication to this thesis.

I would like to thank Pr. Jean-Luc Battaglia from I2M in Bordeaux for his thermal characterization to this PhD work, as well as Christine Labrugere from Placamat for her XPS analysis.

I would also like to thank Viraphong Oudomsack and Guillaume Bertrand for their great technical support and mold machining work.

Thanks to the members of group 4 in ICMCB, I am happy to have had the opportunity to work with them. Special thanks go to Maël, Benjamin, Jonathan, Adrien, Nabil, Antoine, Alexandre, and Iñaki for the mutual guidance and helps.

I gratefully acknowledge the China scholarship council for the financial support.

Lastly, I would like to thank my family and friends.

Résumé des travaux de thèse

Dans l'industrie microélectronique, l'augmentation constante de la densité de puissance, due à la miniaturisation des composants électroniques, nécessite des matériaux de dissipation thermique ayant 1) une conductivité thermique (CT) élevée, 2) un faible coefficient de dilatation thermique (CTE) et 3) des propriétés mécaniques appropriées (PM) spécifiques. Des métaux purs, tels que l'aluminium (Al) et le cuivre (Cu), sont déjà été utilisés pour ce type d'application. Cependant, ils ont des CT limitées (ex. 240 W/mK pour Al) et leurs CTE sont trop élevés (ex. 23 10^{-6}/K pour Al), ce qui est incompatibles avec ceux des composants électroniques (ex. 4 10^{-6}/K pour Si), pouvant conduire à une défaillance en service due à la fatigue thermique. À cet égard, les composites à matrice métallique se sont révélés être des matériaux prometteurs. Des matériaux en carbone, comme le graphite, le diamant et la fibre de carbone, peuvent être utilisés comme renforts en raison de leurs excellentes propriétés thermiques (forte CT et faible CTE). Dans ces travaux de thèse, un composite à matrice Al renforcée par des plaquettes de graphite peu coûteuses et facilement usinables (ci-après appelé composite Al/G_f) a été développé dans le but de maximiser la CT, d'adapter le CTE à une valeur proche de 6 10^{-6}/K, ainsi que d'améliorer les PM.

Les composites à matrice Al/G_f ont été fabriqués par pressage à chaud sous vide. Il a été rapporté que le G_f présente une CT élevée dans le plan basal d'environ 1000 W/mK, alors que la CT perpendiculaire à ce plan est de l'ordre de 5-10 W/mK. Il présente également une anisotropie élevée en CTE (-1 10^{-6}/K dans le plan, 28 10^{-6}/K hors plan). Par conséquent, l'orientation de la G_f est importante dans la fabrication du composite afin d'obtenir une CT élevée dans le plan perpendiculaire à la direction de densification. Le processus de remplissage et de pressage de la poudre a été considéré comme une étape importante afin d'optimiser l'orientation de la G_f. L'utilisation de poudre d'Al (Al_F) en plaquettes s'est avérée efficace afin d'obtenir une orientation contrôlée et uniforme des G_f et ceci pour un remplissage des moules de densification en une seule étape. Toutefois, cette méthode ne convenait pas pour la poudre d'Al sphérique (Al_S), car un mauvais alignement de G_f était toujours constaté dans le composite (ex. figure 1a). La raison principale est que la poudre d'Al_S, qui présente une densité apparente beaucoup plus élevée que celle de la poudre d'Al_F, a une compressibilité moindre après application d'une pression uniaxiale. Ainsi, la distribution aléatoire de G_f, dans le composite final, est supérieure pour les poudres d'Al sphérique par rapport aux poudres plaquettes. Afin d'éviter la distribution aléatoire de G_f, l'épaisseur de la

couche de poudre Al + G_f, pendant le remplissage du moule, doit être contrôlée. Par conséquent, une méthode de remplissage de poudre étape par étape a été développée pour obtenir l'orientation élevée de G_f dans la matrice Al_S, comme le montre la figure 1b. Il faut noter que cette méthode convient également à la poudre Al_F. Le degré d'orientation <cos2θ> de G_f, obtenu par analyse d'image, a atteint 0,94, ce qui est identique à celui du composite Al/G_f préparé avec des poudres Al en plaquettes.

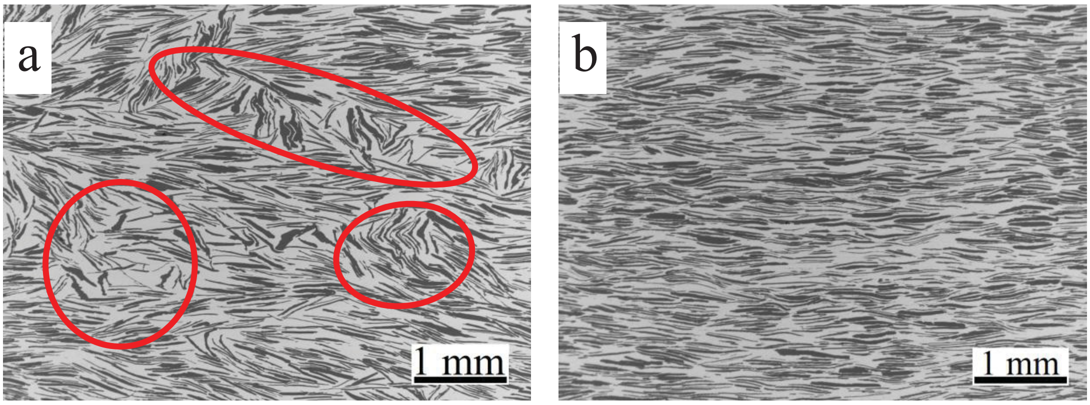

Figure 1 : Micrographies au MEB des composites Al_S/40 % vol. G_f en utilisant (a) la méthode de chargement de poudre en une étape et (b) la méthode de chargement de poudre étape par étape.

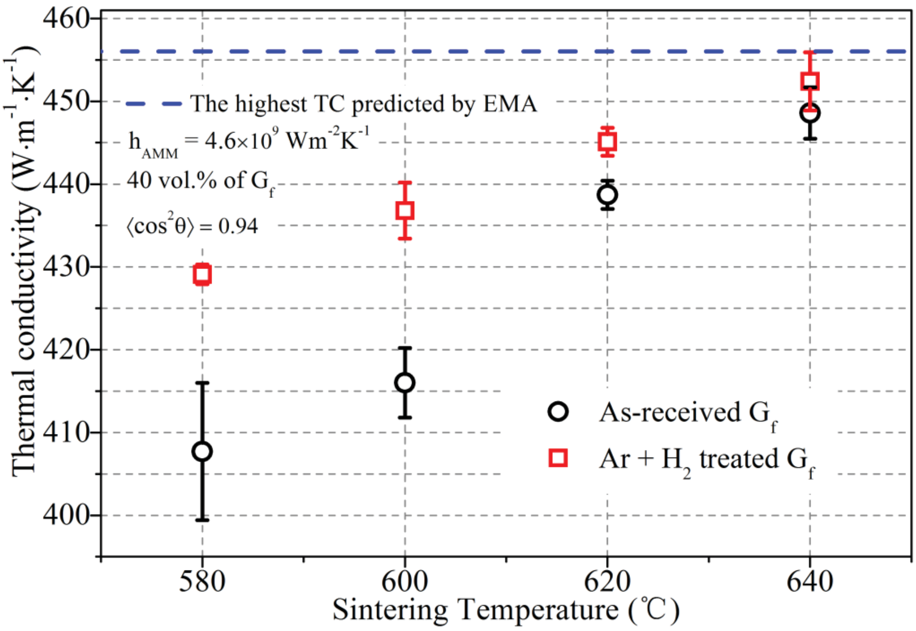

Figure 2 : CT des composites Al_S/40 % vol. G_f (tels que reçus et traités thermiquement avec Ar + H_2) frittés aux différentes températures de frittage de 580 °C, 600 °C, 620 °C et 640 °C.

En outre, comme le montre la figure 2, la CT, dans le plan du matériau composite Al/40 % vol. de G_f, augmente 1) avec la température de frittage jusqu'à 640 °C tout en maintenant le degré d'orientation élevé de G_f ($<\cos 2\theta> = 0{,}94$) et 2) en utilisant du G_f traité thermiquement avec $Ar+H_2$ dans les mêmes conditions de frittage. Le paramètre de réseau d_{002} de G_f reste constant après le traitement thermique $Ar+H_2$, ce qui signifie que la CT intrinsèque de G_f reste inchangée. L'analyse Raman montre que le nombre de défauts de structure sur le bord de G_f diminue après le traitement thermique. Les effets de l'augmentation de la température de frittage et de l'utilisation de G_f traitée sont attribués à l'amélioration de la conductance thermique interfaciale (ITC) entre la matrice Al et G_f. La CT la plus élevée du composite Al/40 % vol. G_f, fabriqué dans nos conditions optimisées, est voisine de 452 W/mK, ce qui est très proche de la CT la plus élevée (456 W/mK) théoriquement prévue par le modèle EMA.

Par convention, les matériaux composite Al/G_f, élaborés par métallurgie des poudres conventionnelle, est noté 1D. Il faut noter que ces matériaux composites présentent une anisotropie élevée tant en TC qu'en CTE, ce qui ne convient pas aux applications de dissipateurs thermiques. Le CTE le long de la direction à 45° a été mesuré. Nous avons proposé une nouvelle conception d'architecture (arrangements 2D ou 3D) de G_f dans la matrice Al et l'avons réalisée grâce à un nouveau procédé, qui combine la métallurgie des poudres en plaquettes, un piston de design spécifique et un procédé de remplissage de poudre étape par étape. Le processus de traitement est illustré à la figure 2. Une distribution en zigzag presque parfaite de G_f a été obtenue grâce à ce nouveau procédé, comme le montre la figure 3. Dans le plan 2D, les valeurs CTE ont été ajustées à 7-8 10^{-6}/K, comme indiqué dans le tableau 1, et la CT dans la direction perpendiculaire au plan 2D reste aussi élevée que la CT dans le plan 1D. Ce composite 2D convient à l'application de dissipateur thermique.

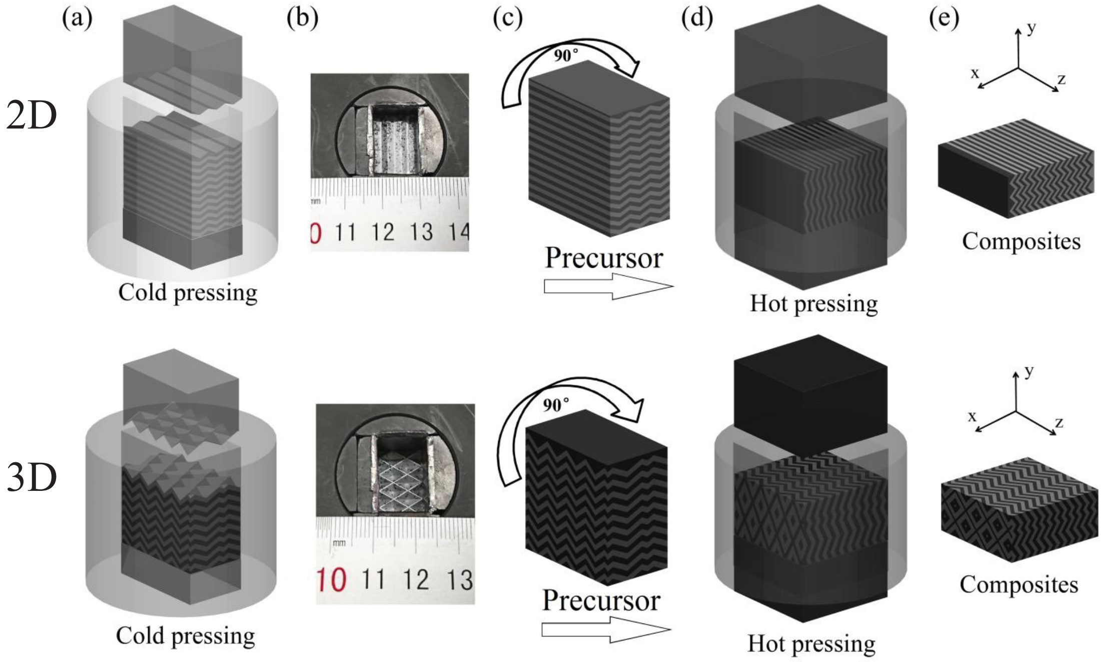

Figure 3 : Illustrations schématiques des procédés de fabrication pour acquérir les composites Al/G_f avec les arrangements 2D et 3D : (a) pressage à froid à l'aide de pistons spécialement conçus, (b) photographies de la morphologie de la couche de poudre après le pressage à froid, (c) le précurseur Al/G_f, (d) les moules en graphite utilisés pour le pressage à chaud, (e) les produits finaux.

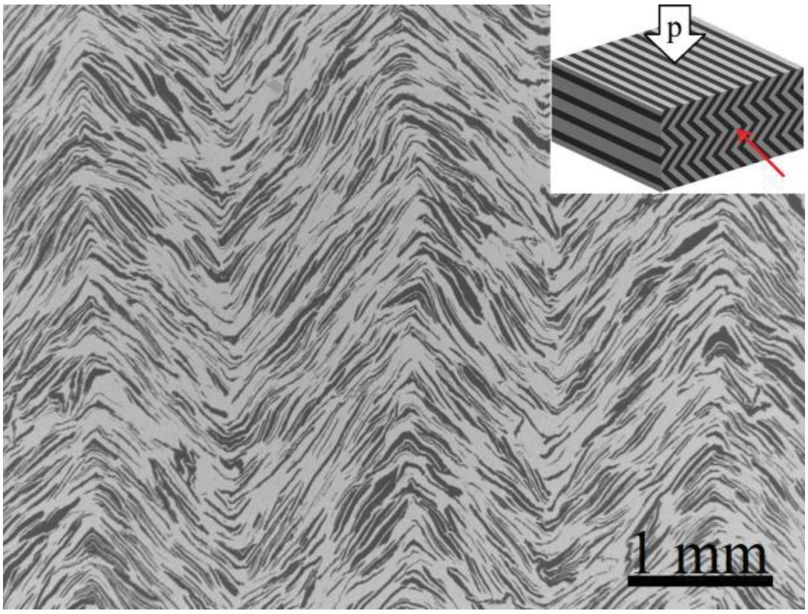

Figure 4 : Micrographie MEB des composites Al_F/40 % vol. G_f avec arrangement 2D de G_f.

Tableau 1 Comparaison des propriétés thermiques des composites Al/40 % vol. G_f entre les arrangements 1D et 2D (valeurs moyennes de CTE mesurées sur la plage de température de 50 °C - 150 °C).

	1D		2D		
CT (W m^{-1} K^{-1})	z,x: 431±6	y: 40±1	x: 81±1	y: 191±1	z: 437±3
CTE (10^{-6}/K)	z,x: 23; 45°: 6	y: -11	x: 7	y: 8	z: 22

D'autre part, nous avons également conçu un piston utilisé pour un arrangement 3D des G_f afin d'optimiser les propriétés thermiques dans les trois directions de l'espace. La figure 5 montre une vue typique du dessus et des deux côtés des composites Al_F/40 % vol.G_f fabriqués à l'aide d'un piston 3D. Les mesures de CTE et TC des composites 3D ont confirmé la réduction du degré d'anisotropie des propriétés thermiques par rapport aux matériaux composites 1D. Cela indique que les propriétés thermiques des composites Al/G_f dépendent fortement de la disposition de G_f à une fraction volumique donnée de G_f.

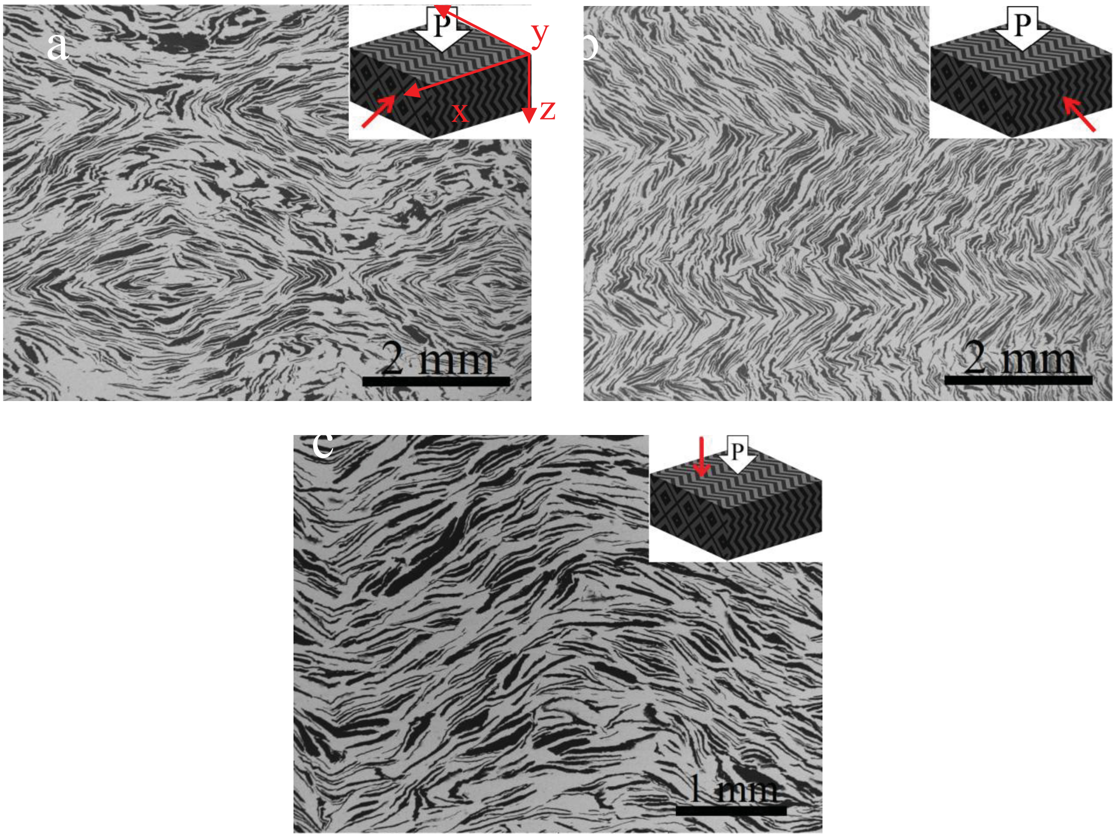

Figure 5 : Micrographies MEB des composites Al_F/40 % vol. G_f avec l'arrangement 3D de G_f : (a) vue de côté 1, (b) vue de dessus, et (c) vue de côté 2 ; les flèches dans les encarts indiquent la direction d'observation par rapport à la direction de pression

Bien que les composites Al/G_f aient montré des propriétés thermiques très prometteuses, leur faible résistance est encore le principal obstacle aux applications potentielles dans l'industrie de l'électronique. Trois stratégies, dont les voies ex-situ (nano-SiC), in-situ (nano-TiB_2) et bio-mimétique, ont été testées afin d'augmenter la résistance des composites Al/G_f. Le résultat de la voie ex-situ a montré que le nano-SiC est distribué en surface des poudres de la matrice Al autre qu'à l'intérieur des grains, et qu'il est difficile d'éliminer toutes les agglomérations de nano-SiC. Le nano-TiB_2 synthétisé in-situ est également confronté au problème de la ré-agglomération dans la matrice pendant le processus de traitement. Enfin, la métallurgie des poudres en plaquettes a été la méthode la plus efficace pour améliorer la résistance mécanique de la matrice Al, car elle forme la structure lamellaire unique. Comme le montre la figure 6, l'ajout de nanoparticules (SiC et TiB_2) dans la matrice Al_F diminue la résistance mécanique des matériaux composites Al/G_f.

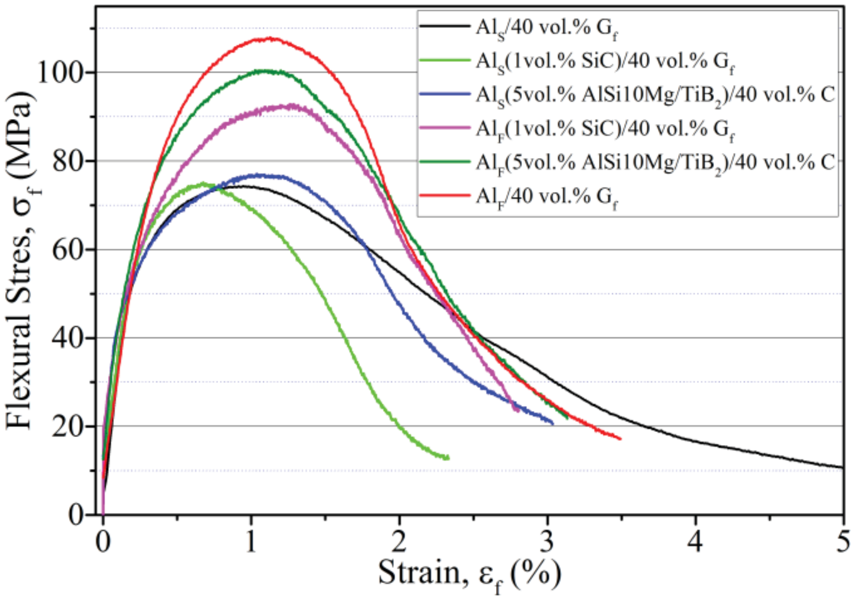

Figure. 6 : Courbes de contrainte en flexion des composites Al_S/40 % vol. G_f, (Al_S+1 % vol. SiC)/40 % vol. G_f, (Al_S+5 % vol. AlSi10Mg/TiB_2)/40 % vol. G_f, (Al_F +1 % vol. SiC)/40 % vol. G_f, (Al_F+5 % vol. AlSi10Mg/TiB_2)/40 % vol. G_f et Al_F/40 % vol. G_f.

Table of Contents

List of Figures

List of Tables

List of Abbreviations

TC	Thermal Conductivity
CTE	Coefficient of Thermal Expansion
CMOS	Complementary Metal Oxide Semiconductor
TIM	Thermal Interface Material
LED	Light Emitting Diode
Al/SiC	Silicon carbide reinforced aluminium composite
G_f	Graphite flake
CF	Carbon Fibre
MMCs	Metal Matrix Composites
VHP	Vacuum Hot Pressing
Al/G_f	Graphite flake reinforced aluminium composite
Cu/G_f	Graphite flake reinforced copper composite
XRD	X-Ray Diffraction
SEM	Scanning Electron Microscopy
EMA	Effective-Medium Approximation
ITC	Interfacial Thermal Conductance
DEM	Differential Effective Medium
AMM	Acoustic Mismatch Model
RAM	Resonant Acoustic Mixer

Chapter 1

Introduction and literature reviews

1.1 General introduction

1.1.1 Background

Various electronic devices have become one of the most important parts in our daily life. Dating back to 1946, the first programmable computer (ENIAC) was invented in University of Pennsylvania, which was supported by tens of thousands of vacuum tubes and had a computing capability of 5000 operations per second [1]. It did open the information age and have a profound influence on our modern life. However, since ENIAC had a large volume having a 15-by-9-metre cabinet and dissipated roughly 170 kilowatts, it was very necessary to remove heated air from computer room via some approaches, like air conditioning and ventilation. The need for thermal management of electronic parts was accompanied with the first generation of digital computer. In 1947, the bipolar was created at Bell Laboratories, which was smaller, lighter, and had a lower level operational power compared to vacuum tubes. As integrated circuit was invented in 1960's, the number of transistors per chip doubled approximately every two years, known as Moore's law, as demonstrated in Fig. 1.1 in its first published and recent version [2, 3]. However, Moore warned the removal of heat generated by electronic components would become a challenge as more and more transistors packed in a fixed area. As seen in Fig. 1.2, the heat flow of electronic device per area was increasing since 1960's and became a very large amount to 12 W/cm^2. During this period, an "attached microcooler" technology was developed to dissipate heat directly from the surface of chip. When complementary metal oxide semiconductor (CMOS) was coming into the electronic industry in 1990's, as it generated less heat at the same power level compared to bipolar, it was starting to replace the bipolar as mainstream. But, as the number of CMOS increased in the exponential way every 18 months, the heat flux became a challenge again as it reached to the same level as the bipolar did before two decades.

Generally, there are two major reasons that the generated heat by chips must be removed in order to keep it cool [4]. One is that the reliability of transistors is exponentially linked to the temperature of the junction. The relationship between operating temperature and failure rate of devices is given below:

$$f = A\varepsilon^{-e_A/kT} \tag{1.1}$$

where A is Arrhenius constant, f is failure rate, e_A is activation energy, k is Boltzmann's constant, T is junction temperature in K. It can be understood that the failure rate doubles for every 10 °C increase in temperature. On the other hand, the speed of the microprocessor is also dependent on the operating temperature. At a lower temperature, the gate delay can be reduced so as to enhance operating speeds, which also helps to decrease leakage power as well as overall power dissipation. In other words, the electronic devices should be operated at a temperature lower than 70 °C for the sake of both performance and reliability.

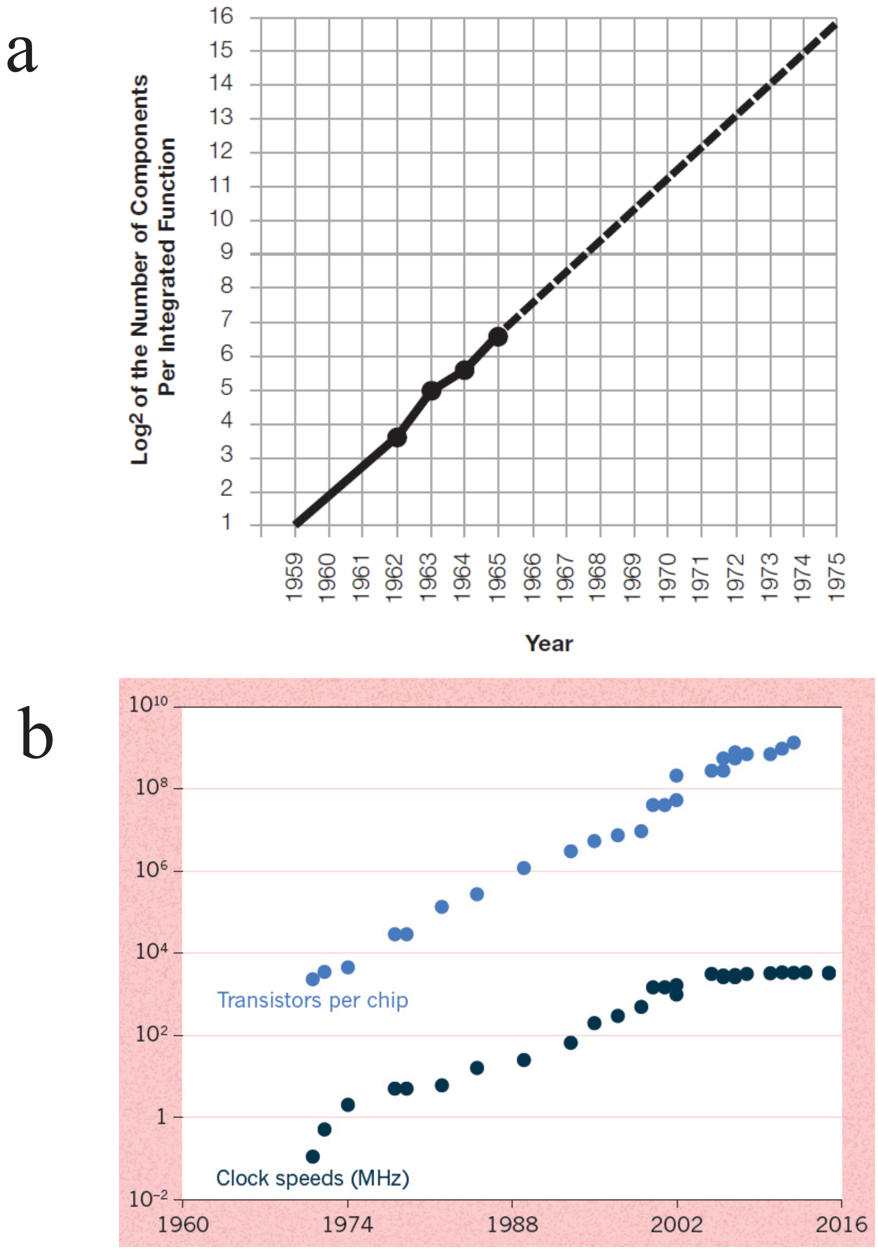

Fig. 1.1: Prediction of the number of components per integrated function versus year (Moore's law): (a) the original version [2] and (b) the recent one [3].

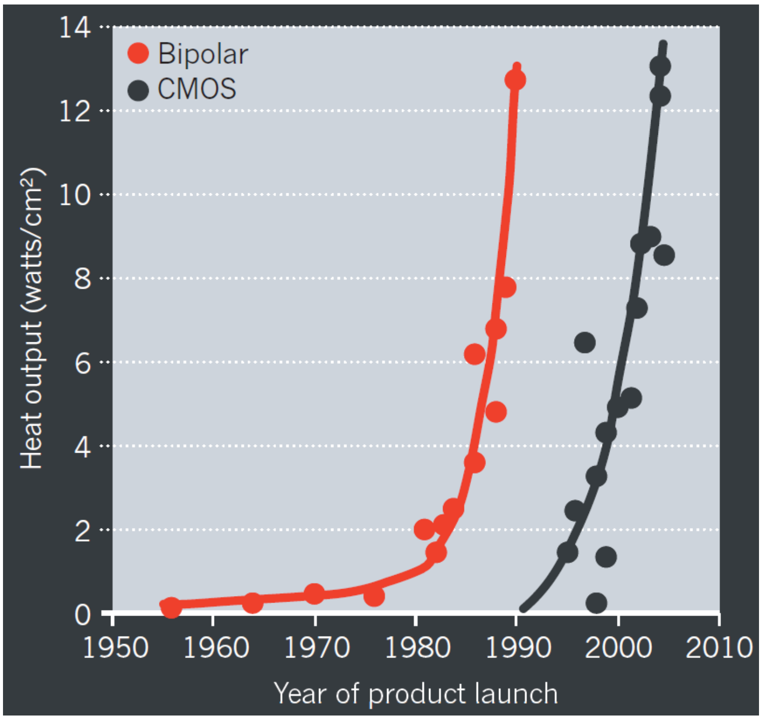

Fig. 1.2: Heat flux of bipolar and CMOS along the year [5].

The necessity of thermal management for electronic components is essentially based on the power dissipation per chip as its packaging density became higher and higher. For example, the power dissipation of CMOS devices is related to the capacitance of the logic elements, the square of the operation voltage swing, and the operating frequency, being expressed as the following equation [6].

$$P \approx NCV^2f \tag{1.2}$$

where P is the power dissipation of CMOS, N is the number of transistors per chips, C is the capacitance of the logic elements, V is the operating voltage, and f is the operating frequency. The capacitance of logic element decreases with feature size of transistor, and operating voltages was significantly depressed. Thus, the boosting in the number of transistors per chip and the clock frequency has been the major driving force for the development of microprocessors before 2005. However, when the power dissipation reached around 100W/chips, the air-cooled technique was unable to maintain the proper operating ambiance. Consequently, clock frequency had to be stabilized at around 3 GHz. Meanwhile, a multi-core processor was introduced as a compromise solution to hold the power increase and continue to improve chip performance. Apparently, the challenge of heat removal from electronic devices has been a major barrier in pursuing the high-performance chip.

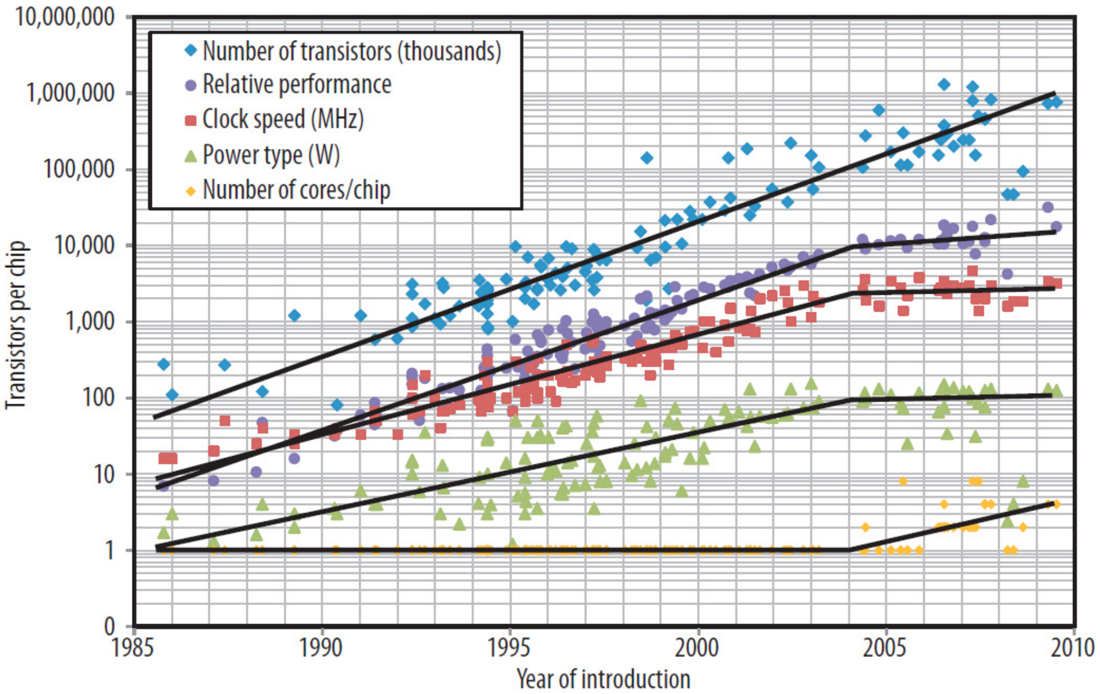

Fig. 1.3: The evolution of transistors, frequency, power, performance, and processor cores over time [7].

In order to satisfy the thermal management requirement, various types of cooling techniques have been developed to control temperature in computers. At module-level cooling, air cooled heat sink and water-cooled cold plate are common techniques used to transfer heat via conduction. For most of high-performance personal microprocessors, two types of electronic packaging were commonly used to meet the need for cooling, as presented in Figure 1.4. The silicon (Si) chip is bonded to the heat sink with a thermal interface material (TIM) (Fig. 1.4a). In the other type, an integrated heat spreader is attached to the die by TIM, and the heat sink to the chip through another TIM. The first architecture is usually seen in laptops, and the other one is used for desktop and server application. When the computer is working, the air fan continues to blow the cold air to the heat sink, and the generated heat in the chip can be efficiently transported to local environment through heat sink or heat spreader and air.

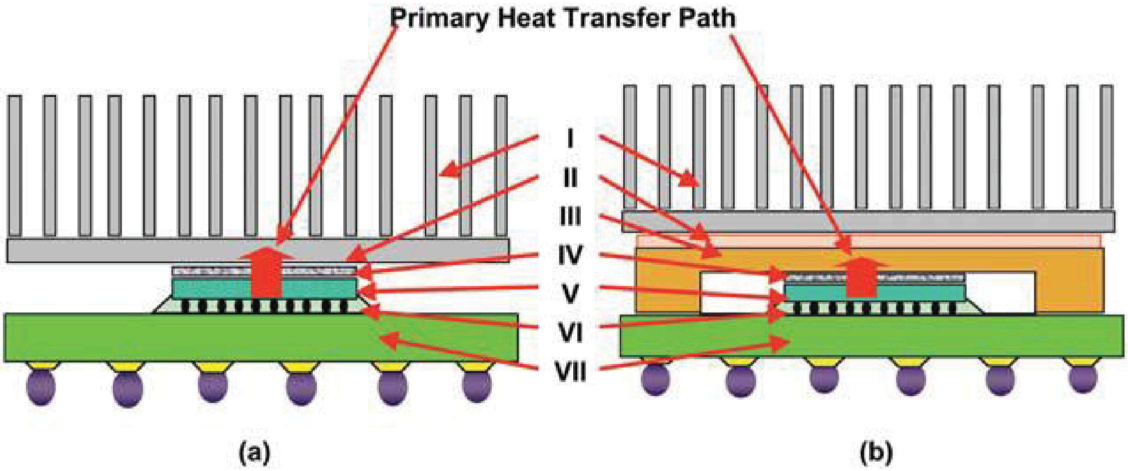

Fig. 1.4: Schematic illustration of the two thermal architectures: (a) typically used in laptop; (b) typically used in desktop and server applications. I heat sink; II TIM; III IHS; IV TIM; V silicon die; VI underfill; and VII package substrate [8].

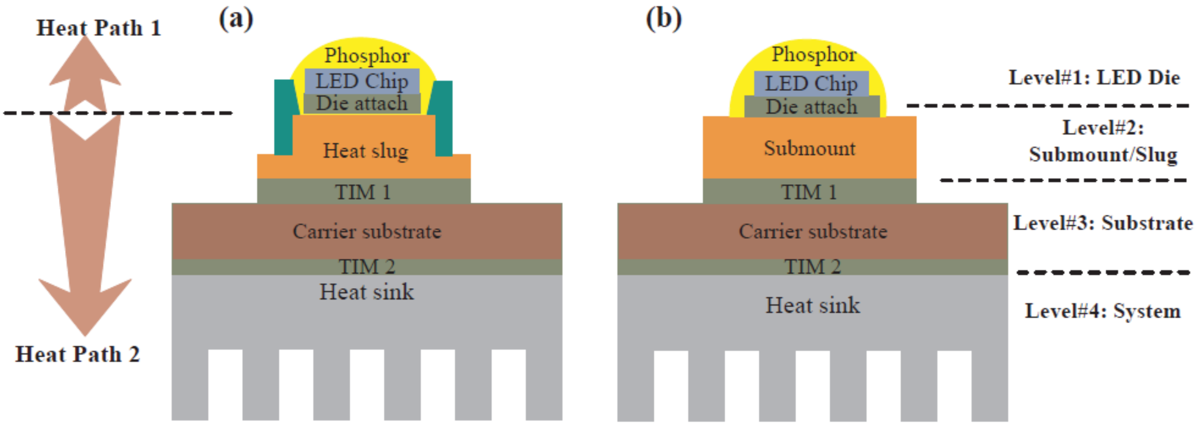

Fig. 1.5: Two thermal architectures of LED module [9].

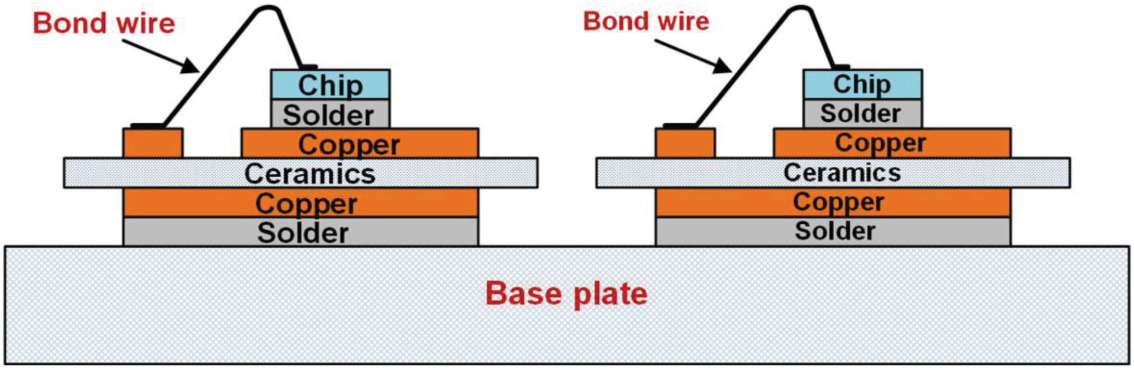

Fig. 1.6: Multilayer structure of power electronic module [10].

Similarly, thermal architecture is also applied in Light-emitting diode (LED) or power electronic modules to enable a proper operating temperature as shown in Figs. 1.5 and 1.6, respectively. Indeed, the heat dissipation ability of the package is dominated by the intrinsic thermal conductivity (TC) of different layers and overall thermal resistance. Among pure metals, copper (Cu) and aluminium (Al) have been used as heat spreaders or heat sinks because they have relatively high TCs. However, thermo-mechanical stress always occurs when layers with different coefficient of thermal expansion (CTE) attach together and undergo thermal changes, which is known as CTE mismatch. Especially, after the long period of thermal cycling, difference in CTEs would cause serious thermal failures as well as affect the normal function of electronic devices. Thermal failures in electronic modules are usually happened in the form of mechanical separating, such as bond wire lift off (Fig. 1.7a) and crack (Fig. 1.7b). To solve this problem, the selected electronic package materials must have the CTEs matching those of the substrate materials or semiconductors.

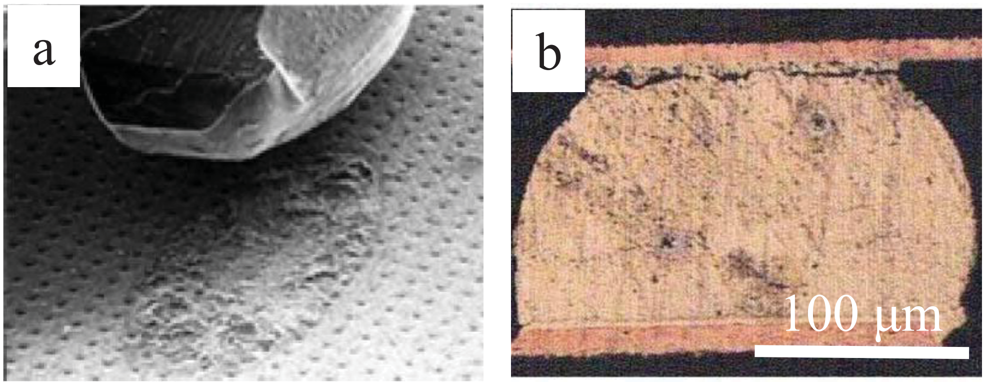

Fig. 1.7: Typical thermal failures in electronic component: (a) Bond wire life off (SEM image, 40×) [11], (b) solder bond crack [12].

1.1.2 Motivation and objectives

Based on our above discussion, the candidate materials used as heat sink should have both high TC and tailored CTE values. As mentioned before, Cu and Al have the high TCs, while they have the high CTEs compared with that of Si chip (4×10^{-6}/K), one of the major materials used as semiconductor. As an alternative, copper-tungsten and copper-molybdenum with relatively low CTE values ($6 - 8 \times 10^{-6}$/K) were previously used to decrease the CTE mismatch, but such materials have the high density and relatively low TC. Later, the Al matrix composite reinforced with silicon carbide (SiC) particles (i.e. Al/SiC composite) was introduced as heat spreader material, and it offered the light weight and low CTE, but its TC was not much improved compared to that of pure Al. Facing the continuing increase of heat density of electronic devices, it is still imperative to develop new materials to meet all the requirements for the effective thermal management. Recently, researchers were going to investigate metal matrix composite materials, which offer the potential for good control over the combinations of properties.

In ICMCB, several metal matrices have been studied, such as Ag, Cu, and Al, whose physical properties are given in the **Table 1.1**. Compared with Cu and Ag, Al offers low price, abundant resource in nature, light weight, and relative high TC. It is more favorable to be used in the applications of automobile or aerospace industries. Thus, it was selected as matrix to be investigated in this study. Besides, carbon materials, such as diamond (D), carbon fibre (CF), graphite flake (G_f), carbon nanotube (CNT), and graphene (G) have been used as reinforcements to improve the thermal properties of composite materials due to their attractive thermal properties (see **Table 1.2**). For example, the TC of D with sp^3 bonds is four or five times higher than that of pure Cu. And the other carbon materials, like G_f, G, with sp^2 bonds also have the TCs much higher than that of pure Cu. As one type of natural graphite, G_f is produced from mining followed by crushing, milling, and separating. Low price is one of the major advantages of G_f compared with D or CF. G_f also has excellent thermal performance and good machinability. As the cost of thermal management is continuing to increase in the electronic industry, G_f became a promising reinforcement candidate to be extensively studied. Therefore, it was selected as reinforcement in this work.

Table 1.1 Physical properties and cost of Selected metal matrices studied in ICMCB

Matrices	TC(W/m K)	CTE(10^{-6}/K)	Density(g/cm^3)	Price (€/Kg)
Ag	420	20	10.5	400
Cu	400	17	8.9	3.4
Al	220	23	2.7	1.3

Indeed, metal matrix composites (MMCs) reinforced with various carbon materials have been proved to be an effective approach to reach the goal of acquiring high TC and tailorable CTE in the past decades [13]. The typical thermal properties and microstructure configuration of Al matrix reinforced different micrometric carbon reinforcements are illustrated in Fig. 1.8. D reinforced Al composites show excellent thermal properties, and the other Al/C composites show high in-plane thermal conductivity. However, considering the practice electronic needs, not all of them are desirable. For instance, Al/D composite materials are hard to be machined and have high cost because of its nature and high price. The other two types of Al/C (CF, Fig

1.8a and G_f, Fig 1.8b) composites show the low through-plane TCs. Many efforts have been done in ICMCB in order to optimize the thermal properties of the composite materials, including using semi-liquid process to tailor the interface between the matrix and reinforcement, applying uniaxial pressure to align the CF or G_f, and adding CF into the Al/G_f to improve the in-plane CTE. However, the undesirable through-plane TC is still an issue for Al/G_f (CF) composite materials. Fortunately, there is still one parameter that is interesting to be studied, which is how to control orientation of anisotropic carbon reinforcement (CF and G_f) and has potential to tailor the through-plane thermal properties.

Table 1.2 Physical properties and cost of carbon reinforcements studied in ICMCB

Reinforcements	TC(W/m K)	CTE(10^{-6}/K)	Density(g/cm^3)	Price (€/Kg)
Diamond	1500-3000	1.0	3.1	200-2000
Carbon fiber	//: 600 ⊥:10	//: -1 ⊥: 25	2.25	30-400
Graphite flake	//:1000 ⊥:10	//: -1 ⊥: 28	2.26	1-10
Carbon nanotube	//:1000 ⊥:10	//: -1	1.6-1.8	500 - 2500
Graphene	～ 2000	-1	1.6-1.8	2000

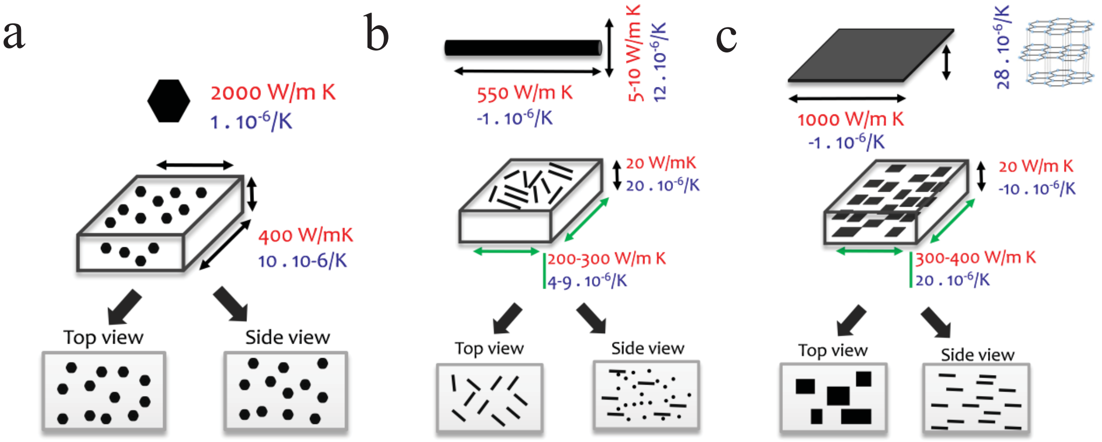

Fig. 1.8: Schematic microstructures and thermal properties of Al/C composite materials reinforced with micrometric reinforcements fabricated in ICMCB, (a) Diamond, (b) Short carbon fibre, (c) Graphite flake.

The objectives of this work were to develop the low cost Al/G_f composite materials having features of high TC, tailorable CTE, light weight, and medium strength. We also wanted to develop a simple process to control the orientation of C reinforcements in the matrix, which can be applicable for all type of anisotropic reinforcements or metallic matrices. This process would have potential to fabricate fully isotropic composite materials reinforced with anisotropic reinforcement that can be used as heat sink or spreader materials.

1.1.3 Outline of the dissertation

In this study, Al and G_f were selected as the metal matrix and reinforcement, respectively. The fabrication of Al/G_f composites was conducted by powder metallurgy using vacuum hot pressing (VHP). **Chapter 1** is the literature reviews providing the information about the background, advantages and limitations of the candidate materials, and points out the major issues and the objectives of this thesis work. **Chapter 2** introduces the optimization of processing parameters to achieve the highest TC of the Al/G_f composites and the effective powder filling method to obtain the high orientation of G_f. Architecture design of G_f is presented in detail in **chapter 3**, where a novel approach was developed to tailor thermal properties of the Al/G_f composites by engineering the distribution of G_f. **Chapter 4** focuses on strengthening the Al matrix by integrating dispersed (ex-situ) SiC and (in-situ) TiB_2 nanoparticles in order to improve overall mechanical properties of the Al/G_f composites. The last **chapter 5** is our general conclusions, and perspectives we would like to propose for future investigation.

1.2 Literature reviews

1.2.1 Production of Al and its powder

Pure Al is made from alumina (Al_2O_3); Al_2O_3 is extracted from bauxite [$(Al, Fe)_2O_32H_2O$] or from certain clays [$Al_2O_3.2SiO_2$] through Bayer process. The flow sheet of Bayer process is displayed in Fig. 1.9 [14]. The bauxite is crushed, mixed with cautic soda solution, and processed in a grinding mill to get slurry containing very fine particles. The slurry is heated to 110-270 °C under pressure to dissolve the Al_2O_3 as aluminate leaving behind a red mud containing iron oxides and other impurities. The aluminate solution is then seeded with hydroxide crystal for depositing this compound. The precipitation is carried out in cycles leaving behind a large amount of crystals to seed the next cycle. Finally, the hydroxide is calcined at 1100 °C to form waterless Al_2O_3. The obtained Al_2O_3 can be used to produce Al.

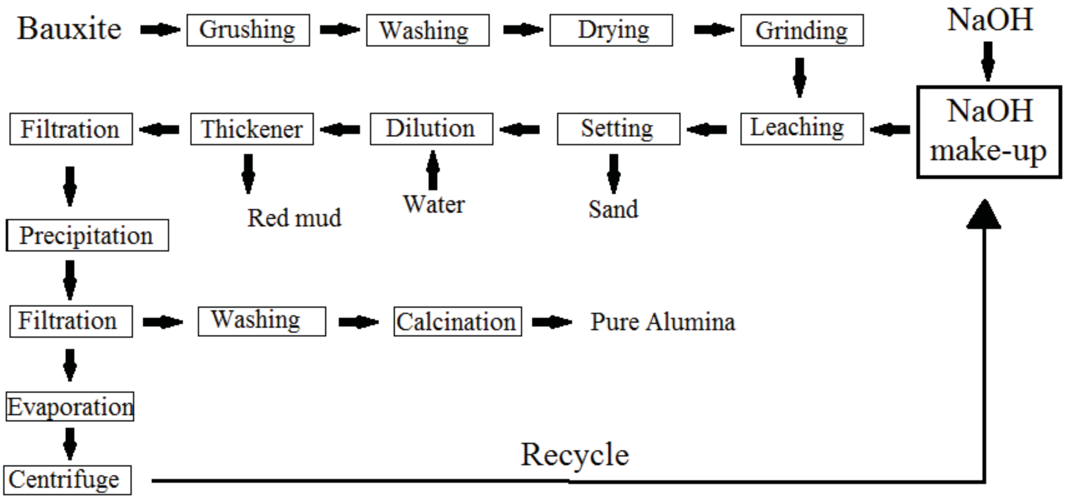

Fig. 1.9: Flow sheet of the Bayer process to produce pure Al_2O_3 [14].

The production of pure Al is implemented through the fused salt electrolysis in an electrolytic pot, which is known as the Hall-Heroult process. A carbon rod acts as the anode, and another type of carbon on the bottom of pot acts as cathode. Al_2O_3 is dissolved in molten cryolite at a temperature around 1770 °C to form an electrolyte solution that conducts the current from the one electrode to the other. The reaction of reducing Al_2O_3 can be given simply as follows:

Cathode reaction: $Al^{3+} + 3e^- \rightarrow Al$

Anodic reaction: $O^{2-} + C \rightarrow CO + 2e^-$

Overall reaction: $Al_2O_3 + 3C \rightarrow 2Al + 3CO$

When the direct current is passed through the solution, the oxygen in Al_2O_3 is released and reacted with carbon forming carbon oxide, and the freed Al atoms settle to the bottom of the pot at the molten state. It is a continuous process where fresh Al_2O_3 is added and the molten Al is siphoned off periodically [14]. For now, Al is the only metal refined electrolytically in a fused salt on an industrial scale.

The major production method of Al powder is gas atomization [15]. In this process, a jet of high-velocity gas is utilized to disintegrate the molten into droplets and form the powder. The atomizing gas is compressed air for the most of applications. Air atomization is possible to produce Al powder because the Al droplets form a thin oxide surface layer that avoids the further oxidation. Fig. 1.10 illustrates the production of metal powder by an up-draught atomizer [16]. Metal ingot is melted by induction heating in a graphite crucible at the atomizing temperature. The metal liquid is then transported into the atomizing nozzle by the flow of the high-pressure atomizing gas. As the metal melt meets the high velocity gas, it is broken up into droplets and sprayed as a jet. The droplets are solidified into powder particles by the cooling air in the chiller chamber. Finally, the powders are collected and classified by sieving into size ranges for the different applications.

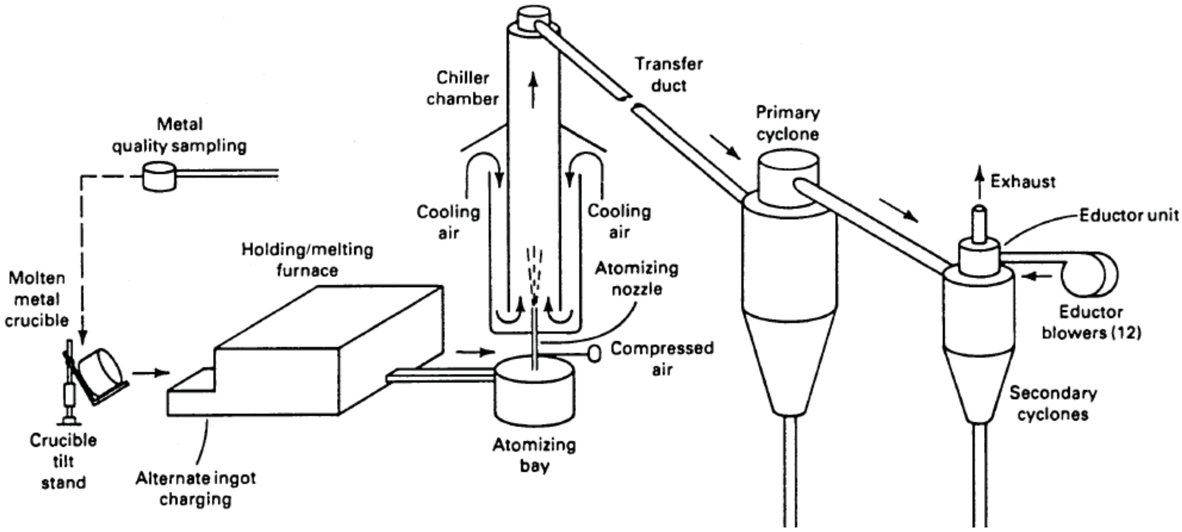

Fig. 1.10: Schematic diagram of a gas atomizer [16].

There are many process parameters that affect the size and morphology of the Al powders including gas pressure, gas types (air, nitrogen, argon, and helium), and the oxygen content in the gas [17]. For instance, higher pressure and/or a smaller jet distance generally result in finer particles [18]. Helium produces much finer powders than those produced by nitrogen and argon under similar fabrication conditions [19]. Air atomized powders with irregular shape show a larger specific surface than powders atomized in inert gas. Since the quenching effect of the gas jets is considerably less than that in water, the droplets formed during gas atomization of the liquid metal are more likely to convert into spherical shape before solidification. Above all, gas atomized Al powders are generally free of fine porosity, typically spherical type with relatively smooth surface, which means they have good compressibility, good flow characteristics, and lower sintering activities.

1.2.2 The development of metal (Al or Cu)/G_f composites

MMCs are recognized as combining two or three constituents to form a new multiphase material. In this way, it can to some extent suppress the limitation of each constituent. As an example, Al and Cu were used as heat spreader materials to cool the electronic components, while these metals have the relatively high CTEs that would generate high thermal stress during service. The incorporation of reinforcements such as SiC particles [20], carbon fibres [21], and diamond particles [22] into the metal matrix has been proved to be effective to improve overall thermal performance of the composite. However, these fillers still have the disadvantages of high cost and difficulty in machining. In 2008, Prieto et al. [23] firstly reported that G_f can be a promising reinforcement to make low cost and high thermal performance MMCs. Since then, this kind of materials have been investigated for more than 10 years in the aspects of processing, thermal and mechanical properties, and interfacial states between the matrix and reinforcement. In the most of investigations, G_f was used to reinforce the Al or Cu matrices aiming at enhancing the TC and tailoring the CTE.

There are many fabrication techniques to produce MMCs which are typically classified as liquid or solid routes. In the liquid route, such as gas pressure-assisted liquid metal infiltration, G_f is used to prepare a precursor. Then, an applied external pressure forces the liquid metal or its alloys to pass through the precursor until that it solidifies to form the composite. However, no spacing between the layers of G_f after stacking makes the infiltration process impossible. One method was developed using SiC [24] or Si [25] particles as a separator to create some spaces between the G_f. This process is generally carried out in an inert atmosphere under pressure. One should point out that the use of the metal alloys in infiltration process tend to decrease the TC of the matrix as a result of electron scattering caused by solute atoms and various defects such as dislocations and grain boundaries [26]. Moreover, the existence of SiC or Si particles also degrades the overall TC of the composite. In addition, because the working temperature is higher than the melt point of the matrix, there is always the concern of the formation of reaction product between the solid reinforcement and the liquid matrix. For instance, excessive formation of an Al_4C_3 phase at the Al-C interface [27] is thought to reduce both TC and mechanical properties of such composites. To avoid the formation of this detrimental phase, powder metallurgy [28, 29] as the solid route was employed to fabricate highly dense composites and to reduce the probability of chemical reaction between the reinforcements and the metal matrix.

1.2.2.1 The methods to align the G_f

It has been reported that G_f exhibits the high in-plane TC of around 1000 W/m.K [30], while out-of-plane TC is only in the range 5 – 10 W/m.K [31], and it also has the high anisotropy in CTE (-1×10^{-6}/K in-plane, 28×10^{-6}/K out-of-plane [32]). Therefore, the orientation of G_f was always emphasized in the fabrication of composites when the TC along the basic plane of G_f was expected to be very high. Powder mixing and filling process was considered as an important step to determine the orientation of G_f. Some researchers [23, 28, 33] believe that G_f with flake geometry tend to stack on top of each other making the alignment of G_f feasible with the aid of uniaxial pressure. Others [34-37] have tried several technical approaches to ensure the high orientation of G_f. Hereafter, we review the various methods used for aligning G_f.

- **Uniaxial pressing**

Al/G_f composite was initially fabricated via liquid metal infiltration [23]. In this process, G_f is packed in a crucible to form a preform, during which the alignment of G_f is completed by means of applying the uniaxial pressure [25]. One feature of liquid metal infiltration is to produce composites with a high-volume faction of G_f (up to 70 vol.%) that is beneficial for the alignment of G_f and, in turn, enhancement of overall TC in the alignment direction. Fig 1.11 shows the micrograph of Al/G_f composite fabricated via infiltration presenting the array of G_f along one direction [24].

Uniaxial pressure was also employed to orient G_f in powder metallurgy process. As a result, G_f tend to be oriented along the direction perpendicular to the pressing one. Vacuum hot pressing (VHP) is a common technique in powder metallurgy. In the VHP process, the powder mixture undergoes cold compacting and hot pressing in order to get a final product, and uniaxial pressure is applied at both stages. Fig. 1.12 shows SEM micrographs of Al/G_f composites fabricated by VHP [38], in which most of G_f align along the horizontal direction. However, some misalignment of G_f can still be found in some local regions. It should be noted that only applying the uniaxial pressure is technically insufficient to get the high orientation of G_f when spherical and micrometer-sized Al powder was used.

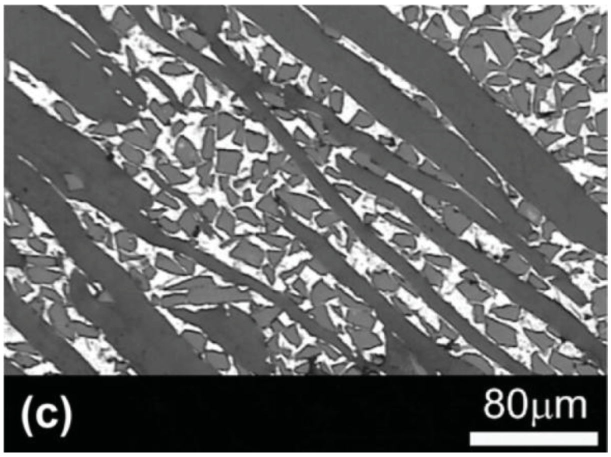

Fig. 1.11: SEM micrograph of the Al-12Si/70 vol.% G_f composite fabricated by gas pressure-assisted liquid metal infiltration where SiC particles were used as the separator [24].

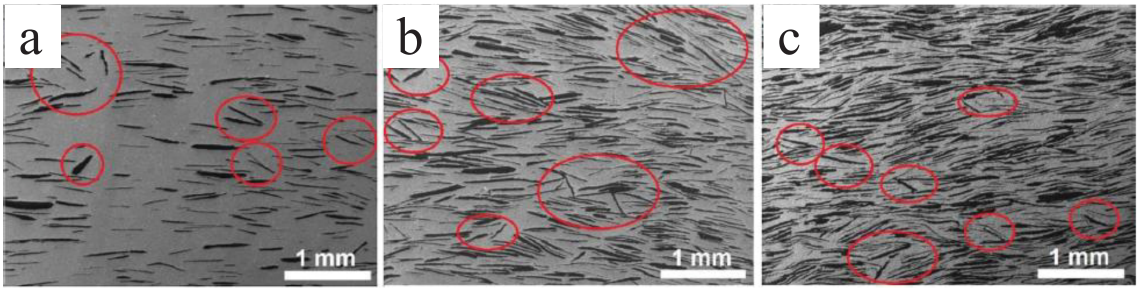

Fig. 1.12: SEM micrographs of the Al/G_f composite fabricated by powder metallurgy using a spherical Al powder as the matrix material: (a) 10 vol.%, (b) 30 vol.% and (c) 50 vol.% [38].

- **Tapping or vibrating**

Disordering G_f in a metal powder mixture occurs during the mechanical mixing process, such as using a 3D tubular mixer. When such a powder mixture is filled into the mold and compacted, certain of misalignment of G_f can be kept in the sample even after hot pressing (see Fig. 1.12). To improve the situation, tapping or vibrating the mold using a shaking device (see Fig. 1.13a) while filling the powder contributed to the directional arrangement of G_f [28, 39-41]. Thus, some upright G_f in the mixture would turn to the horizontal direction due to the effect of vibration wave. As shown in Fig. 1.13b, preferred orientation of G_f can be observed in the micrograph of the Al/G_f composite as a consequence of the vibration treatment of the mixture powder [40].

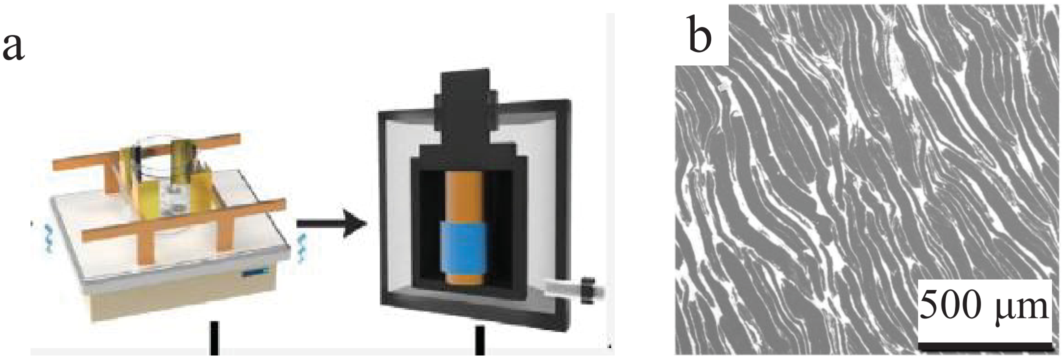

Fig. 1.13: (a) Schematic illustration of vibration device and (b) SEM micrograph of the Al/70 vol.% G_f composite with the desired orientation of G_f [40].

- **Filling powder in batches**

The thickness of the powder mixture containing the metal matrix and G_f after compacting in the die depends on the mass of loaded powder mixture and compression ratio. In practice, when all the mixture is filled in the mold once, the thickness of the powder is usually much higher than the diameter of single G_f in the range several hundreds of micrometres. In this case, G_f has the possibility to arrange in any directions. In order to avoid the randomly distributed G_f, the thickness of powder layer can be controlled such that the space can't hold the vertical G_f inside, thus G_f have to orient along the plane direction of the powder layer.

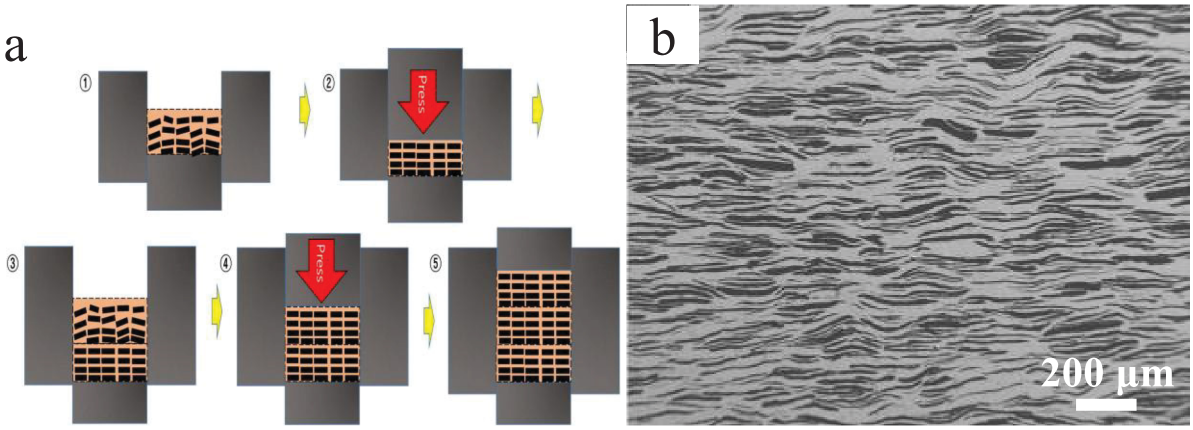

Fig. 1.14: (a) Schematic illustration of loading powder method to guarantee the unidirectional orientation of G_f, and (b) SEM micrograph of the obtained Cu/50 vol.% G_f composite using this method (adapted from [34]).

Several researchers [34, 42, 43] have reported that the unidirectional orientation of G_f can be well guaranteed by loading powder in several batches, and a proper pressure was applied to the powder in each step. A typical schematic illustration of this procedure is shown in Fig. 1.14a [34], in which a portion of mixture was put in the mold and compacted by applying pressure, and this step was repeated until all the powder were positioned. Applying this method, a highly unidirectional alignment of G_f in the Cu matrix can be obtained as shown in Fig. 1.14b [34].

- **Use of flake shaped powder and ball milling process**

As shown in Fig. 1.15, the high orientations of G_f were easily achieved in the Al/G_f composite using a flake Al powder through the one-step powder filling process [38]. Generally, the flake Al powder can be converted from the spherical one through a ball milling process. It was thought that the high alignment of G_f was attributed to the flaky geometry with large specific surface area recognized as better morphology compatibility with G_f compared to spherical powders [38, 44].

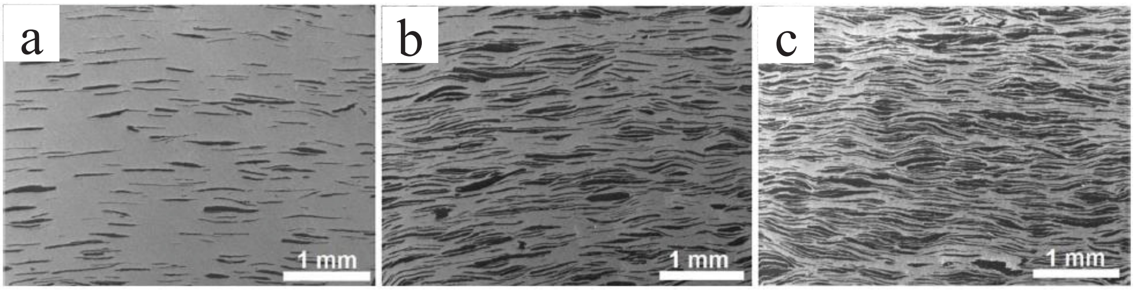

Fig. 1.15: SEM micrographs of the Al/G_f composites with the different volume fractions of G_f using a flake Al powder fabricated by VHP: (a) 10 vol.%, (b) 30 vol.% and (c) 50 vol.% (adapted from [38]).

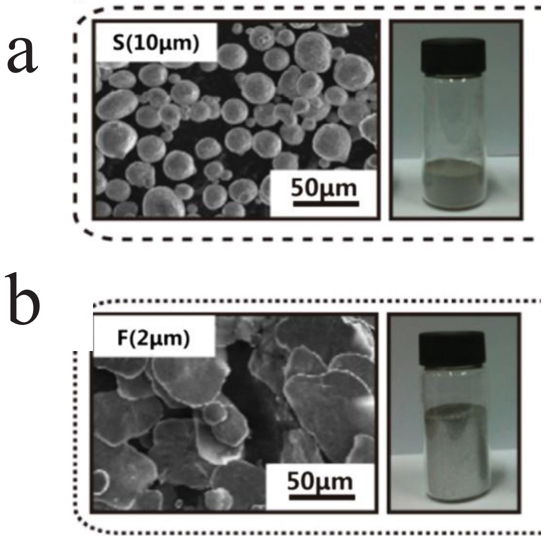

Fig. 1.16: The (a) spherical and (b) flaky morphologies of the Al powder showing the link between the apparent density and particle geometry (adapted from [45]).

However, it is worthy to mention that the apparent density of Al powder dramatically decreases when the powder shape changes from sphere to flake, as demonstrated in Fig. 1.16 [45]. Uniaxial pressing has an effect on the orientation the G_f because of the reduction of volume of powder compact during compressing where G_f rotates to the plane direction. If the volume reduction is not enough allowing all the G_f turn to this preferred direction, some misalignment of G_f will be left, which has been observed in the composite using the spherical Al powder [38]. Thus, it can be assumed that there is a critical value of apparent volume to get the well oriented G_f.

1.2.2.2 Quantitative analysis of the orientation of G_f

The anisotropic thermal performance of metal/G_f composites largely depends on the alignment degree of G_f. The higher alignment degree of G_f results in the better TC along the in-plane graphite direction. The orientation degree of G_f can be evaluated by a parameter $<\cos^2\theta>$ expressed as below [46].

$$\langle\cos^2\theta\rangle = \frac{\int \rho(\theta)\cos^2\theta\sin\theta d\theta}{\int \rho(\theta)\sin\theta d\theta} \tag{1.3}$$

Herein, $\rho(\theta)$ represents the statistical distribution of G_f, and θ is the angle between the horizontal plane of the composites and the basal plane of G_f. Theoretically, $<\cos^2\theta> = 1/3$ and $<\cos^2\theta> = 1$ relate to the totally random and perfect alignment of G_f in the composite, respectively. $<\cos^2\theta>$ can be calculated by determining the $\rho(\theta)$.

One of the approaches to determine the expression of $\rho(\theta)$ is image analysis of frequency (fraction of graphite for a given θ) versus θ from the corresponding cross-sectional views of metal/G_f composites with the aid of Image Tool software [47]. Original optical or SEM micrographs were transformed to black-and-white images to measure the angle distribution of G_f. The $\rho(\theta)$ was obtained by fitting plots of frequency versus θ.

On the other hand, the $\rho(\theta)$ can be obtained from polarized Raman spectra [44]. Graphite has four Raman-active modes as shown in Fig 1.17a, and its typical Raman spectra with well-ordered and disordered parts are presented in Fig. 1.17b. The first order spectrum with the E_{2g} mode at around 1582 cm^{-1} is generally regarded as G peak. The Raman intensity of the G peak as a function of the polarization angle of the incident and scattered light was used to characterize the alignment of G_f in the composites [36, 44]. Fig. 1.18a exhibits the schematic illustration of measurement setup. Theoretically, as demonstrated in Fig. 1.18b, for a random distribution of G_f, intensity of the G-peak is a constant when varying the polarization angle.

For perfectly aligned G_f, the intensity of G-peak $I_{tot} \propto f^2 \cos^4\varepsilon$ and thus has a maximum for the in-plane polarization (ε=0, 180°, and 360°), while it is zero for ε = 90°, 270°. Figs 1.18c and d show the results of the normalized intensity of the G-mode measured in the Cu/G_f composites [44]. The lower intensities at 90° and 270° indicate the better alignment of G_f.

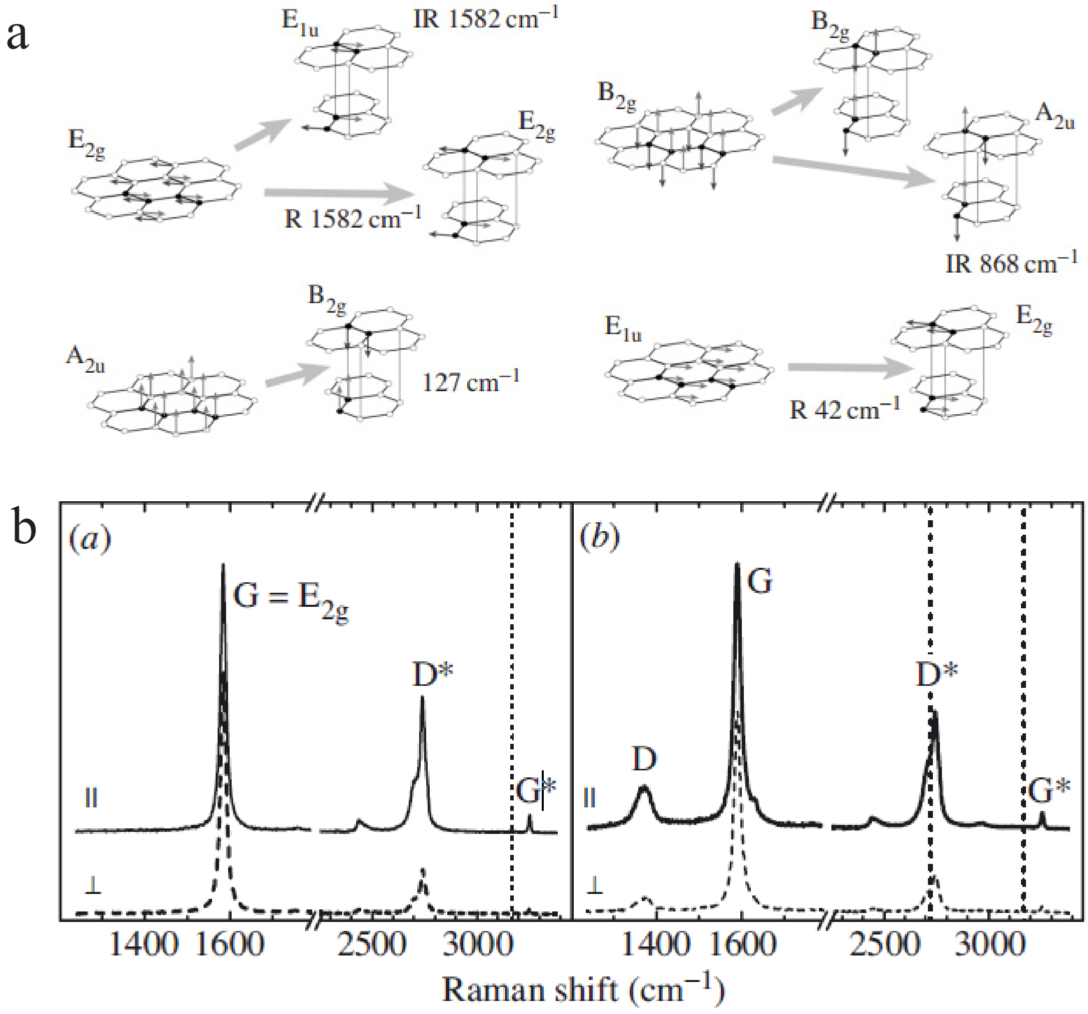

Fig. 1.17: (a) Optical lattice modes in graphite with indicated Raman and infrared activity and (b) Raman spectra of graphite taken at a perfect (left) and a disorder (right) part of G_f [48].

The expression of G_f alignment from polarization-angle dependence of the G peak was derived using the selection rules for light scattering in graphite to obtain the intensity of the Raman active modes of an individual G_f and then integrating over all the possible orientation angles. The overall intensity of G_f in a composite is expressed as follow [36, 44].

$$I_{tot} \propto \iint \rho(\theta_1,\sigma)\rho(\theta_2,\sigma) I_G(\theta_1,\theta_2)\, d_{\theta_1} d_{\theta_2} + I_0 \tag{1.4}$$

$$\rho(\theta,\sigma) = \frac{1}{\sigma\sqrt{2\pi}} e^{-\frac{\theta^2}{2\sigma^2}} \tag{1.5}$$

where $\rho(\theta,\sigma)$ is the angle distribution for the rotation angles θ_1 and θ_2, and I_0 is a corrected intensity for the measurement setup. Thus, the standard deviation σ is the only one parameter to match the Raman intensity of the composites. From the obtained $\rho(\theta)$, $<\cos^2\theta>$ can be calculated via numerical integration.

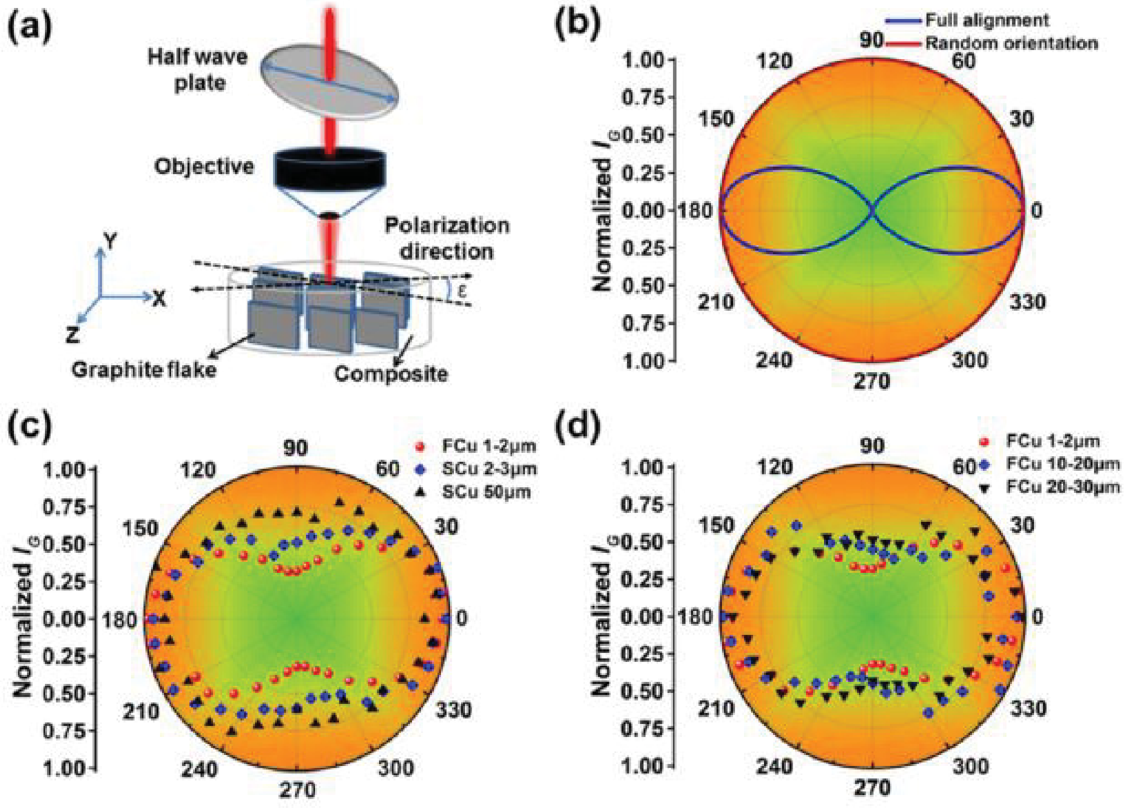

Fig. 1.18: Polarized Raman spectra used for characterize the orientation degree of G_f [44].

Additionally, X-ray diffraction (XRD) was applied to do qualitative analysis of G_f orientation. In the composite with high alignment of G_f, the intensity of d_{002} diffraction peak in the horizontal plane is usually hundred times higher than that in vertical one, as shown in Fig. 1.19, which originates from the highly anisotropic characteristic of G_f. The similar results have been reported in refs. [43, 49, 50].

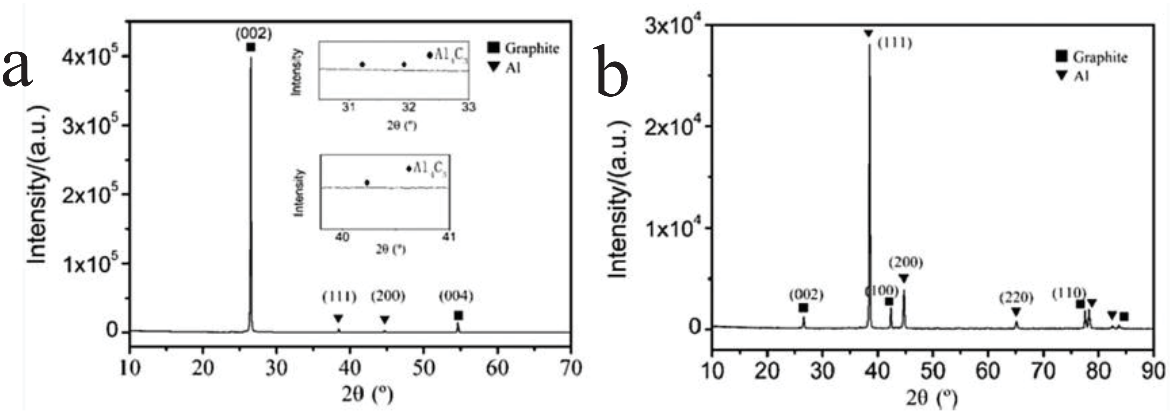

Fig. 1.19: Typical XRD patterns of the Al/G_f composites obtained from different planes, (a) horizontal plane, (b) vertical plane [51].

1.2.2.3 The effect of volume fraction of G_f and interface states on the TC and mechanical properties

The TC of the metal/G_f composites along the graphite in-plane direction has been successfully increased by improving the orientation and increasing the volume fraction of G_f because the intrinsic TC of in-plane graphite is much higher than pure metals like Al and Cu [28, 34, 51]. It can be understood by layers-in-parallel model without considering the interface thermal resistance in order to predict the TC of composites at a given volume fraction of reinforcement [52],

$$K_c = fK_r + (1 - f)K_m \tag{1.6}$$

where K_c, K_r, and K_m are the longitudinal TC of composite, reinforcement and matrix, respectively. f is the volume fraction of reinforcement. Generally, high volume fraction of G_f up to 70 vol.% was fabricated through the liquid routes including infiltration and squeeze casting, while the real content of G_f was obtained by means of image analysis of side-views of the composites [24]. By contrast, the volume percentage of G_f can be accurately controlled according to powder mass in powder metallurgy. Fig. 1.20 shows the SEM micrographs of the Al/G_f composites fabricated by powder metallurgy with the volume fractions of G_f from 10 vol.% to 90 vol.% [28]. However, the matrix becomes less discontinuous when the G_f content increases beyond 60 vol.%, and the relative density after sintering becomes very low which also degrades the overall TC of the composites. For example, the relative density reached around 93% when the composite contained 90 vol.% of filler and its experimental TC value was far off the theoretical one as shown in Fig. 1.21 [28]. Thus, the content of G_f no more than 50 vol.% was recommended when applying powder metallurgy process [33, 38] in order to ensure the relatively high TC.

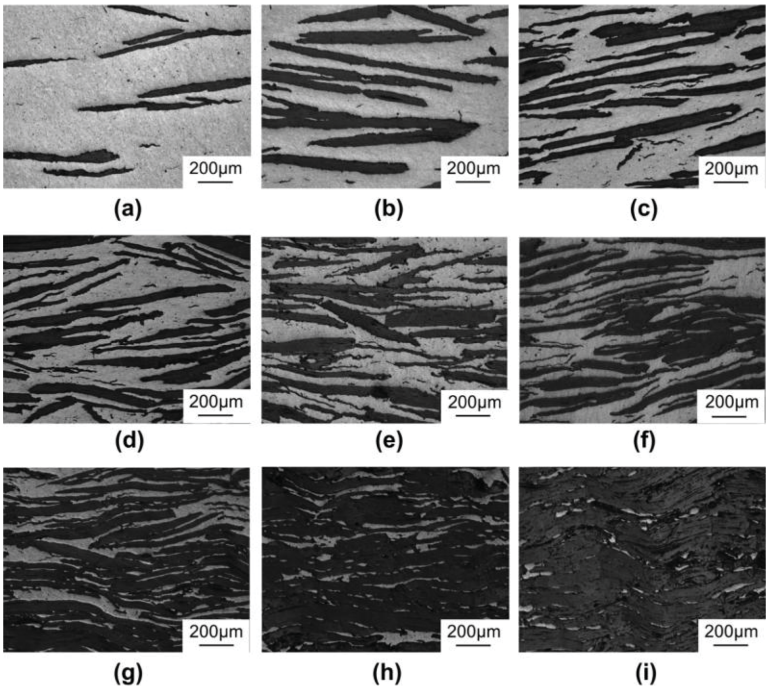

Fig. 1.20: SEM micrographs of the Al/G_f composites with the different volume fractions of G_f produced by powder metallurgy: (a) 10 vol.%, (b) 20 vol.%, (c) 30 vol.%, (d) 40 vol.%, (e) 50 vol.%, (f) 60 vol.%, (g) 70 vol.%, (h) 80 vol.% and (i) 90 vol.% [28].

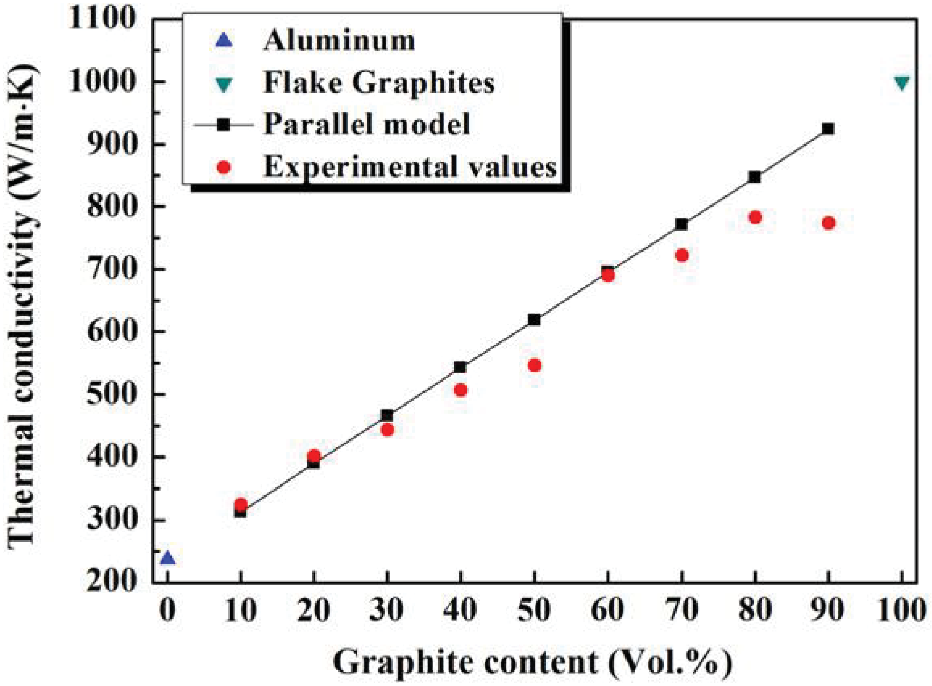

Fig. 1.21: Comparison of experimental and predicted values of TC [28].

Although the enhancement of TC has been achieved by adding a high amount of G_f as mentioned above, the mechanical property always becomes worse at the high G_f content compared to the pure matrix due to brittle nature of G_f itself, as shown in Fig. 1.22 [53]. This is unfavorable considering the potential use of the metal/G_f composites as electronic packaging materials. In-plane G_f has high strength covalent bonding, but the connection between layers of G_f is controlled by van der Waals force, which is easy to be split into separated parts. In addition, the weak interfacial bonding between G_f and metal matrix also results in poor mechanical property of the composites [33]. It is contradictory to improve both TC and mechanical property in metal/G_f composites by increasing the proportion of G_f.

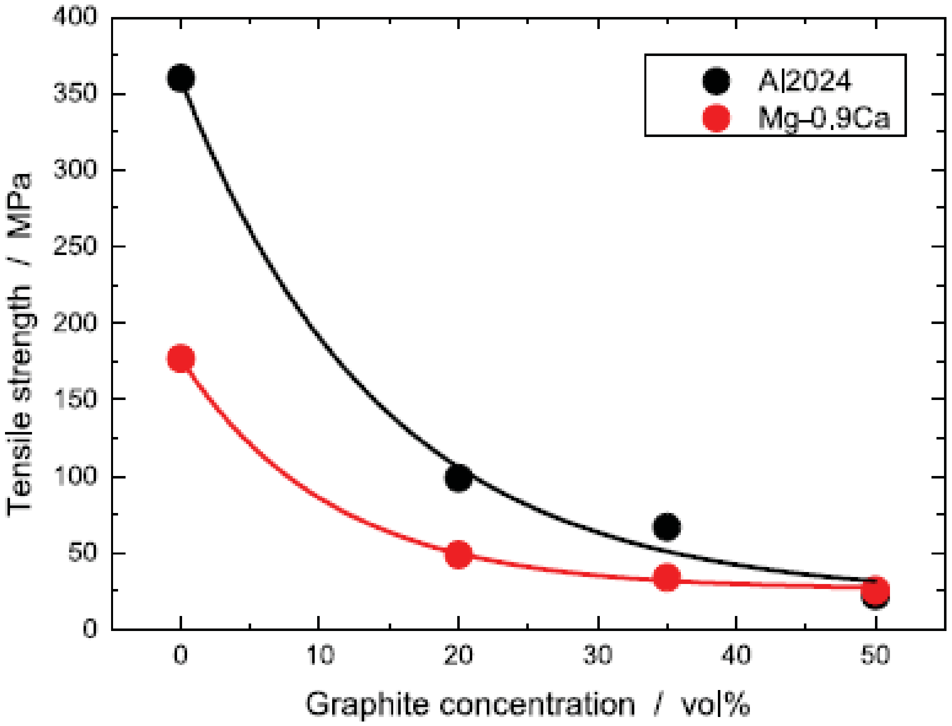

Fig. 1.22: Tensile strength of the Al2024/G_f and Mg-0.9Ca/G_f composites as a function of G_f content [53].

The overall performance of the composites is not only relying on the intrinsic properties of the matrix and reinforcement, but also determined by the interfacial bonding state between them. The interface/interphase generally plays an important role in determining heat exchange or load transfer between the constitute phases in the composites.

As aforementioned, interfacial chemical reaction between Al and carbon forms Al_4C_3 which can degrade the thermo-physical properties of the composites, while Al_4C_3 was usually observed in porous graphite or Al/CF composites manufactured by liquid infiltration using a high temperature and a low cooling rate [27, 54]. It was also reported that there was no trace amount of Al_4C_3 in the Al/G_f composites fabricated by either liquid route [24, 25, 51] or powder metallurgy [28, 33]. The main reason is attributed to the low degree of graphitization of porous graphite or some CFs providing more sites for nucleation of carbides compared to highly crystallized G_f [27]. Moreover, the interface between Al and G_f can be featured with a nano-sized void layer caused by thermal stress [33, 55].

Cu and carbon were considered as a nonreactive system, which means only the mechanical bonding can be formed between them. One simple approach to improve interfacial heat transfer efficiency as well as the TC of Cu/G_f was using the heat treated G_f under H_2 atmosphere; this process can remove the impurities (i.e. oxygen) on the side of the G_f [56]. Nevertheless, most of investigations focused on tailoring the interfacial zone between G_f and metal matrices by introducing a third element to form carbide or other compounds. The major candidates were carbide forming elements, such as Ti [39], Zr [43], Cr [57], Si [40, 41], and B [49], or some elements easily to be coated on the surface of carbon, such as Cu [58] and Ni [35].

Chen et al. utilized salt bath method to grow a layer of SiC or TiC on the surface of G_f [39]. Specifically, a mixture of G_f, Si powder (or Ti powder) and $CaCl_2$ powder was heat treated at a high temperature, in which the melted $CaCl_2$ transferred Si to the surface of G_f and the reaction of Si-C occurred. As shown in Fig. 1.23, bending strengths of the coated Al/G_f composites were increased, and more dramatically for the TiC coated G_f compared to uncoated G_f. Meanwhile, SiC coating of G_f improve the TC of Al/G_f composites, whereas the TiC coating degraded the TC. Besides, coating of boron carbide on the surface of G_f was carried out in a NaCl salt bath [49], and it increased the flexural strength but decreased the TC of the Cu/G_f composites.

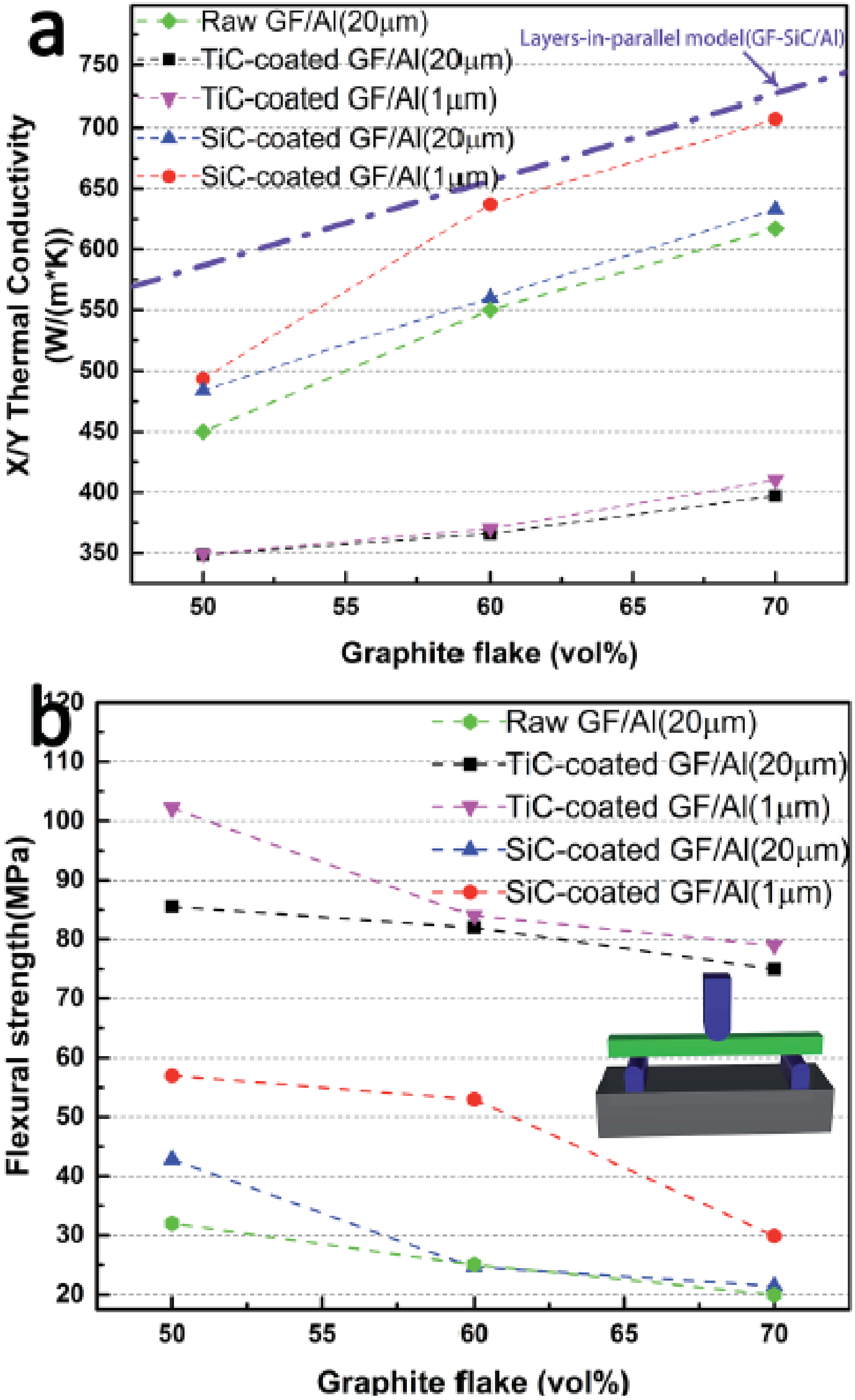

Fig. 1.23: The effect of SiC or TiC coated G_f on the (a) TC and (b) flexural strength of the Al/G_f composites [39].

Further, it was also reported in the Cu/G_f composites that adding a moderate amount of carbide forming elements in the Cu matrix by ball milling can increase TC as a result of the enhancement of the interfacial bonding [43, 57, 59, 60]. For example, the addition of Zr improved the TC of the Cu/G_f composites as it formed a layer of ZrC at the interfacial zone as shown in Fig. 1.24. Due to the absence of chemical reaction between Cu and graphite, void layer is present at the Cu/G_f interface causing high interfacial thermal resistance [59]. The formation of carbide at the interface will act as a solid heat transport media which markedly reduced the interfacial thermal resistance leading to an increase of the overall TC of the composites. However, the increase of thickness of the carbide layer will boost the interfacial thermal resistance to decrease the TC of the composite. Thus, there is an optimized content of carbide forming element or thickness of the carbide layer to obtain the beneficial enhancement of TC. Additionally, the addition of a carbide forming element improved the mechanical property of Cu/G_f composites by enhancing the interfacial bonding.

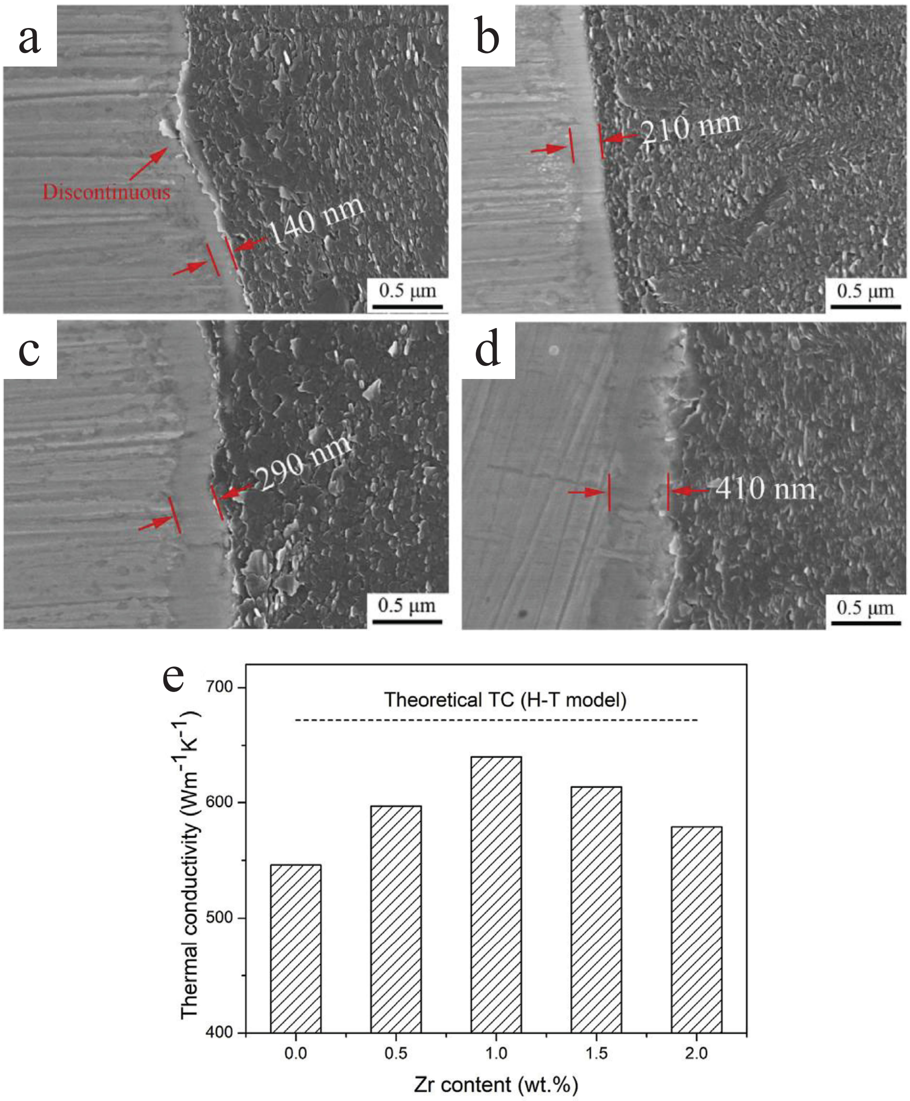

Fig. 1.24: SEM micrographs of the interfacial zone for Cu-Zr/G_f composites with the different content of Zr: (a) 0.5 wt.%, (b) 1.0 wt.%, (c) 1.5 wt.%, (d) 2.0 wt.% and (e) the effect of Zr addition on the TC [43].

1.2.2.4 Models for predicting TC of the composites

Heat flows in a solid is realized by the transmission of phonons (lattice vibrations) and/or free electrons. Both of these carriers have a certain mean free path λ between collisions (energy exchange events) and an average velocity ν. the TC K is related to these parameters by the equation [26]:

$$K = \frac{c\nu\lambda}{3} \tag{1.7}$$

in which c is the volume specific heat of the carrier. The mean free path of a phonon is determined by perfection degree of lattice and can be very high in perfect crystal, like single crystals. Usually electrons in metals have a much larger mean free path than phonons, which gives metals a relatively high TC, but it can be reduced by the presence of solute atoms and various defects that cause electron scattering. The average carrier velocity is insensitive to temperature in both cases.

MMCs consist of two or three phases with specific TCs. As a general sense, the “microscopic” length scale (e.g. the average domain size) of different phases in composites is much larger than the molecular dimensions but much smaller than the characteristic length of the macroscopic specimen. Thus, the composite can be regarded as a continuum on the microscopic scale and macroscopic or “effective” properties can be ascribed to it [61]. Theoretically, it is of importance to predict precisely how the TC of the composites varies with matrix and reinforcement physical properties, volume fraction, distribution, aspect ratio and interfacial structure.

As mentioned before if we assume that the interface between the matrix and reinforcement is perfect, layers-in-parallel model was used to calculate the overall TC of the composites, but this model usually overestimated the values compared with the measured ones [25, 28]. In practice, there is a temperature discontinuity at the interface, noted as the interfacial thermal resistance or Kapitza resistance [62]. A model considering the interfacial thermal resistance was developed by Hasselman and Johnson [63]. It is suitable for the composites with dilute concentrations of spherical inclusions. The expression is as follow.

$$K_c = \frac{K_m\left[2K_m + K_r^{eff} + 2\left(K_r^{eff} - K_m\right)\cdot f_r\right]}{2K_m + K_r^{eff} - \left(K_r^{eff} - K_m\right)\cdot f_r} \tag{1.8}$$

$$K_r^{eff} = \frac{K_r}{1 + \frac{K_r}{a\cdot h}} \tag{1.9}$$

where K_m, K_r, and f_r are the TC of matrix, TC of reinforcement, and volume fraction of reinforcement, respectively. K_r^{eff} is the effective TC of filler, and a and h are the average radius of reinforcement particles and interfacial thermal conductance (i.e. reciprocal of interfacial thermal resistance) of the matrix-reinforcement interface, respectively. Thus, it can be used to estimate the TC in particulate reinforced composites [24, 64]. And the theoretical TC can also be computed with differential effective medium (DEM) scheme [65]:

$$(1-f_r)\left(\frac{K_c}{K_m}\right)^{\frac{1}{3}} = \frac{K_r^{eff}-K_c}{K_r^{eff}-K_m} \tag{1.10}$$

Among these parameters, h can be calculated by the acoustic mismatch model (AMM), which views the interfacial heat transfer as continuum mechanics by calculating the probability of an incident phone passing the interface [62].

$$h_{AMM} \cong \frac{1}{2}\rho_m C_m \frac{\upsilon_m^3}{\upsilon_r^2}\frac{\rho_m \upsilon_m \rho_r \upsilon_r}{(\rho_m \upsilon_m + \rho_r \upsilon_r)^2} \tag{1.11}$$

where C, ρ, and υ are the specific heat capacity, density and the Debye phonon velocity, respectively, and subscripts m and r represent the matrix and reinforcement, respectively.

In some circumstances, the surface of reinforcement (e.g. G_f) was covered with a layer of coating [39, 49, 59], and the multi-interfaces metal/coating/G_f become complex. The interfacial thermal conductance of matrix-coating and coating-reinforcement can be obtained by AMM, while the overall h_t can be estimated using the following equation [41]:

$$\frac{1}{h_t} = \frac{1}{h_{m-c}} + \frac{1}{h_{c-r}} + \frac{d_c}{K_c} \tag{1.12}$$

where d_c and K_c are the thickness and TC of coating, respectively.

Different from the spherical particle reinforcement, G_f presents thin disc shape and anisotropy in properties, Hatta-Taya model is thus more applicable in this case, which deals with the high concentrations of reinforcement [66].

$$K_c = K_m + \frac{K_m \cdot f_r}{S_i(1-f_r)+\frac{K_m}{k_f^i - K_m}} \tag{1.13}$$

$$S_L = \frac{\pi t}{4D} \tag{1.14}$$

$$S_T = 1 - \frac{\pi t}{2D} \tag{1.15}$$

in which S_i is a factor related to the morphology and alignment of reinforcement, and L, T stand for the longitudinal and transversal directions, respectively. This model assumes that the reinforcements are well oriented.

One more important model is effective-medium approximation (EMA) proposed by Nan [46], which not only considers the geometry, the interface, but also the orientation degree ($<\cos^2\theta>$) of the reinforcement. The TC predictions along the longitudinal (x, y) and transversal (z) directions are given below:

$$K_{xy} = Km\frac{2+f[\beta_L(1-S_L)(1+\langle\cos^2\theta\rangle)+\beta_T(1-S_T)(1-\langle\cos^2\theta\rangle)]}{2-f[\beta_L S_L(1+\langle\cos^2\theta\rangle)+\beta_T S_T(1-\langle\cos^2\theta\rangle)]} \tag{1.16}$$

$$K_z = Km\frac{1+f[\beta_L(1-S_L)(1-\langle\cos^2\theta\rangle)+\beta_T(1-S_T)\langle\cos^2\theta\rangle]}{1-f[\beta_L S_L(1-\langle\cos^2\theta\rangle)+\beta_T S_T\langle\cos^2\theta\rangle]} \tag{1.17}$$

in which

$$\beta_i = \frac{K_i-K_m}{K_m+S_i(K_i-K_m)}, \quad (i = L, T) \tag{1.18}$$

And the other parameters have the same meaning as mentioned before. Until now, EMA model involves almost all the factors relating to the TC of composites, thus, it became the most popularly used model to predict the TC of the metal/G_f composites.

1.2.2.5 The counterintuitive performance of CTE in metal/G_f composites

Naturally, G_f presents a negative CTE along in-plane direction, and a relatively high CTE along the through-plane direction. Metals generally have an isotropic CTE. However, in the metal/G_f composites with oriented distribution of G_f, a high CTE in-plane and low or even negative through-plane have been measured, which is opposite to the prediction according to the rule of mixtures [67]. This counterintuitive phenomena were reported for various metal matrices, such as Cu [35, 36, 49], Al or Al alloys [25, 28], and Mg alloys [53], being independent of processing processes of liquid infiltration or powder metallurgy. The tendency is that the in-plane CTE goes down remarkably to a very low value and the through-plane CTE decreases a little bit with increase of G_f content, as displayed in Fig.1.25. Zhou et al. [25] reported that the measured through-plane CTE was just slightly lower than the in-plane CTE in the ternary composites consisting of Al alloy, Si particle and G_f.

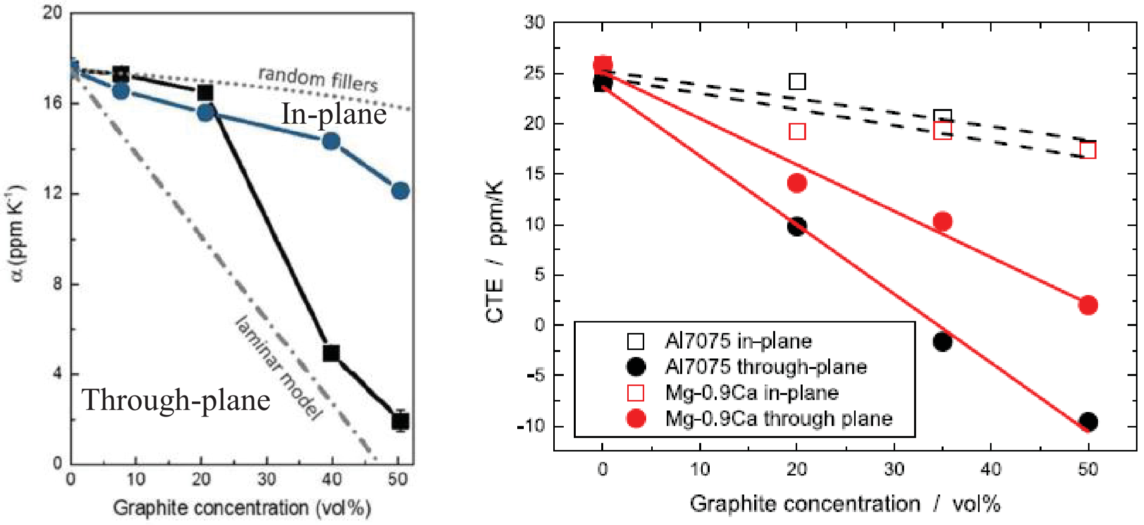

Fig. 1.25: In-plane and through-plane CTE as a function of volume fraction of graphite content in the metal/G_f composites: (a) Cu matrix [36], (b) Al alloys and Mg alloy matrices [53].

In fact, the CTE is derived from thermal expansion curves measured by a dilatometer. If the evolution of thermal expansion is linear, the CTE value is constant and equal to the slope of the curve, and if not, an average physical CTE was used for the examination, which is obtained by dividing the change in thermal strain with the corresponding temperature range. As shown in Fig.1.26, the dilatometry curve is linear along the x,y direction during the whole heating/cooling cycles, while it shows that material shrinks first and then expands in the z-direction at the cooling stage [68]. It is worth noting that the CTE values being evaluated varies with the selection of temperature range when the dilatometry curve is nonlinear. Several models (Kerner's model [69], Turner's model [70], and Schapery's model [71]) have been used to explain the CTE behaviours of composites, but none of them is effective [35, 68]. Firkowska et al. [36] proposed a laminar model, and attributed the anomalous CTE to two temperature dependent factors including in-plane strain of G_f and large two-dimensional Poisson ratios. The CTE of graphite along through-plane direction was calculated to be -26 ppm/K based on an elasticity theory, and the CTE of Cu matrix along the in-plane direction was 24 ppm/K due to the compressive in-plane strain. The possible description is that macro folding of G_f in basal plane occurs when the metal matrix shrinks during the cooling process after hot pressing, which leads to the thickness increase of G_f along the through-plane direction. When the composite is heated, the G_f would spread in the in-plane direction as the metal matrix expands, and the gradual disappearance of folding in G_f would result in the decrease of G_f thickness, thus the CTE of G_f in z-direction appears as negative so as to make the CTE of composite is relatively low in this direction. However, Oddone et al. argued that there is the absence of residual strain from neutron scattering results [68], which suggested that compression of G_f in basal plane is not at microscopic but macroscopic scale due to the high Young's modulus of G_f.

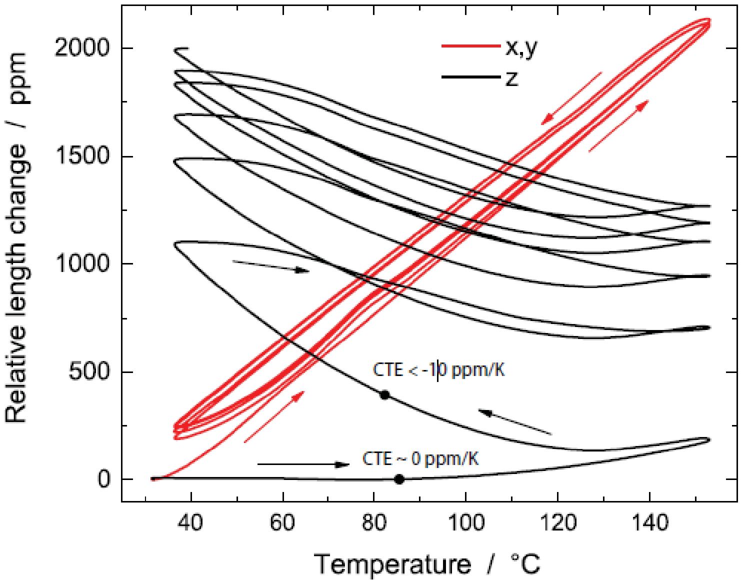

Fig. 1.26: Thermal expansion curves of an Al2040/G_f composite in the in-plane (x, y) and through-plane (z) directions [68].

The CTE of the metal/G_f composites is not only influenced by the G_f content but also by the metal-G_f interfacial properties. Several studies have shown that an enhanced interfacial bonding between coated G_f and metal matrix resulted in a lower CTE value in the through-plane direction compared with uncoated G_f [35, 44, 60] (cf. Fig. 1.27). It is explained that the enhanced interface adhesion facilitates the stress transfer between the Cu matrix and reinforcement. Therefore, G_f could effectively curb the expansion of the Cu matrix during heating [35]. Zhao et al. [60] considered that the thickness of G_f decreases more under the tensile force generated by the thermal expansion of the matrix as a result of the more compact interface, which is consistent with the interpretation from Bai et al. [49].

Certainly, a high anisotropy in CTE parallel and perpendicular to the pressing direction was retained in the metal/G_f composites, which is not favorable to match the two-dimensional CTE of electronic components. It was reported that CF reinforced MMCs resulted in the higher z-CTE and lower x,y-CTE [72], which exhibits an opposite trend compared with the metal/G_f composites. Thus, combination of carbon fiber and G_f reinforcements was added to the Al matrix in order to use its synergetic effect on the thermo-mechanical performance [55, 73]. By varying the volume fraction ratio of G_f and CF, an isotropy in CTE was obtained within the in-plane and through-plane directions, as shown in Fig. 1.28 [73]. Nevertheless, the addition of CF decreased TC of the metal/G_f composites along the in-plane direction.

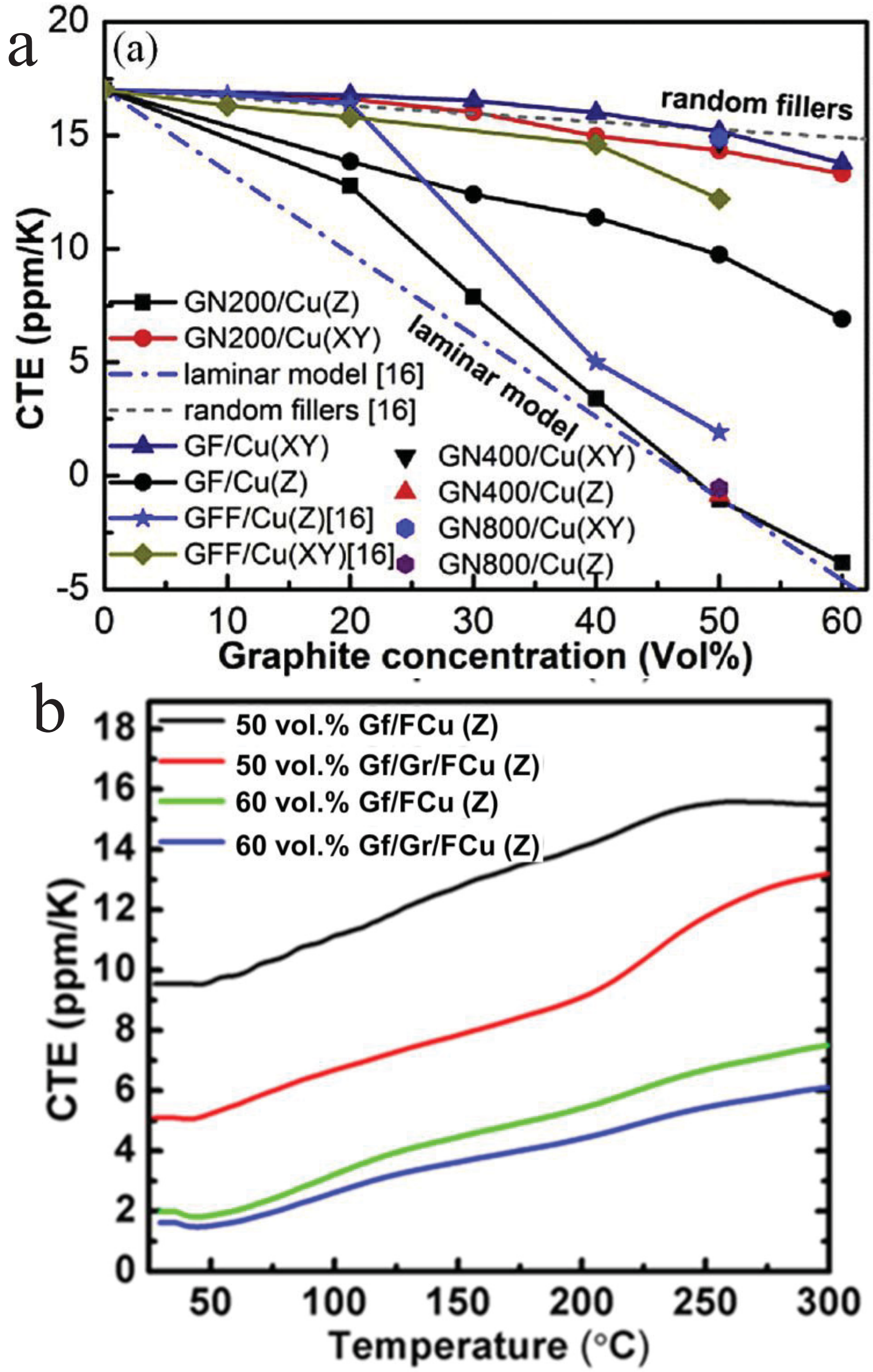

Fig. 1.27: The effect of modification in the interfacial states on the through-plane CTE of the Cu/G_f composite: (a) [35], (b) [44].

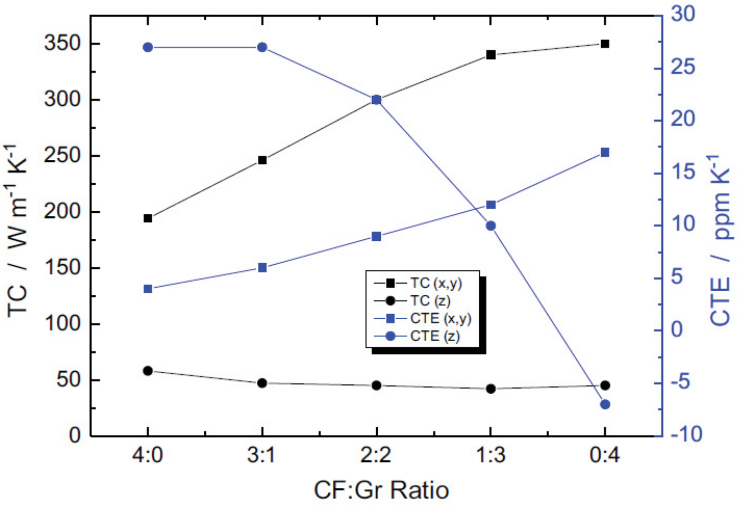

Fig. 1.28: TC and CTE values of the Al2024/G_f composite as a function of the CF/Gr ratio (Gr denote graphite flake) [73].

1.2.3 Al matrix composites reinforced with nanosized particles

Although the Al/G_f composites have shown very promising thermal properties, their low strength is still the main obstacle for potential applications in the electronic packaging industry. It has been mentioned in section 1.3 that mechanical properties of the Al/G_f composites can be improved by strengthening interfacial bonding between the Al matrix and G_f. The other effective way is to increase strength of the Al matrix by using Al alloy, but it significantly degrades its TC. Thus, this solution was excluded in this study. Further, it has been well-known that pure Al matrix can be strengthened by homogenously integrating micrometer sized or nano-sized ceramic particles. It has been expected that the composites reinforced with a small amount of nano-sized reinforcements could not only exhibit higher yield strength than their counterparts with micrometer sized reinforcements, but also limit the degradation of TC of the pure Al matrix. Various nanosized ceramic particles, such as SiC, B_4C, Al_2O_3, TiC, SiO_2, AlN, and TiB_2 [74], were tested to reinforce the Al matrix by ex-situ and in-situ processing processes. An ex-situ route involves introducing nanoparticles to the liquid or metal powder, and an in-situ route refers to the techniques leading to the formation of nano-sized ceramic reinforcement particles by chemical reaction during processing. The main challenge in the fabrication of Al nanocomposites is homogeneous dispersion of nanoparticles, because they tend to form agglomeration or clustering. In this section, some fabrication methods and properties of Al nanocomposites (choice of reinforcements mainly focusing on SiC and TiB_2) are reviewed.

1.2.3.1 Dispersion of nanosized SiC particles by an ex-situ route

- **Ultrasonic method**

In the casting process, simply mechanical mixing of nano-sized ceramic particles in the liquid metal resulted in agglomeration and clustering due to high viscosity and poor wettability in the metal matrix, which causes a nonuniform reinforcement distribution. Ultrasonic wave was used to disperse nano-sized ceramic particles in the liquid Al as it can break down the big agglomeration through acoustic cavitation effect [75]. High intensity ultrasonic wave can induce periodic positive and negative pressure fields in the liquid. Micro-bubbles can be generated, expanding during the negative pressure, and it will collapse in the following positive pressure. The whole process is called acoustic cavitation. The collapse of micro-bubble can cause transient local micro "hot spots" that can reach a very high temperature and high pressure so as to break down nano-sized particle clusters and enhance the wettability of nanoparticles with matrix. Many investigations have been conducted to produce the composites reinforced with nano-particles via this ultrasonic solidification method [75-78], and the process is illustrated in the Fig. 1.29. Yang et al. [75] manufactured the nano-sized SiC particles reinforced A356 Al alloy composites using ultrasonic non-linear effects. As shown in Fig. 1.30, the nearly uniform dispersion of nano-SiC was achieved compared with the severe agglomerates in composites using traditional casting.

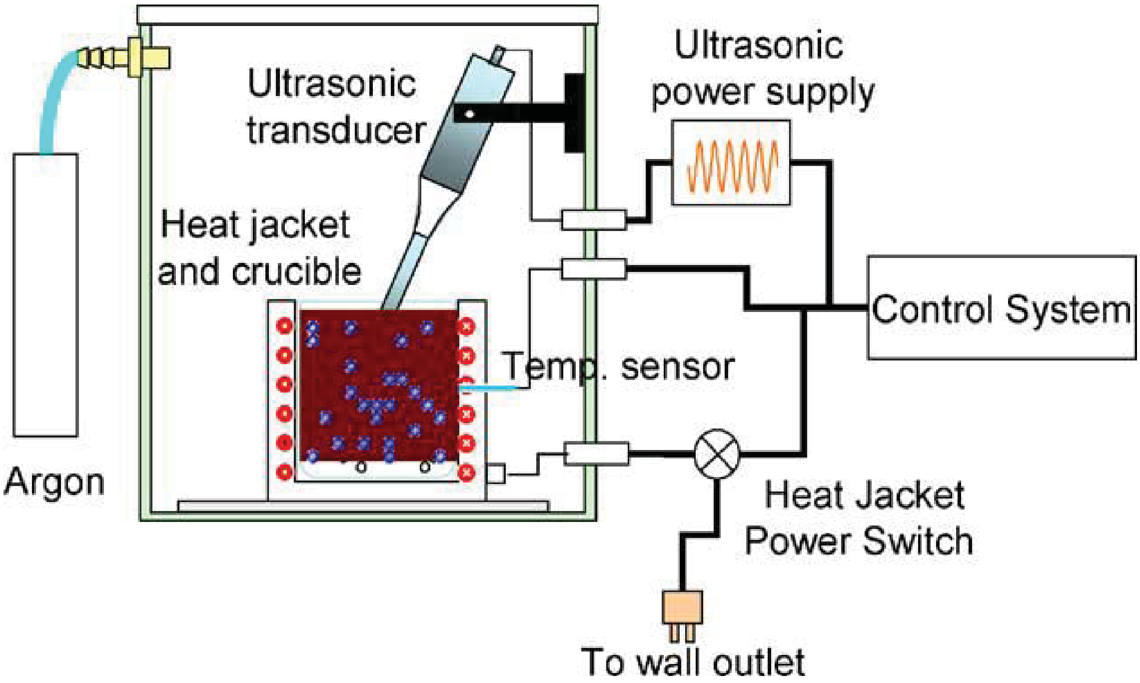

Fig. 1.29: Schematic of ultrasonic solidification setup [75].

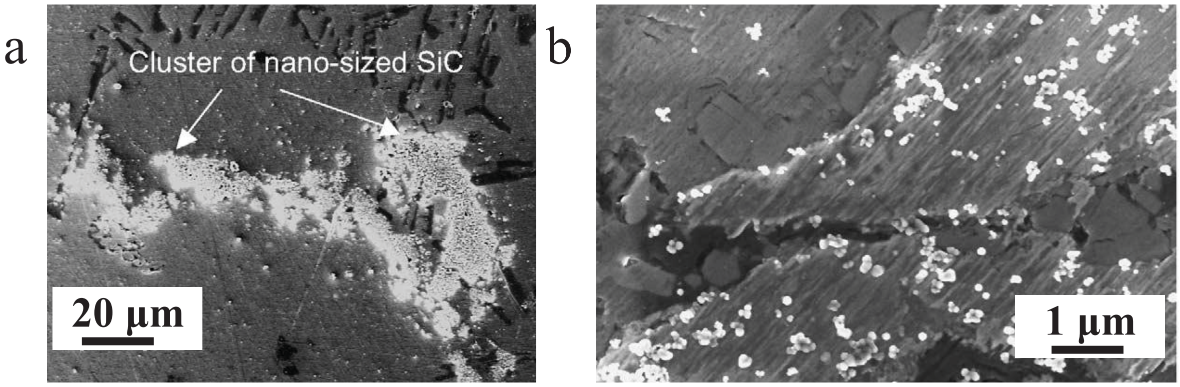

Fig. 1.30: SEM micrographs of Al nanocomposite reinforced with nanosized SiC: (a) cluster of nano SiC, (b) improved dispersion of nano SiC via ultrasonic treatment [75].

Besides, nano-particle agglomerates can also be disintegrated in liquid, like ethanol and water, at room temperature with the aid of ultrasound. Nano-SiC particles was dispersed in ethanol by ultrasonic-assisted stirring, then, the suspension containing nano-particles was mixed with Al powder by a planetary mixer [79]. It was believed that the nano-SiC particles were well distributed on the surface of Al powder as shown in Fig. 1.31. This method is achievable because nano-SiC is easy to form colloid suspension in neutral ethanol, in which the particles take negative charges [80, 81], while Al particles take positive charges in ethanol at a similar condition [82]. When Al and nano-SiC particles meet together in ethanol, they will attract each other to form a composite powder because of the electrostatic effect. This process was usually called hetero-agglomeration method [83]. However, this method only allowed nanoparticles to disperse on the surface of Al particles and, in turn, at the inter-particle boundaries after sintering. Hot extrusion can also be used to improve its distribution via dynamic recrystallization [79].

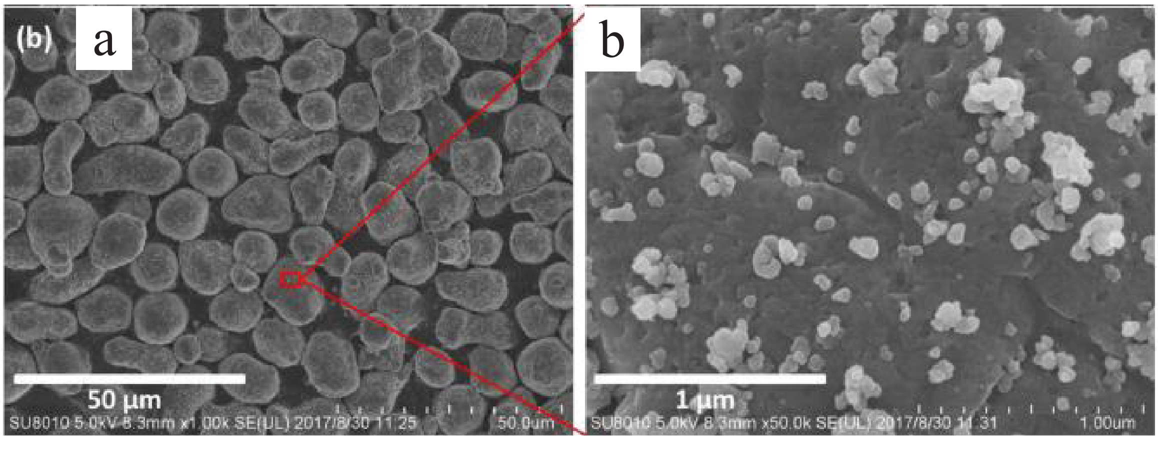

Fig. 1.31: (a) low- and (b) high-magnification SEM micrographs showing spherical Al powder particles after mixing with 2 wt.% of nano-SiC particles [79].

- **Ball milling**

Ball milling is a solid-state powder processing method. It involves repeated cold welding, fracturing of particles in a high energy ball mill. The main factors affecting the milled products include ball to powder weight ratio, ball material (i.e. Al_2O_3, steel, tungsten carbide, …), milling atmosphere, process control agent, and milling time [84]. Usually, the process control agent was added especially for ductile materials to prevent or minimize the effect of welding, such as stearic acid, heptane, methanol, and isopropanol. This technique can not only be used to decrease the size of ceramic particle from macro to nano scale, but also produce a homogenous material starting from powder mixtures. Therefore, it has been applied to incorporate nano-sized ceramic particles into the Al matrix, and most of researchers employed a planetary ball mill to reach this technical goal [85-88]. One of the advantages is that the hard nanoparticles can be embedded in the ductile matrix particles during milling process. The ball milled powders were usually consolidated by powder metallurgy.

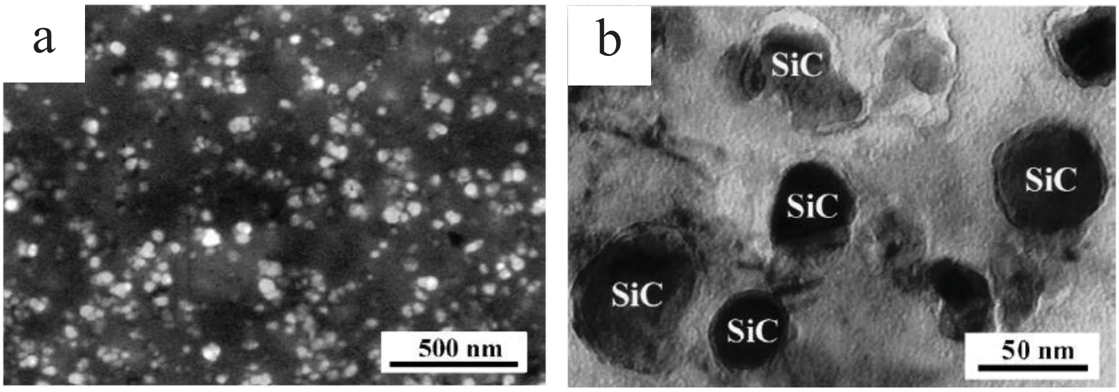

Fig. 1.32: (a) SEM and (b) TEM micrographs showing the distribution of SiC particles in Al matrix composite prepared by ball milling [85].

Feng et al. fabricated nano composites of Al5083/SiC through cryomilling followed by hot isostatic pressing [85]. Cryomilling refers to milling operation that is carried out at a very low temperature provided by a cryogenic medium such as liquid nitrogen. The uniform distribution of nanoparticles was revealed by the SEM and TEM analysis (see Fig. 1.32), and the tightly adhered interfacial bonding between the Al matrix and SiC was observed. Also, Mazahery et al. utilized the ball milling process to disperse nano-SiC in the Al powder to form an Al/SiC composite powder, then, the material was fabricated using stirring casting by adding the milled Al/SiC powder into the Al alloy melt [87]. The uniform dispersion of SiC nanoparticles in the Al matrix was achieved by applying this process. Thus, ball milling can be regarded as an effective method to disperse nanoparticles, although some small agglomerates remain in the matrix.

1.2.3.2 In-situ method to produce TiB_2 reinforced Al composites

Regarding in-situ MMCs, the reinforcements are synthesized in the metal matrix by exothermal reactions among the elements during the process. Compared to the ex-situ method, in-situ formed reinforcements are thermodynamically stable in the matrix, the interfaces between the matrix and reinforcement are clean leading to a strong interfacial bonding, and the particles formed in-situ are much finer in size and their distribution is more uniform [89]. A typical process to produce Al composites reinforced with TiB_2 nanoparticles is termed as flux-assisted synthesis. During this process, mixed salts of potassium hexafluoro-titanate (K_2TiF_6) and potassium tetrafluororate (KBF_4) are added in atomic ratio of Ti/2B to the molten Al while stirring [90]. The reaction presenting the formation of TiB_2 can be written as:

$$3K_2TiF_6 + 13Al \rightarrow 3TiAl_3 + 3KAlF_4 + K_3AlF_6$$

$$2KBF_4 + 3Al \rightarrow AlB_2 + 2KAlF_4$$

$$AlB_2 + TiAl_3 \rightarrow 4Al + TiB_2$$

When the reaction is completed, the stirring is stopped to remove the slag containing $KAlF_4$ and K_3AlF_6 from the top of the Al melt, and the molten composite is cast into the mold. The maximum volume fraction of in-situ reacted TiB_2 is limited by the viscosity of the subsequent melt. This technique has been widely used to produce Al/TiB_2 composites with improved mechanical performance because of its low cost and simplicity [74, 91, 92].

1.2.3.3 Mechanical properties and strengthening mechanisms

Tensile and compressive tests and hardness measurement have been used to evaluate mechanical performance of the composites reinforced with nanosized particles. The mechanical properties of composite materials mainly depend on type of reinforcement, shape, quantity of reinforcement, distribution and size etc. [93]. Generally, the mechanical properties (e.g. 0.2% yield strength, ultimate tensile strength, and hardness) of nanocomposites are improved with increasing the volume fraction of nanosized reinforcement [76, 87, 94, 95]. Fig. 1.33a shows that the yield strength of as-cast aluminum alloy A356 was enhanced by about 50% due to the addition of 2 wt.% nano-sized SiC [76], and this strengthening effect is also visible in the TiB_2 reinforced Al composites (Fig. 1.33b) [96].

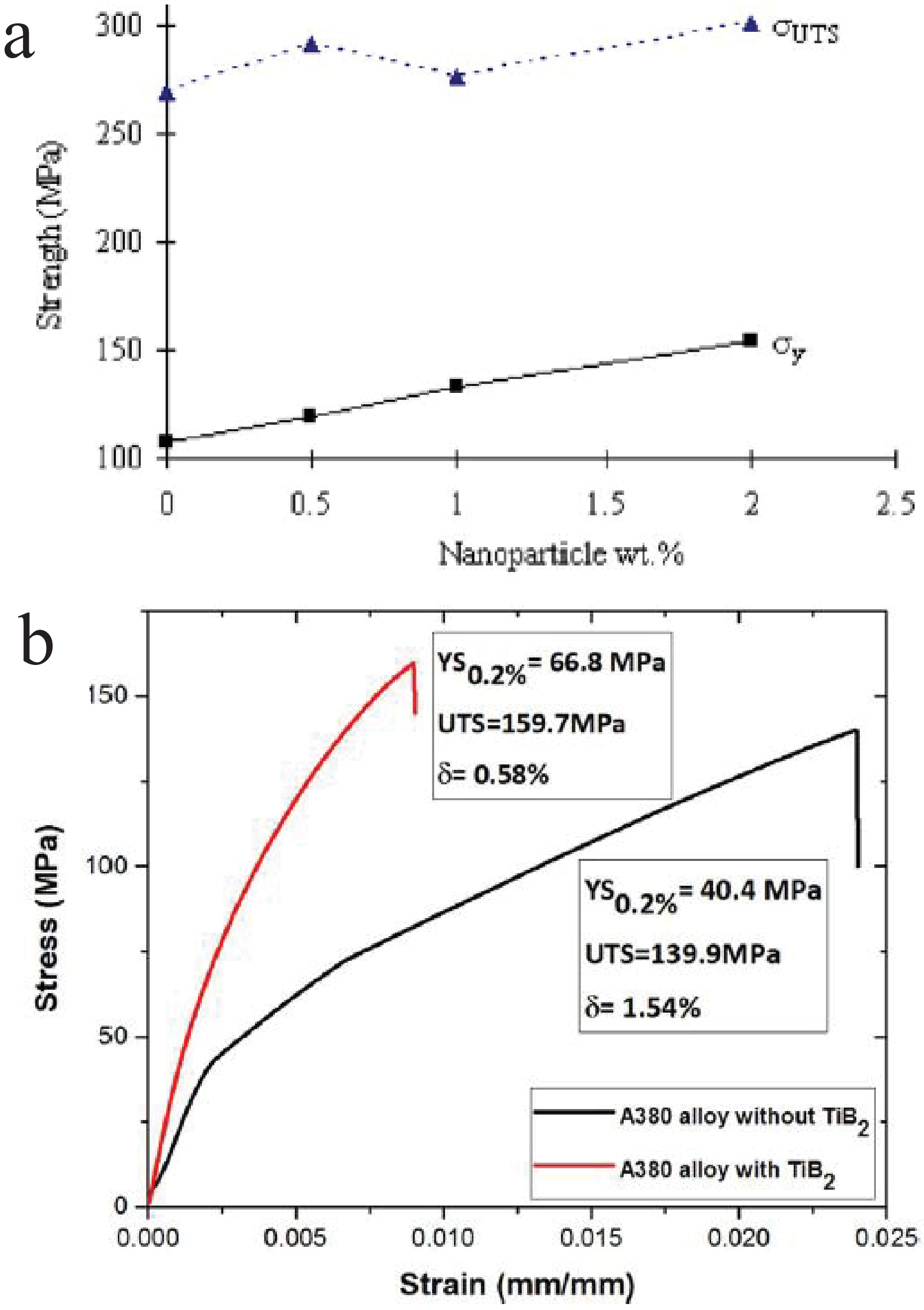

Fig. 1.33: Effect of nano-reinforcement on the tensile strength of Al composites, (a) SiC [76], (b) TiB_2 [96].

In nanocomposites, nanoparticles act as a barrier for the movement of dislocations, known as Orowan strengthening [97]. In addition, in-situ formed TiB_2 nano-particles could refine the grain size of Al matrix [96]. As indicates by Hall-Petch relationship, finer grains results in higher yield strength [74]. In Orowan strengthening mechanism, nano-particle pin down the dislocation lines and generate the Orowan loops around the particles, and the induced stress resistance can be expressed as:

$$\sigma_0 = \frac{0.13\mathrm{Gb}}{\lambda} \ln\frac{\mathrm{r}}{\mathrm{b}} \tag{1.19}$$

where, G is the shear modulus of material, b is the Burger's vector, and r is the average radius of nanoparticles assuming them as spherical shape. The distance λ between the particles can be calculated by:

$$\lambda = \frac{4(1-\mathrm{f})\mathrm{r}}{3\mathrm{f}} \tag{1.20}$$

where f is the volume fraction of particle. According to equation 1.3, the distance between the nanoparticles decreases with increasing the content of reinforcement. The reduction of the distance between the nanoparticles will result in an increase in the required stress τ_0 for forcing dislocations move among the reinforcement particles as indicted in equation 1.4, thus the overall strength of material is increased.

$$\tau_0 = \frac{\mathrm{Gb}}{\lambda} \tag{1.21}$$

It is evident that the smaller the particles and the greater their contribution to the strengthening through the Orowan process. However, the effectiveness of Orowan strengthening significantly degrades due to the presence of particle agglomeration or clusters.

Finally, the increase in strength can also be attributed to the mismatch in CTE values of matrix and reinforcement. The metal matrix has higher CTE values than those of ceramic reinforcement. During cooling stage of process, thermal stress resulting from the difference in CTE can be released by generating the dislocations in the vicinity of the interface. Those dislocations may contribute the hardening of the materials [95, 98].

1.3 Summary

In the microelectronic industry, effective thermal management solutions are challenging facing the increasing power density of electronic components. MMCs reinforced with carbon materials have shown attractive thermal properties (high TC and tailored CTE) that may meet the requirements of microelectronic industry. Among them, the development of Al/G_f composites was reviewed. Several methods to orient G_f were highlighted, in which flake powder metallurgy and step-by-step powder filling method were the most effective. Quantitative characterization of G_f orientation can be carried out by image analysis or polarized Raman spectra. The interfacial states between the matrix and G_f have a considerable effect on the thermal and mechanical properties of composites. The anisotropy in thermal properties and poor mechanical strength are still the big issues for the composites considering their use as heat sink or heat spreader. The metal matrix reinforced with nanoparticles can be an effective solution to enhance strength of the composites without losing too much TC.

In terms of the literature review, in this work we aimed to develop an Al matrix composite reinforced with low-cost and easily machinable graphite flakes (hereafter called Al/G_f composite) with controlled orientation of G_f, the high TC, tailored CTE close to 6×10^{-6}/K, as well as improved mechanical properties.

Chapter 2

Achieving the theoretically predicted highest TC of the Al/G_f composites with highly orientated G_f

2.1 Introduction

Al is a widely used heat sink material, because of its lightweight (2.7 g/cm^3), high thermal conductivity (TC, 220 W/m.K), and relatively low cost compared with other pure metal candidates, such as Cu and Ag, which has great advantages in the applications of automobile and aeronautic industries. Nowadays, carbon-based materials, such as G_f [23, 28, 36], synthetic diamond particles [99], and short carbon fibres [100, 101], have become the popular reinforcements because of their excellent thermal and/or mechanical properties. High TCs have already been achieved in diamond and G_f reinforced metal matrix composites, while the use of diamond poses the problems of high cost and poor machinability [99, 102]. The orientation of short carbon fibers is still a technical obstacle in order to obtain a high TC due to its anisotropic TC [100, 101]. Among these reinforcements, G_f has the low cost, excellent thermal properties, low weight, and ease to machine making them a promising reinforcement candidate for composites used in electronic industry [23, 28, 37, 38, 51].

Considering the large anisotropic TCs of G_f, the orientation of G_f in the metal matrix is vital to get a high TC along the direction of graphite plane [28, 42, 103]. High alignment of G_f has been realized via liquid route processes, such as infiltration and squeeze casting, because G_f tend to lie on the top of each other due to large ratio of lateral size and thickness. It is also needed to add some separator (e.g. SiC [24], Si [25]) to create space between G_f making metal infiltration achievable. However, those spacers with low TCs may act as obstacles for heat transfers, which is the main disadvantage for securing the high TC of composites [51]. Regarding powder metallurgy routes, the fully orientation of G_f was expected to be acquired by application of uniaxial compression during compacting and sintering [24, 53]. However, it was reported that there were still some misaligned G_f distributed in the Al matrix using spherical Al particles with one-step die filling [38]. One possible solution was presented in Cu/C composites [34, 37], in which the powder loading process was divided into several steps. Additionally, converting the spherical particle into flake one using ball milling enabled to obtain the high orientation of G_f by one-step die filling [38, 44, 57, 59]. This is because the apparent density of metal powders is reduced by changing the shape from sphere to flake

[104], which gives rise to enough space of G_f to complete the alignment parallel to the basic graphite plane during cold compacting. But, ball milling is a time consuming process, and in case of Al matrix composites, it degrades the TC of the matrix due to the increase of oxygen content [38].

Interfacial thermal resistance between the metal matrix and reinforcement dominates the overall TC of the composites, especially for non-wetting or non-reactive systems, such as Cu-C, of which TC can be easily enhanced by introducing an interfacial chemical bonding [57, 59, 102, 105, 106]. For filler with isotropic properties, such as diamond particles, it is necessary to understand the contribution of improved interfacial states to the TC of composites, because the overall TC is determined by the intrinsic TCs of the matrix and reinforcements, and the efficiency of heat transfer across the interface [102, 107]. However, due to the anisotropic thermal properties of G_f as mentioned above, both the alignment and interface states should be considered at the same time in order to tailor the TC of composites. It was reported that the reduction treatment of G_f can increase its quality by changing both the value of d_{002} and surface oxygen content to improve the TC of Cu/G_f composites [56]. Several studies have tried to investigate the effect of interfacial features between the G_f and Al matrix on TC [25, 33], while the effect of the orientation degree of G_f on TC was unclear.

In this chapter, a high orientation of G_f in the Al matrix was achieved via a step-by-step powder filling method using the spherical Al powder. Based on this, the effects of sintering temperature and Ar + H_2 heat treated G_f on TC were investigated, which was analyzed in terms of the interfacial configurations by electron microscopy and effective medium approximation (EMA) approach.

2.2 Powder mixing and filling process

As shown in Fig. 2.1, the starting materials were a gas-atomized Al powder (ULTD0065, Hermillon powders, France) with the average particle size of around 10 μm, and G_f powder (Purchased from Yanxin-Graphite Co., Ltd.) with the diameter and thickness of around 550μm and 30 μm, respectively. Selected physical properties of Al powder and G_f were given in **table 2.1**. The G_f was first ultrasonically washed in ethanol for 10 min, filtered by filter paper and dried in a drying chamber. A small batch of G_f was heat treated in the Ar + H_2 atmosphere (95% Ar + 5% H_2). Specifically, 10 g of G_f was put on an alumina pod and then placed in the center of a tubular furnace chamber. The furnace was heated at 6 °C/min to the bearing temperature of 400 °C, maintained for 1 h, and then cooled down by switching off the powder. The Al powder was homogenously mixed with G_f using a resonant acoustic mixer (RAM) for 10 s with an acceleration of 70 g (LabRAM, Butte, Montana, USA; Fig. 2.2), in which the volume fraction of G_f was fixed at 40 vol.%. RAM, different from conventional techniques, can improve mixing efficiency and performance, especially in reduction of mixing time and homogenization of powder [108].

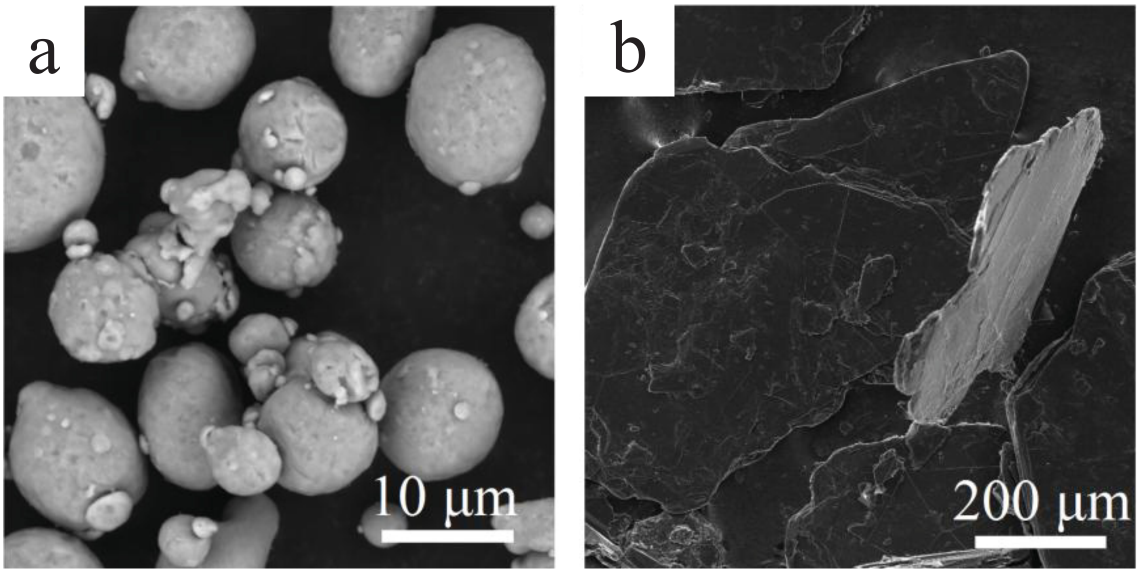

Fig. 2.1: SEM micrographs of the starting materials: (a) spherical Al powder, (b) G_f.

Table 2.1 Selected physical properties of Al powder and G_f

	ρ (g/cm³)	K (W/m.K)	C_p (J/Kg.K)
Al (sphere)	2.7	220	921
Graphite	2.25	1000 [30]	836

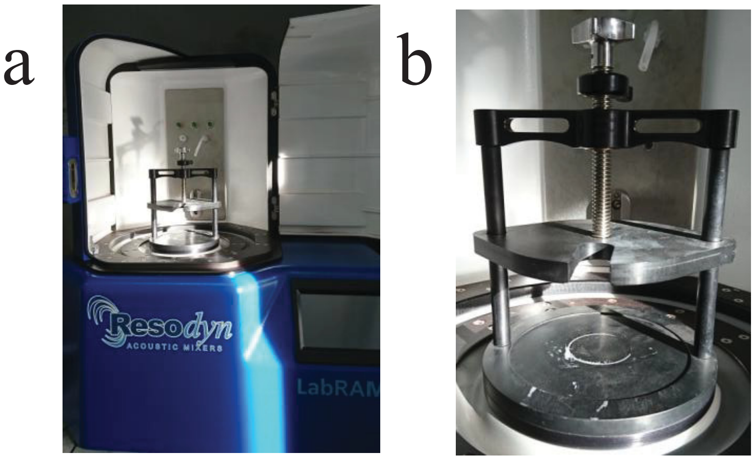

Fig. 2.2: Photographs of (a) the resonant acoustic mixer and (b) the holder to fix the mixing vessel.

Quantity of the Al/G_f powder mixture for one specimen was calculated according to both the final size (Φ40 mm × 7.5 mm) of sample and theoretical density obtained by rule of mixtures. A small amount of powder was filled in a graphite die (Fig. 2.3) and compacted under a uniaxial pressure of 2 MPa with the aid of hand-pressing machine, in which the thickness of powder layer is smaller than 1 mm. Thus, this step was repeated until all the mixture was put into the die. A graphite paper was used to separate the powder mixture and graphite die in order to remove the composite easily after sintering. For comparison, the same amount of mixture was also loaded in the die in one step and compacted by vacuum hot pressing (VHP).

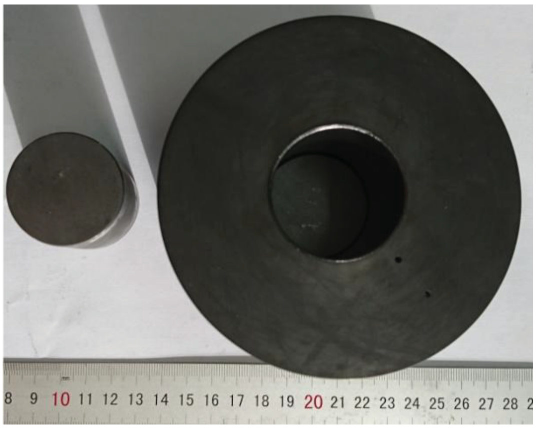

Fig. 2.3: Photograph of the graphite die and piston.

2.3 Sintering, sectioning, and polishing of the Al/G_f composites

Fig 2.4 shows the photograph and schematic illustration of the VHP equipment. A typical VHP facility includes the heating system (induction heating), vacuum pump, sintering chamber (Fig 2.4b), and hydraulic machine. The sample was sintered at a temperature lower than its melt point with a uniaxial pressure under vacuum. Our cylindrical bulk composites (Φ40 mm × 7.5 mm) were fabricated via VHP under the conditions of 1.5 × 10^{-1} mbar, 60 MPa, 30 min, and different sintering temperatures (580 °C, 600 °C, 620 °C, and 640 °C). Temperature was monitored by a K-type thermocouple positioned in the hole located close to the cavity of the graphite mold. Here, hot pressing direction was noted as z, while x, y was the basic plane.

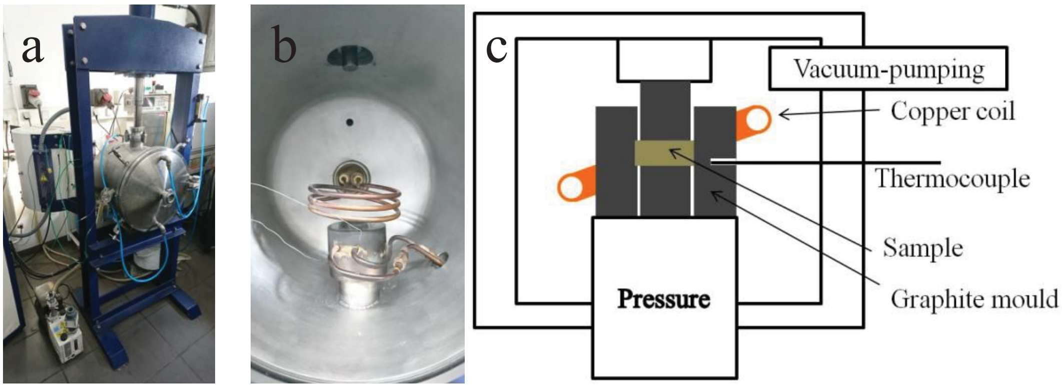

Fig. 2.4: Photographs of (a) overview, (b) sample chamber interior and (c) schematic illustration of the VHP facility.

The as-sintered dense Al/G_f composite was polished on both sides, (Fig. 2.5a), then it was sectioned by a diamond wire saw along the plane parallel to the pressing direction, as illustrated in Fig. 2.5b-c. One slice of sample with the thickness of around 2 mm was mounted in resin used for micrograph analysis (Fig. 2.6a). Grinding was carried out using a rotating disc covered with SiC paper and water. The grinding SiC paper sequence was Struers P500, P800, P1000, and P1200, and each step lasted for 10 sec. A cloth impregnated with Struers water-based diamond suspension (9 µm, 3 µm, and 1 µm in three stages) was used for polishing with each stage of lasting 6 min. Final polishing was done using silica suspension.

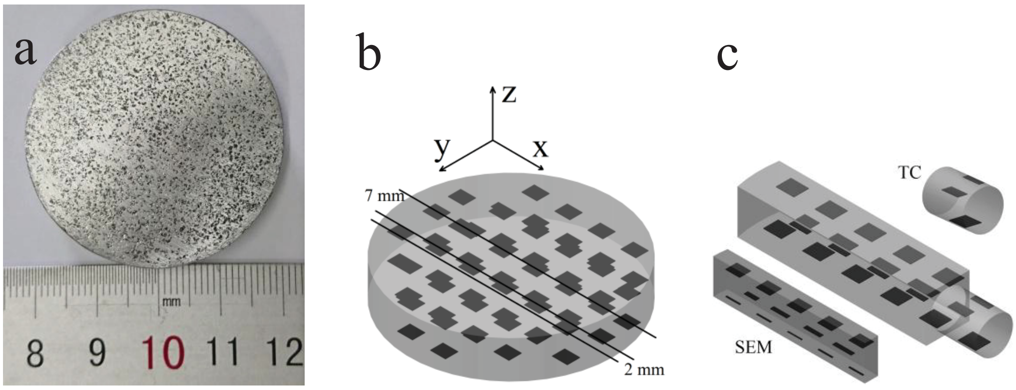

Fig. 2.5: (a) Photograph of the Al/G_f composites fabricated by VHP, schematic illustrations of (b) sectioning and (c) machining of samples for characterizations.

One slice of sample with the thickness of 7 mm was machined into a cylinder shape with the diameter of 6 mm, and then cut into small pieces with thickness more than 4 mm used for thermal diffusivity measurements. Up and down sides of cylinder is required to be highly parallel. However, those two ends were very coarse and rough after being cut by the diamond wire saw. A graphite carrier (Fig. 2.6b) was used to fix the sample on an aluminum holder in order to obtain a right cylinder (Φ6 mm × 4 mm, Fig. 2.6c).

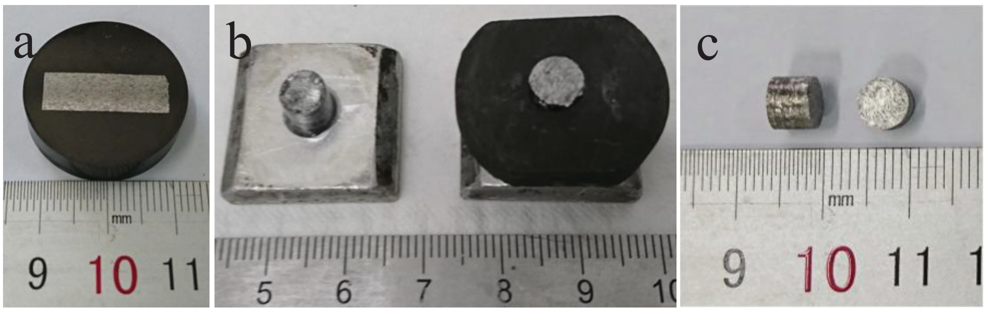

Fig. 2.6: Photographs of the G_f/Al composite samples used for characterizations, (a) the mounted sample, (b) carriers used for polishing samples (c) samples for thermal diffusivity measurement.

2.4 Microstructure characterization of the Al/G_f composites

Microstructure analysis were performed using scanning electron microscopy (SEM) (Tescan, VEGA$^{©}$) at the cross-section perpendicular to x, y plane. Fig. 2.7 shows the typical cross-sectional SEM micrograph of the Al/40 vol.% G_f composite using the one-step powder filling method. Dark regions represent the graphite flakes, and continuous gray one is the Al matrix. Most of G_f orient along the horizontal direction, while there are still quite a few G_f distribute randomly, in which some even orient along the pressing direction. Since this sample was fabricated by one step powder loading process, certain random arrangement of G_f after the mixing process remained in the composite even after hot pressing. Although the application of uniaxial pressure can result in the alignment of G_f during hot pressing [28], our work proved that application of uniaxial pressure is not sufficient to achieve fully orientation of G_f, which is consistent with the previous report [38]. Such misaligned G_f would have a negative effect on obtaining a high TC along the basal plane of graphite.

Fig. 2.8 shows the SEM micrographs of the Al/40 vol.% G_f composites fabricated at the different sintering temperatures. It should be reminded that the magnification of each image could cover the size of sample used for thermal diffusivity measurement (5 mm × 4 mm). High alignment of G_f in the Al matrix can be observed in each image owning to the step-by-step powder loading method. It implies that the misalignment of G_f can be avoided by controlling the thickness of each layer when filling powder. The effect of the different sintering temperatures on the alignment of G_f is negligible.

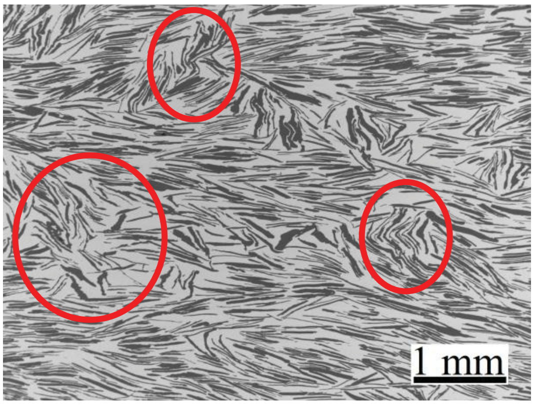

Fig. 2.7: SEM micrograph of the Al/40 vol.% G_f composite obtained from the one-step powder filling method.

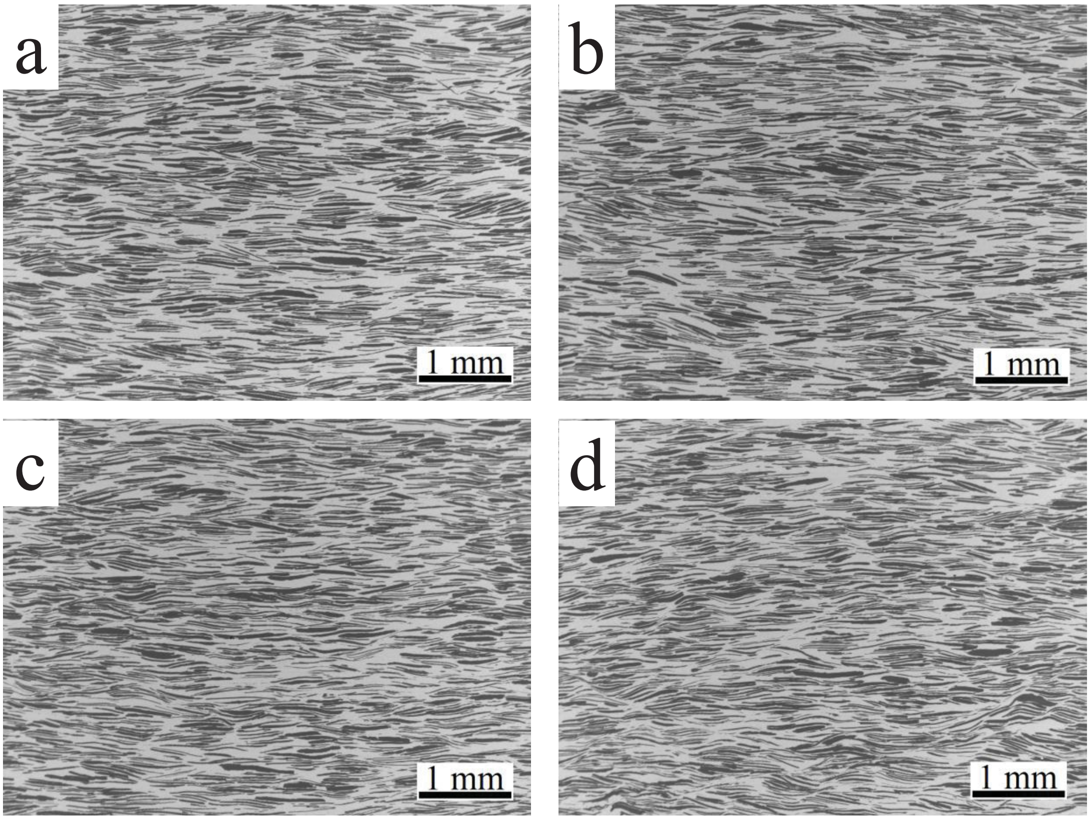

Fig. 2.8: Typical SEM micrographs of the Al/40 vol.% G_f composites using the step-by-step powder filling method and sintered at the different temperatures of (a) 580 °C, (b) 600 °C, (c) 620 °C, (d) 640 °C.

X-ray diffraction (XRD) was carried out by a PANalytical X'pert PRO MPD diffractometer using Cu Ka radiation (k = 0.15418 nm), and each measurement was set within an angular range of 2θ of 8° – 80° at the scanning speed of 1° /min. Besides, one more XRD measurement was carried out at the low scanning rate of 0.2° /min in the range 30° - 38° in order to detect the possible existence of Al_4C_3 in the sample sintered at 640 °C.

Fig. 2.9 exhibits XRD patterns of the Al/40 vol.% G_f composites fabricated at the different sintering temperatures. It shows the diffraction peaks of Al and graphite with no visible difference among all the four samples, while no peaks of Al_4C_3 are found at this macroscopic scale as shown in the inset. In addition, The diffraction peak at about $2\theta = 26.5°$, corresponding to (002) crystal plane of hexagonal graphite, has the relatively weak intensity indicating that G_f have the high orientation arrangement [51].

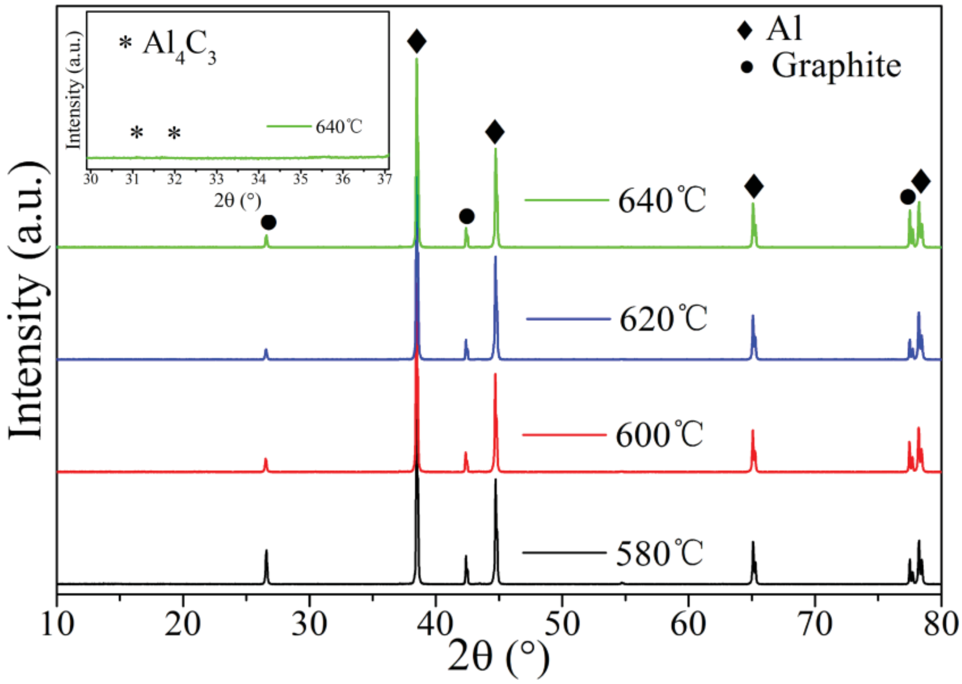

Fig. 2.9: XRD patterns of the Al/40 vol.% G_f (as received) composites obtained using the different sintering temperatures of 580 °C, 600 °C, 620 °C and 640 °C.

A high purity Si powder was used as the reference to calibrate the diffraction peak position of d_{002} of G_f to measure its graphitization degree [109]. Standard Si powder in the particle size range 25 µm – 50 µm was obtained through pulverizing a single crystal of Si following by screening with 325 and 500 mesh standard sieves. Both as-received and H_2 treated G_f were mixed with 20 wt.% of Si powder. The XRD peak profile was obtained by the continuous scanning method, where the scanning rate of the counter and angular range were 0.25° /min and 25° – 30°, respectively [110].

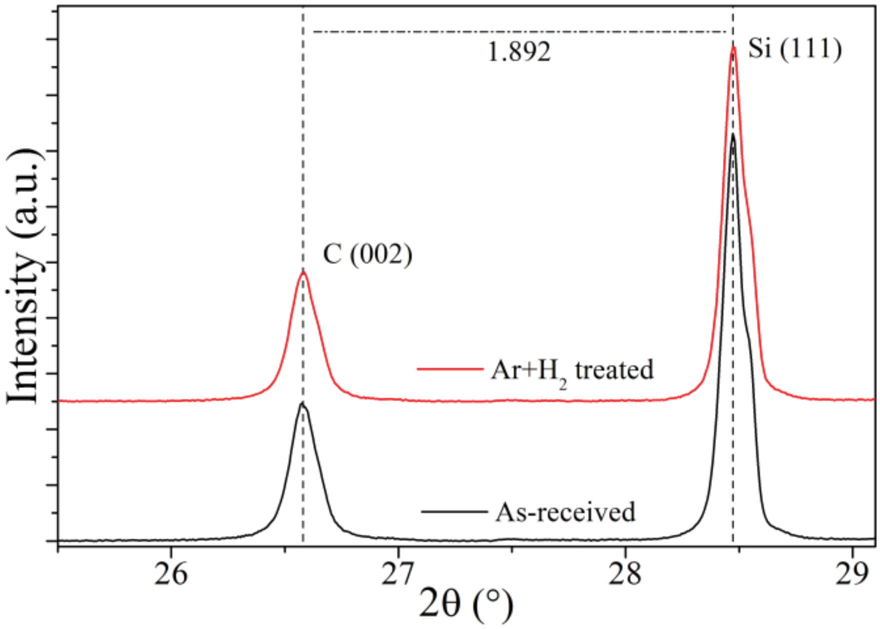

Fig. 2.10: XRD patterns of G_f mixed with standard Si powder before and after reduction treatment.

Fig. 2.10 shows the XRD patterns of G_f and silicon powder mixtures. The peak d_{002} of G_f was corrected by the peak 111 of Si using the following equation [109]:

$$2\theta_{Si} - \delta_{Si-C} = 2\theta_C \tag{2.1}$$

where $2\theta_{Si}$ is 28.443° for standard silicon power. δ_{Si-C} was measured from the Fig. 2.10, which is 1.892. Indeed, this value is the same for as-received and H_2 treated G_f. The inter-planar of d_{002} was calculated using Bragg's equation with $2\theta_C$ value originated from Eq. (2.2):

$$d = \lambda/2\sin\theta_C \tag{2.2}$$

The calculated d_{002} is 0.3357 nm, which is very close to 0.3355 nm for high-quality graphite [111]. Note that the smaller d_{002} and the higher degree of graphitization of G_f [112]. Thus, the result indicates that the graphitization degree as well as intrinsic TC of G_f maintained unchanged after applying H_2 heat treatment at 400 °C.

The as-received and H_2 treated G_f was also characterized by Raman spectroscopy. The Raman analysis was performed with a high-resolution Horiba spectrometer equipped with a 532 nm laser in a backscattering micro-configuration, whose accuracy is equal to 0.1 cm^{-1}. The laser power was kept in the range between 5 and 10 mW to avoid local heating. All the tests were carried out at room temperature with a 50× objective having a laser spot size of about 400 nm. Single and multi-peak fittings of selected Raman bands were done using Gaussian and Lorentzian functions after background subtraction in Fityk 1.3.1 software.

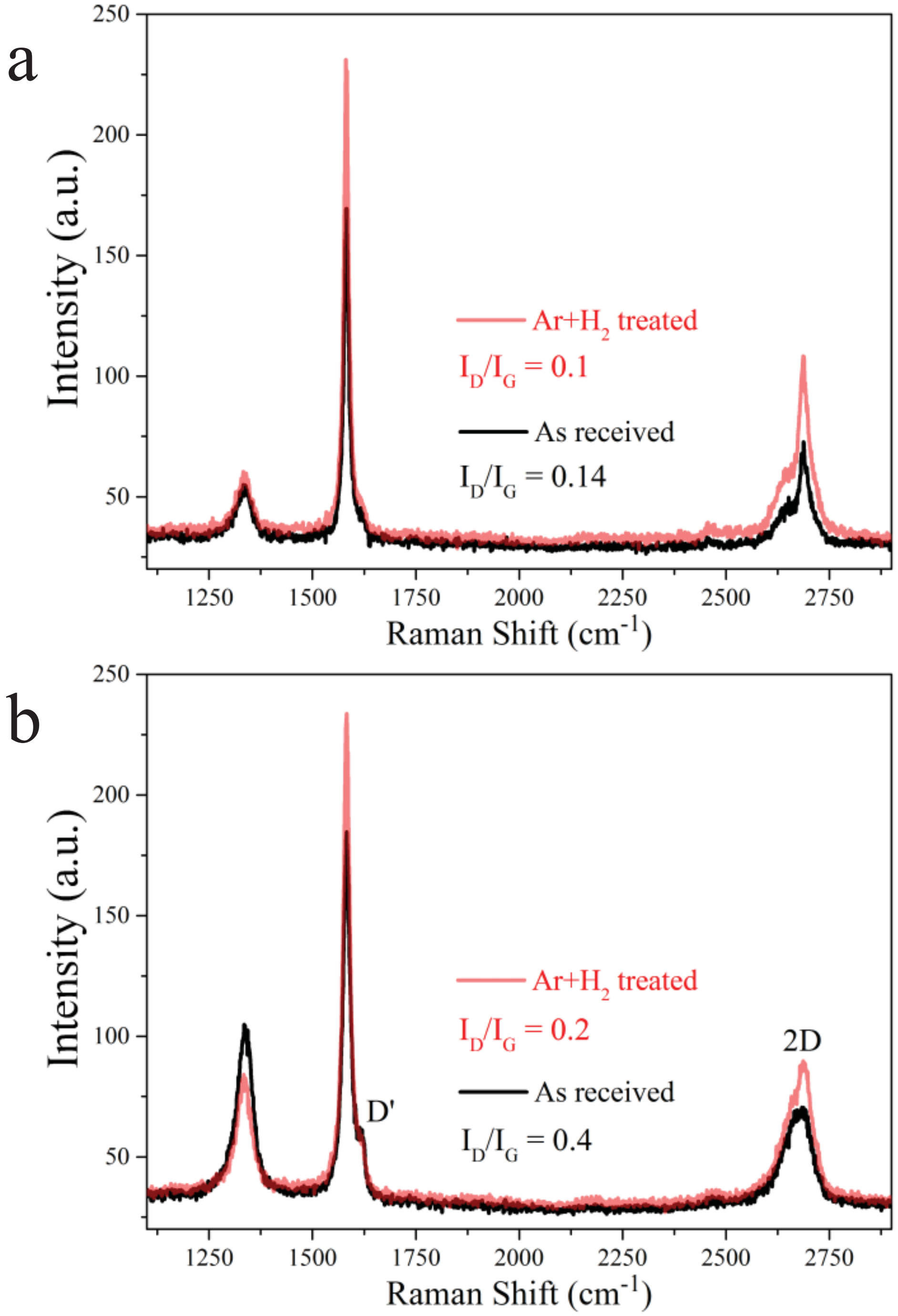

Fig. 2.11: Raman spectra recorded from the (a) center and (b) edge areas of the as-received (black) and H_2 heat treated (red) G_f.

Fig. 2.11 shows the Raman spectra collected in both center and edge areas of as-received and H_2 + Ar heat treated G_f. G band appears around 1580 cm^{-1} corresponding to sp^2-C network. The D and D’ bands are located around 1350 cm^{-1} and 1620 cm^{-1}, respectively, which result from the introduction of defects into the C-lattice. And, 2D band, also called G' band, appears around 2720 cm^{-1}. The ratio I_D/I_G has usually been applied to indicate the concentration of defects in the graphite [113-117]. Our results show that the ratio on the edge of G_f decreases from 0.4 ± 0.1 to 0.2 ± 0.03 after H_2 + Ar heat treatment, while the one in the center of G_f is nearly independent on heat treatment and lower. Moreover, $I_D/I_{D'}$ was calculated to be around 0.3 for both samples, which indicates existing defects can be classified as boundary-like type [115]. Thus, the decrease of defects on the edge of graphite would enhance the heat transport carried by phonons as well as improve the interface thermal dissipation efficiency between Al and graphite.

2.5 Thermal characterization of the Al/G_f composites

TC determines the heat dissipation ability of a material, which is a critical feature for heat sink applications. TC value was acquired by means of thermal diffusivity measurement using the following equation.

$$K = \alpha \times \rho \times C_{p,c} \tag{2.3}$$

where K, α and ρ represent TC in W/m.K, thermal diffusivity, and density of composite, respectively. $C_{p,c}$ is specific heat capacity of composite calculated by rule of mixture:

$$C_{p,c} = V_m C_{p,m} + V_r C_{p,r} \tag{2.4}$$

in which $C_{p,m}$ and $C_{p,r}$ are the specific heat capacity of Al matrix and reinforcements, respectively. V_m and V_r are the volume fraction of the Al matrix and reinforcement, respectively. The density of composites was measured using a device based on Archimedes' principle and calculated by a formula as follows.

$$\rho_c = \frac{w_{air}}{w_{air} - w_{water}} \times \rho_{water} \tag{2.5}$$

in which w_{air} and w_{water} are the weight of sample measured in air and in water, respectively. ρ_{water} is density of water (1 g/cm^3). The relative density is the ratio between the experimental and theoretical density, where theoretical one is calculated through the rule of mixture.

$$\rho_c = V_m \rho_m + V_r \rho_r \tag{2.6}$$

where ρ_c, ρ_m, and ρ_r are the densities of composite, Al matrix, and G_f, respectively. V_m and V_r are the volume fraction of Al matrix and reinforcement, respectively.

Thermal diffusivity was measured via laser flash method (NETZSCH® LFA 457, Microflash) at 70 °C. The sample was usually coated with black carbon on both surfaces (Graphite 33). Fig. 2.12 shows a photograph and schematic principle of laser flash apparatus. A short laser pulse heats the lower surface of the sample (Fig. 2.12b). The resulting temperature change on the upper surface of sample is then determined by an infrared detector. The typical curve of the signals is shown in Fig. 2.6c. The thermal diffusivity is calculated via the formula [118]:

$$\alpha = 0.1388 \times \frac{d^2}{t_{1/2}} \tag{2.7}$$

where d is the thickness of sample and $t_{1/2}$ is the time at half signal height.

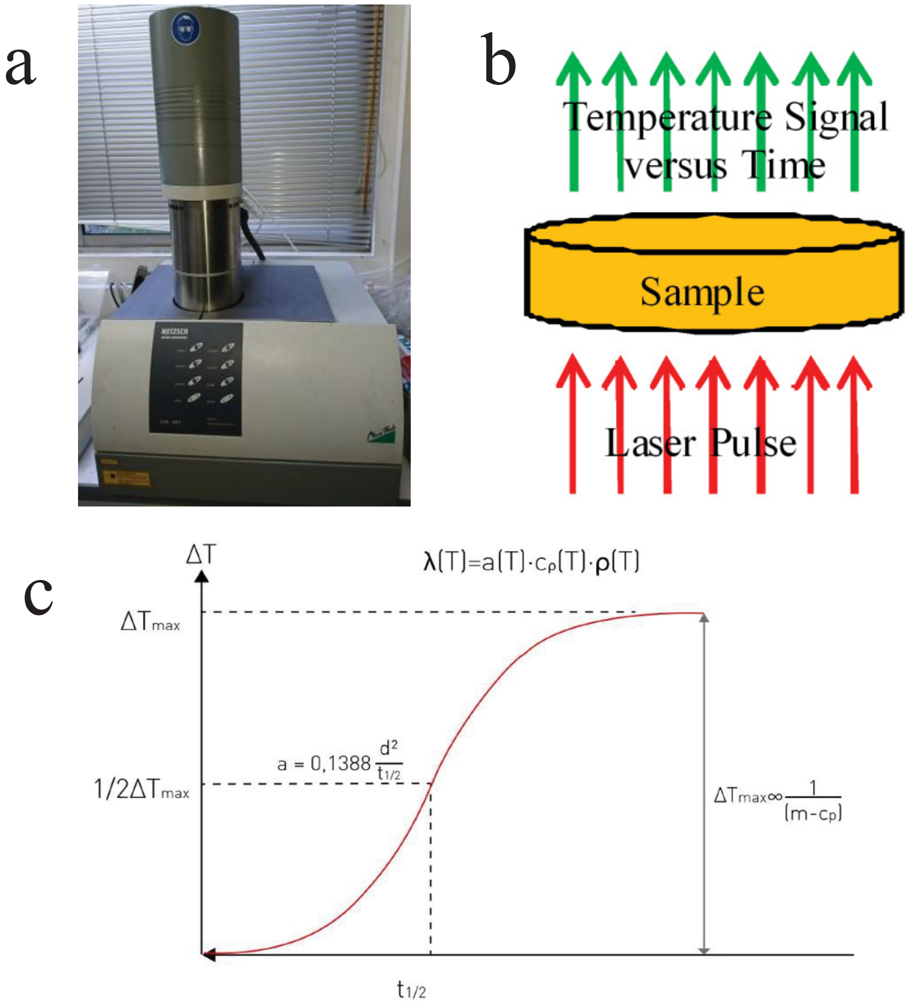

Fig. 2.12: (a) Photograph of the flash laser apparatus, (b) schematic illustration of the thermal diffusivity measurement, and (c) temperature change as a function of time.

2.6 Theoretical TC and its correlation with the orientation degree

Generally, there are various factors affecting TC, such as the intrinsic thermal properties, shape, filler sizes, orientation, volume fraction of reinforcements, and interfacial thermal conductance between matrix and reinforcement. There is a classical model that considers all those factors called effective medium approximation (EMA) [46]. The formulations of in-plane ($K_{//}$) and through-plane ($K_{\perp}$) TC are defined as follows:

$$K_{//} = Km\frac{2+f[\beta_L(1-S_L)(1+\langle\cos^2\theta\rangle)+\beta_T(1-S_T)(1-\langle\cos^2\theta\rangle)]}{2-f[\beta_L S_L(1+\langle\cos^2\theta\rangle)+\beta_T S_T(1-\langle\cos^2\theta\rangle)]} \tag{2.8}$$

$$K_{\perp} = Km\frac{1+f[\beta_L(1-S_L)(1-\langle\cos^2\theta\rangle)+\beta_T(1-S_T)\langle\cos^2\theta\rangle]}{1-f[\beta_L S_L(1-\langle\cos^2\theta\rangle)+\beta_T S_T\langle\cos^2\theta\rangle]} \tag{2.9}$$

in which

$$\langle\cos^2\theta\rangle = \frac{\int\rho(\theta)\cos^2\theta\sin\theta d\theta}{\int\rho(\theta)\sin\theta d\theta} \tag{2.10}$$

$$\beta_i = \frac{K_i-K_m}{K_m+S_i(K_i-K_m)},\quad (i = L, T) \tag{2.11}$$

$$S_L = \frac{\pi t}{4D},\quad S_T = 1-\frac{\pi t}{2D} \tag{2.12}$$

The subscripts L and T are noted as the in-plane and through-plane directions of G_f, respectively. f is the volume fraction of fillers, and S is the geometrical factor, where D and t are the diameter and thickness of the filler, respectively. K_m is the TC of Al, K_i is the intrinsic TC of G_f, and K_m, K_L, and K_T are 220, 1000 [28], and 10 $W.m^{-1}.K^{-1}$ [119], respectively . The item of $\langle\cos^2\theta\rangle$ represents the alignment degree of reinforcements in the matrix. With the full orientation of G_f along the in-plane direction of the composite specimen, $<\cos^2\theta>$ is equal to 1, and for the completely random distribution of G_f, $<\cos^2\theta>$ is equal to 1/3 [47, 120, 121]. $\rho(\theta)$ is a distribution function describing the orientation of G_f in the matrix. θ is the angle between the basal graphite plane and the x,y plane of the composites.

2.6.1 Orientation degree analysis

An image analysis technique [47, 103] was used to make statistics about angle θ distributions of G_f, which was processed via ImageJ software. Firstly, cross-sectional SEM micrographs of Al/G_f composites (Fig. 2.7 and 2.8) were converted to black-and-white images using a constant threshold value (see two examples in Fig. 2.13). It should be noted that some G_f may stick together after such processing making the software hard to identify an individual one, so they were divided manually. Then, statistical measurement of the angle θ of each flake was completed by the software based on black-and-white contrasts.

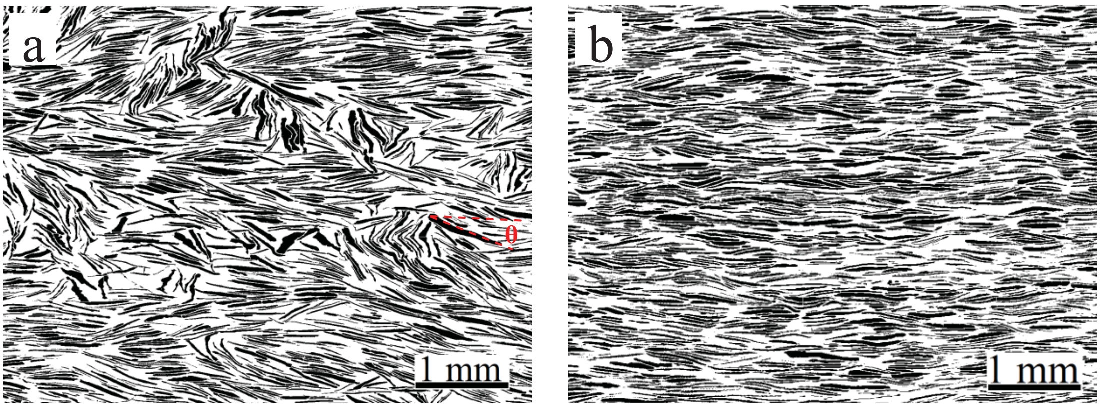

Fig. 2.13: Black-and-white contrast images converted from experimental SEM micrographs of Al/40 vol.% G_f composites by ImageJ software: the sample using (a) the one-step powder loading and (b) the step-by-step powder loading.

The distribution of angle θ was presented as the frequency (the number of G_f at certain θ in all the G_f) versus θ plots, as shown in Fig. 2.14, in which it contains the fittings of angle distribution. Here, an ExpDec 1 function $\rho(\theta)$ was used to fit the curves using the Origin software [47, 120].

$$\rho(\theta) = A_1 e^{(-\theta/t_1)} + y_0 \tag{2.13}$$

where A_1, t_1 and y_0 are the fitting variables. After the fittings, the specific $\rho(\theta)$ was obtained, and $<\cos^2\theta>$ values of each considered picture can be calculated through numerical integration (insets in Fig. 3.14).

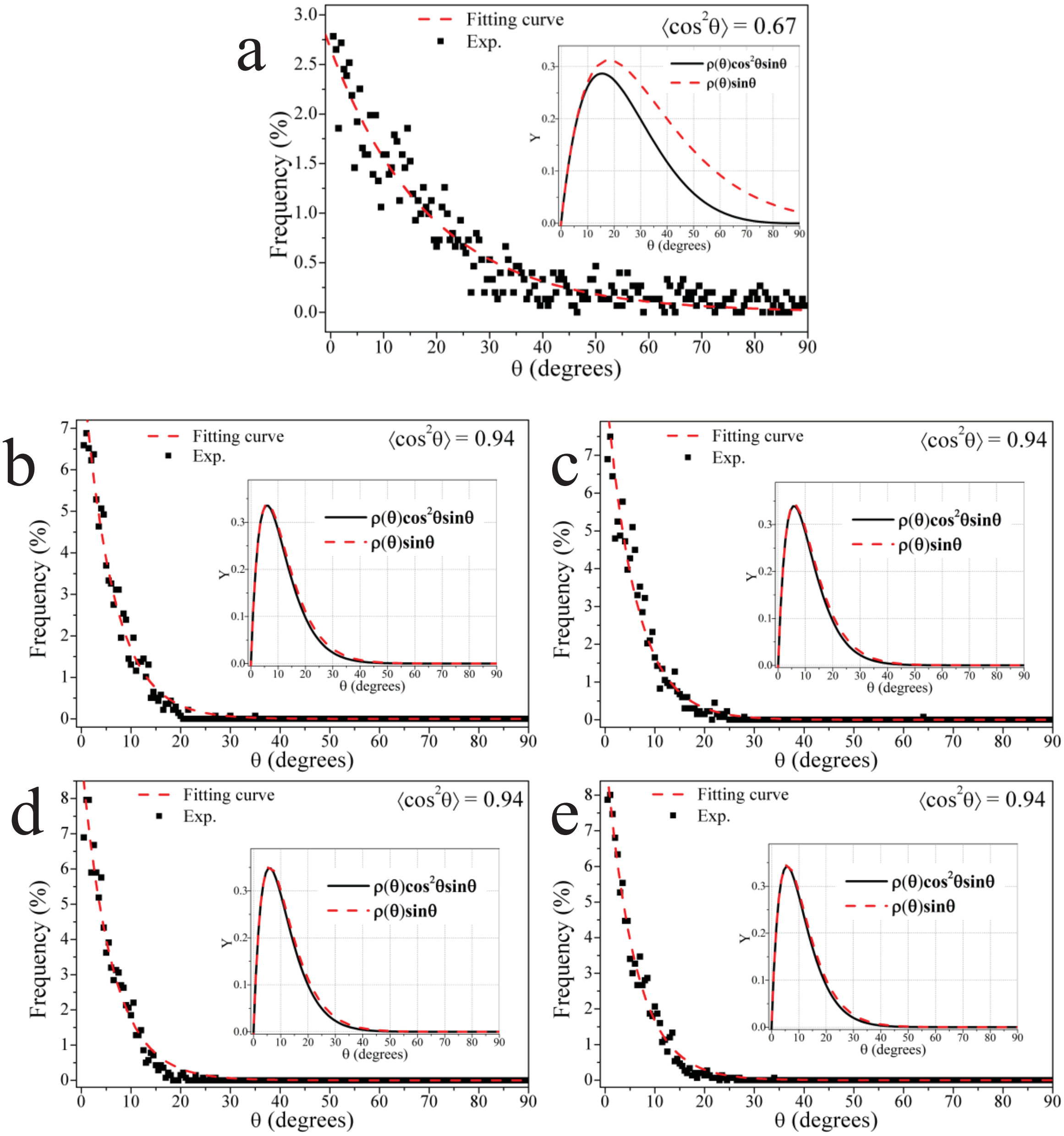

Fig. 2.14: Distribution plots of the angle θ between the graphite basal plane and the x,y plane of the composites sintered at the different temperatures and their corresponding determination of <cos^{2}θ> as insets: (a) 620 °C fabricated by the one-step powder filling; (b) 580 °C, (c) 600 °C, (d) 620 °C, and (e) 640 °C fabricated by the step-by-step powder filling, plots were fitted by the "nonlinear curve fit" process by Origin software.

Fig. 2.14a shows that the value of <cos^{2}θ> for the specimen fabricated by one-step powder filling is 0.67, which implies that the alignment of G_f was much closer to random. By contrast, Fig. 2.14b-e shows that <cos^{2}θ> values of the samples fabricated by step-by-step powder filling and sintered at the different temperatures are 0.94, which suggests that they have almost the same and high orientation of G_f. Therefore, it confirmed that such a step-by-step powder filling method can achieve the high orientation of G_f in the Al matrix.

In order to consider the interfacial thermal conductance, the interfacial thermal barrier was introduced via making modification of the intrinsic TC of the reinforcement [63]. The TCs of filler can be treated as an effective TC, and equations are expressed as follows:

$$K_L^{eff} = \frac{K_L}{\frac{2K_L}{hD}+1} \tag{2.14}$$

$$K_T^{eff} = \frac{K_T}{\frac{2K_T}{ht}+1} \tag{2.15}$$

where h is interfacial thermal conductance, which can be acquired using the acoustic mismatch model (AMM) [62]. The expression can be referred to chapter 1, and the values of those material parameters in the expression can be obtained from previous work [38]. Thus, the interfacial thermal conductance of the Al/G_f composites was calculated using equation (8) to 4.6×10^7 W.m^{-2}.K^{-1}.

2.6.2 TC predictions based on EMA model

Fig. 2.15 shows the TC predictions dependence of various factors based on EMA model, which helps to better understand how to tune the TC of composites. Volume fraction of G_f is a remarkable parameter that affects the overall TC of composite. As mentioned above, G_f is a highly anisotropic material such that the orientation is very critical to the enhancement of TC along the basal plane of graphite. Thus, if being highly oriented along the in-plane direction of G_f, TC of composites goes up with increment of G_f content as shown in Fig. 2.15a.

In order to study the effect of interfacial thermal conductance h on TC, this variable was defined as 4.6×10^x W.m^{-2}.K^{-1}, So x is Lg(h/4.6) (Lg is common logarithm). Thus, the theoretical predication of TC as the function of Lg(h/4.6) with fixed volume fraction of G_f at 40 vol.% and the different orientation degrees is shown in Fig. 2.15b using equation (1). It indicates that there is sharp evolution of TC in the range 5 – 7 of Lg(h/4.6), and TC gradually becomes constant after 8 or before 4. As we can see, the calculated value of h based on AMM is 4.6×10^7 W m^{-2} K^{-1}, whose corresponding TC is not reaching the maximum value. On the other hand, when we modified the intrinsic TC of G_f (for example 900 – 1100 W/m.K) with the fixed volume fraction and orientation degree of G_f, as shown in Fig. 2.15c, the trend of the curves appears different starting from the Lg(h/4.6) value of around 6 until after 8 reaching the constant value of TC each. Therefore, at the given volume fraction and orientation degree of G$_f$, the intrinsic TC of reinforcement determines the highest value of TC, and whether it can reach the maximum depending on the h.

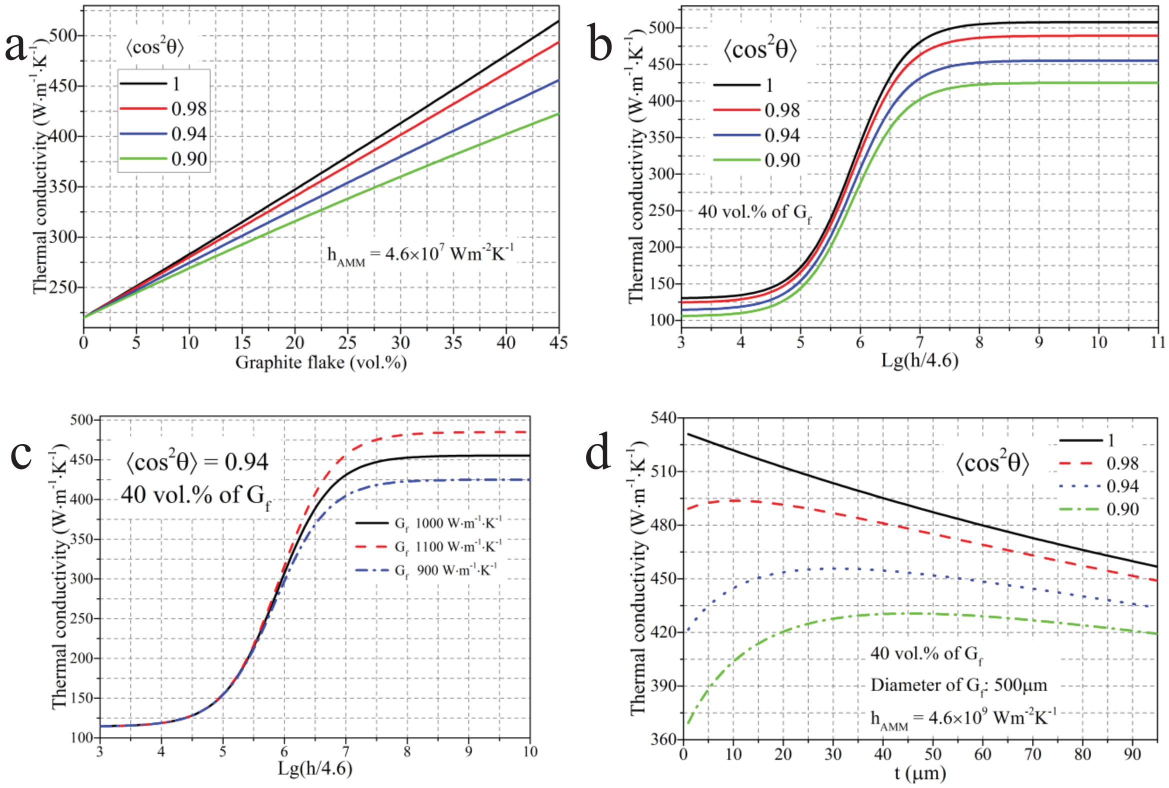

Fig. 2.15: TC predictions as a function of different parameters: (a) G$_f$ volume fraction with different orientation degrees of G$_f$, (b) interfacial thermal conductance with different orientation degrees of G$_f$, (c) interfacial thermal conductance with different intrinsic TC of G$_f$ and, (d) thickness of G$_f$ with fixed diameter of 500 μm under different orientation degrees of G$_f$.

The size effect of G$_f$ on TC is shown in Fig. 2.15d, in which the diameter and volume fraction of G$_f$ are 500 μm and 40 vol.%, respectively. Under the condition of perfect alignment of G$_f$, TC increases with reducing the thickness of G$_f$. However, the value of thickness with respect to the highest TC slightly moves rightward when the orientation degree of G$_f$ degrades from 1 to 0.9. In our experiments, the average diameter of G$_f$ is 500 μm, and the range of thickness corresponding to relatively high TC is 20 μm – 40 μm when the orientation degree of G$_f$ is 0.94. In summary, to get high TC in the Al/G$_f$ composites, the intrinsic TC of matrix and reinforcements should be guaranteed. Meanwhile, highly oriented G$_f$ is much effective to obtain the high TC along the in-plane direction of G$_f$ provide that the interface state between the matrix and reinforcement can be tailored to have high interfacial thermal conductance.

2.6.3 Effect of sintering temperature and Ar + H_2 treated G_f on TC

The composite fabricated via the one-step powder filling method and sintered at the temperature of 620 °C has the TC of 328 ± 45 W/m K with relative density of 98.7 ± 0.3, which is much lower than the TC (439 ± 2 W/m.K) of the sample prepared via the step-by-step powder filling method. The low orientation degree of G_f in this sample was 0.67 (Fig. 2.14a), which can explain the low TC, and the large error of TC also witnesses the inhomogeneous distribution of G_f.

As presented above, our step-by-step powder loading method leads to the relatively high orientation degree $<\cos^2\theta>$ of G_f around 0.94. Fig. 2.16 shows that the increase of sintering temperature has a positive effect on the TC. The value of TC of each condition is an average result measured on four samples, the error bar is the standard deviation of the four TC values. It should be noted that their relative densities are close to 99 % (Fig. 2.16b) despite of the different sintering conditions. Since all the other parameters supposed to be the same, such as starting materials, volume fraction and alignment degree of G_f, there is only one possible factor that may affect the TC of composites fabricated at the different sintering temperatures, which is the interfacial thermal conductance. Moreover, using Ar + H_2 thermal treated G_f also enhanced the TC at the same sintering conditions. However, this enhanced effect becomes weaker at the sintering temperature of 640 °C.

Adrien et al. reported that the intrinsic TC and surface quality of G_f can be improved by heat treatment under H_2 atmosphere [56]. Dash line in the Fig. 2.15c shows the predicted TC with a higher intrinsic TC (1100 W/m.K) of G_f, whose values after Lg(h/4.6) of 8 is higher than that with lower intrinsic TC (900 W/m.K) of G_f. However, it was not reflected in the Fig. 2.16a, in which the TCs of composites with as-received and H_2 treated G_f become close at the sintering temperature of 640 °C. Our Raman analysis and measurement of d_{002} of G_f indicate that H_2 heat treatment only reduces the defects of G_f at the edge rather than leading to the enhancement of its intrinsic TC. Therefore, either Ar + H_2 heat treatment or increase of sintering temperature can be considered to improve the interfacial thermal conductance in the composites so as to increase the TC to some extent. Finally, the TC almost reaches its highest value using our fabrication conditions.

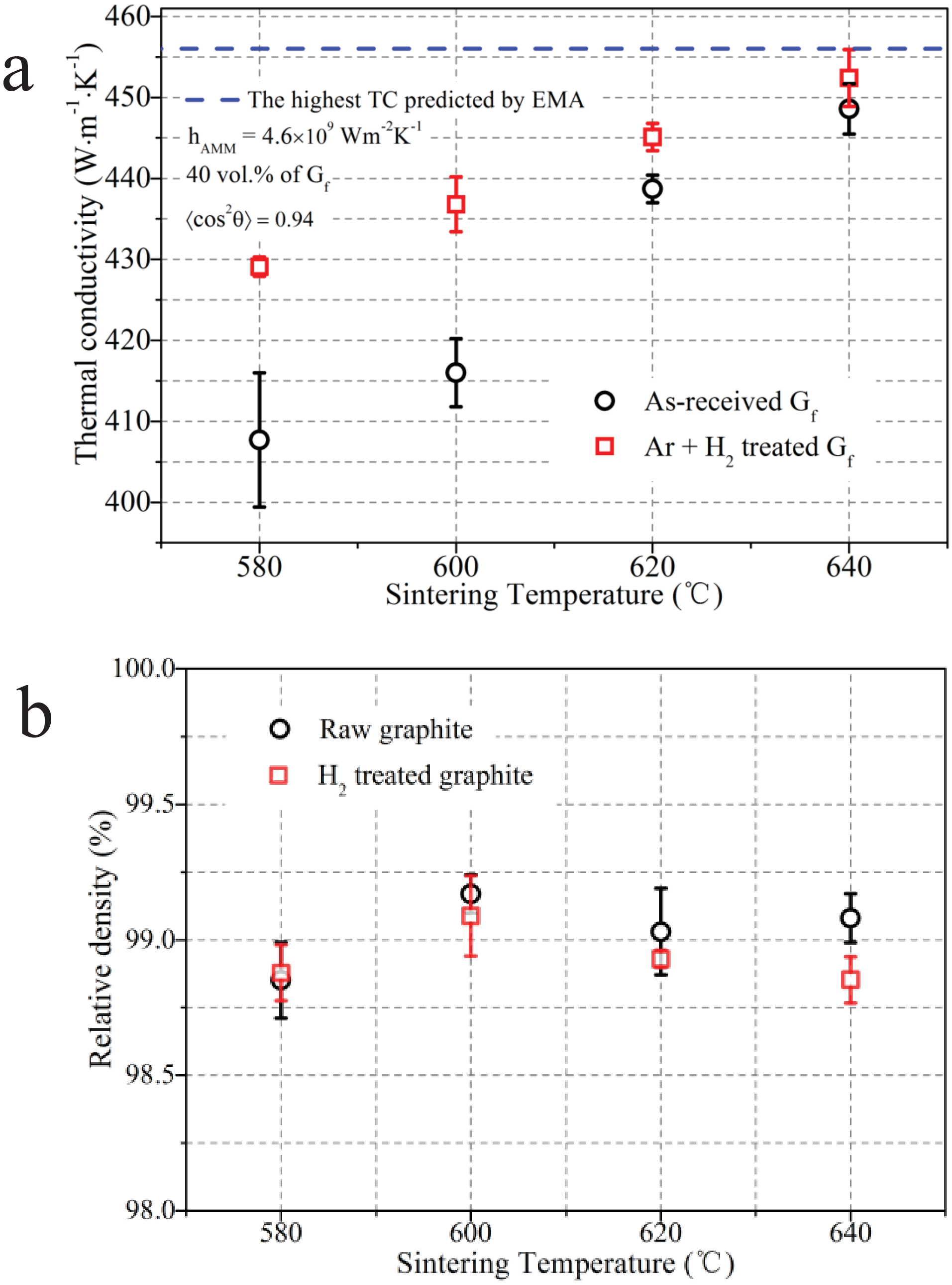

Fig. 2.16: (a) TCs and (b) relative densities of the Al/40 vol.% G_f (as received and thermal treated with Ar + H_2) composites sintered at the different sintering temperatures of 580 °C, 600 °C, 620 °C and 640 °C.

2.7 Interface characterization

Interfacial thermal conductance dominates the overall TC of composites as presented in Fig. 2.15b. A field emission gun SEM (JEOL JSM-7800F) enables to obtain high resolution SEM micrographs providing micro-structural information at the sub micrometer scale. Fig.

2.17 clearly shows there are much more needle-like phases distributed at the interface of Al/G_f composite sintered at 640 °C compared to the one sintered at 580 °C, which can be only one possible reactive product (Al_4C_3) of Al and carbon (i.e. G_f). Increasing processing temperature can enhance the chemical driving force of Al and carbon to form its carbide, especially in melt Al [27, 122]. In our case, increase of sintering temperature can result in more creation of interface product. This suggests more chemical bonding forms between the matrix and reinforcement, which is more beneficial for thermal transfer compared to mechanical one.

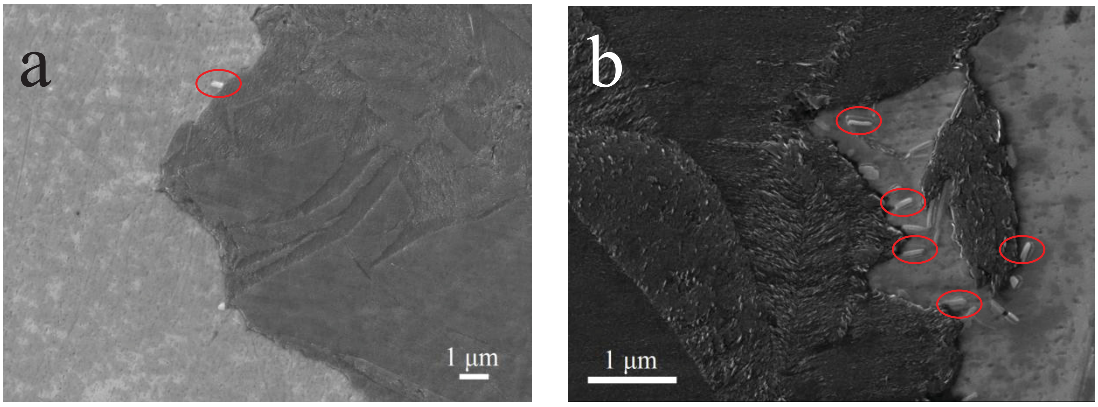

Fig. 2.17: SEM micrographs of the Al/40 vol.% G_f (as-received) composites highlighting the Al-G_f interface area in the samples sintered at the different temperatures of (a) 580 °C and (b) 640 °C.

2.8 Conclusion

Al matrix composite reinforced with G_f has been proved to be a promising heat sink material due to its low cost, high TC. Due also to the high anisotropy of TC in G_f, orientation of G_f in the Al matrix becomes a critical parameter to obtain the high TC along the in-plane direction of G_f. In the present work, such high alignment of G_f was successfully achieved using the spherical Al powder via a step-by-step powder filling method, which is comparable to that by means of flake powder metallurgy [38]. Compared with the TC of sample fabricated using one-step powder filling, it did improve the in-plane TC from 327 to 439 W/m K. Based on the same orientation degree of G_f, increase of the sintering temperature of VHP from 580 °C to 640 °C is able to improve the TC by increasing the interfacial thermal conductance. The results were summarized in the **table 2.2**. Regarding this, suitable chemical bonding by local formation of fine needle-like Al_4C_3 at the Al/G_f interface is beneficial for TC enhancement. On the other hand, using H_2 heat treated G_f further enhances TC at the same sintering temperature, while this enhancement becomes limited at the highest sintering temperature of 640 °C. With the aid of EMA model, the effect of various factors on TC, such as geometry of filler, interfacial thermal conductance between Al matrix and G_f, and intrinsic TC of filler, was established. Above all, the theoretically predicted maximum value of TC (452 W/m.K) was experimentally obtained given the content of G_f of 40 vol.%.

Table 2.2 Summary of TC results of Al/40 vol.% G_f composites sintered at different temperature and their relative density and orientation degree values.

Sintering temperature	580 ℃	600 ℃	620 ℃	640 ℃
TC (W/m K)	408 ± 8	416 ± 4	439 ± 3	449 ± 3
Relative density (%)	98.9 ± 0.1	99.2 ± 0.1	99.0 ± 0.2	99.1 ± 0.1
$\langle\cos^2\theta\rangle$	0.94	0.94	0.94	0.94

Chapter 3

Architecture design of graphite flakes (G_f) in the Al matrix

3.1 Introduction

There are two necessary properties for thermal management applications in the microelectronic industries. A high TC is required to dissipate the excess heat generated by the Si chip, while a low CTE is also fatal to ensure reliability of the electronic device. Since temperature fluctuation occurs during the service of electronic components, the difference in CTE between heat sink and ceramic substrate inevitably induces important thermal stresses. This can lead to the formation of cracks within a solder joint or the ceramic substrate to eventually degrade the lifetime of the electronic devices. Al, a widely used heat sink material, however, exhibits a high CTE value (26×10^{-6}/K), being incompatible with the Si chip (4×10^{-6}/K) or alumina substrate (7×10^{-6}/K). To solve this problem, Al has been reinforced with SiC and some carbon based materials, such as CF [72] and G_f [33, 53], in order to tailor the thermal expansion performance.

G_f has very high anisotropy in CTE (-1×10^{-6}/K in-plane, 28×10^{-6}/K out-of-plane [32]). It was reported that the overall CTE of the aligned Al/G_f composites, along the in-plane of G_f, merely decreases from 25×10^{-6}/K to 22×10^{-6}/K when the volume fraction of G_f increases up to 50 vol.% [33]. Comparatively, the overall CTE along the direction perpendicular to the alignment direction decreases drastically even reaching negative values [53, 68], which cannot be explained by a simple rule of mixture [68, 72].

Therefore, such above-mentioned high anisotropies of the G_f gave rise to major obstacles in fabrication once both TC and CTE should be considered for potential applications. Taking an example of a flat heat sink material pressed against a Si wafer, the high TC should be obtained along the direction parallel (heat spreader effect) and perpendicular (heat sink effect) to the basic plane of Si wafer, while the CTE has to be low and isotropic at least in the basic plane contacting the Si ship to avoid the thermal stress at heating and cooling [123]. However, this configuration of highly oriented G_f along one direction cannot allow to tailor the out-of-plane TC and the in-plane CTE being incompatible with that of the Si wafer. Some researchers [55, 73] have added additional discontinuous CFs into the Al/G_f composite to have a synergetic effect, while this has decreased significantly the TC. To the best knowledge of the authors, no works have been reported to tailor the configuration of thermal properties in the Al/G_f composites via the architecture design of G_f.

This chapter aims at addressing the technical challenge for developing a novel method to achieve the 2D and 3D arrangements of G_f by flake powder metallurgy using a specifically designed punch associated with the step-by-step powder filling process, which opens up a window to design the orientation of G_f. Flake Al powder, compared with other shape of particles, like sphere and dendrite, has a lower apparent density [45], which is of benefit to accomplish the local arrangement of G_f.

3.2 Fabrication of the Al/G_f composites using flake powder metallurgy

Flake Al powder (Al_F) was produced from spherical Al powder (ULTD0065, Hermillon powders, France) by planetary ball milling. 6 g of spherical Al was put in a stainless-steel jar with addition of 5 ml of isopropyl alcohol each time. The weight ratio between spherical Al powders and stainless-steel balls of 5 and 10 mm in diameter was 20:1. The rotation speed was set to 200 rpm. A short time of 30 min was used to acquire the flake shape of Al powder without introducing too many secondary effects like contaminations. After the ball milling process, Al powder mixed with steel balls and isopropyl alcohol was washed using distill water followed by ethanol in an ultrasonic bath, then dried in a vacuum chamber. The micrograph of obtained flake Al is shown in Fig. 3.1a with an average thickness smaller than 1 µm. Fig. 3.1b displays spherical and flake Al powder mixed with 40 vol.% of G_f showing different apparent density, which has a significant effect on the alignment of G_f during compacting. G_f used was the same type as mentioned in chapter 2. The G_f was homogenously mixed with the flake Al powder using a resonant acoustic mixer, in which the volume fraction of G_f was set to 40 %. The mixture was filled into the graphite die in one step using a punch with flat end and compressed with the hydraulic machine.

The Al_F/G_f composites were consolidated via hot pressing under vacuum (1.5×10^{-1} mbar) at the optimized conditions (620 °C, 60 MPa for 30 min). Microstructure characterizations were carried out in the same way as mentioned in chapter 2.3. TC measurement was done as same as mentioned in chapter 2.5.

The deformation of a solid induced by a temperature change ΔT can be described by strain ε whose components are proportional to ΔT [124]

$$\varepsilon = \Delta L/L = \alpha\Delta T \tag{3.1}$$

where α is the CTE, L is the initial length of sample and ΔL is the change of length. The value α at a specific temperature is regarded as the slope of the $\Delta L/L$ vs T curve, while the average α over a temperature range is calculated as $\Delta L/L\cdot\Delta T^{-1}$.

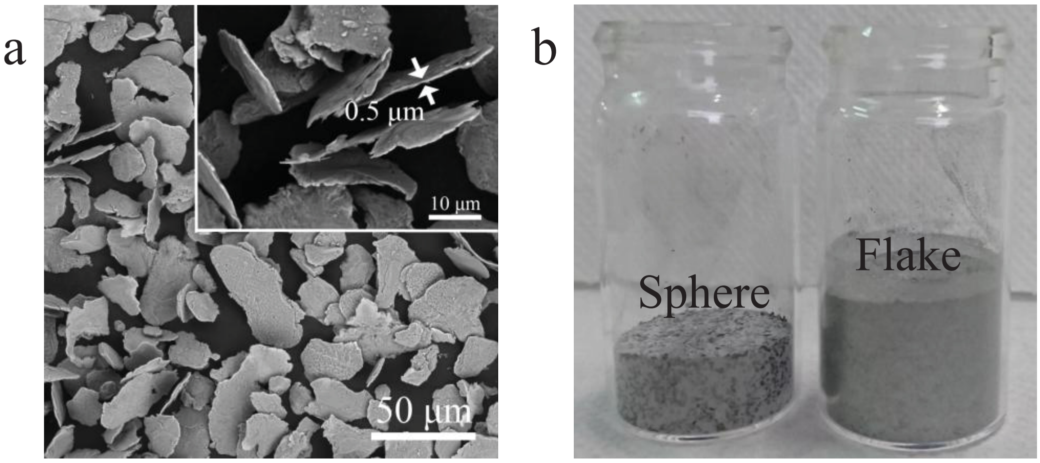

Fig. 3.1: (a) SEM micrographs showing the morphology of as-milled flake Al powder particles, inset highlights the thickness of the powder; (b) Photograph comparing apparent densities between the spherical and flake Al powders, note that the weight of the Al/40 vol.% G_f powder mixture is 3 g for each in the glass bottle.

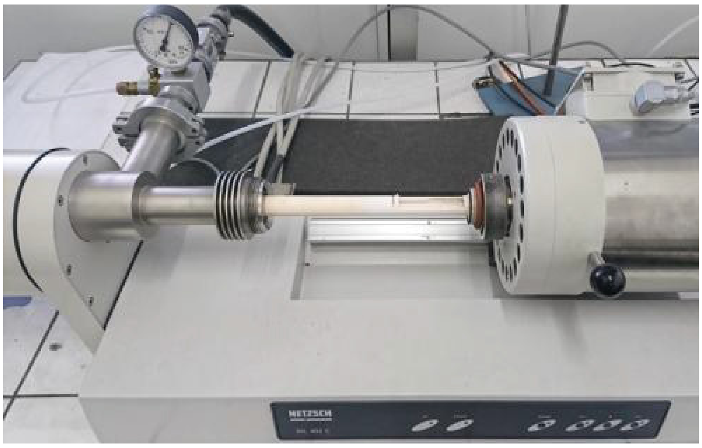

Fig. 3.2: Photograph of the horizontal dilatometer

Thermal expansion behaviours were characterized by a horizontal dilatometer (NETZSCH DIL 402 PC, Fig. 3.2) over a temperature range from 40 °C to 300 °C with the heating rate of 2 °C/min in an Ar atmosphere. The samples used for CTE characterization were cut into a cubic shape ($5 \times 5 \times 5$ mm^3) as shown in Fig. 3.3a. The sectioning process is exhibited in Fig. 3.3b where the CTE values were measured along the three directions: parallel and perpendicular to the pressing direction as well as along the direction having the angle of 45° with respect to the G_f plane. In this work, an average α was calculated in the temperature range 50 – 150 °C to evaluate the thermal expansion performance of the composites.

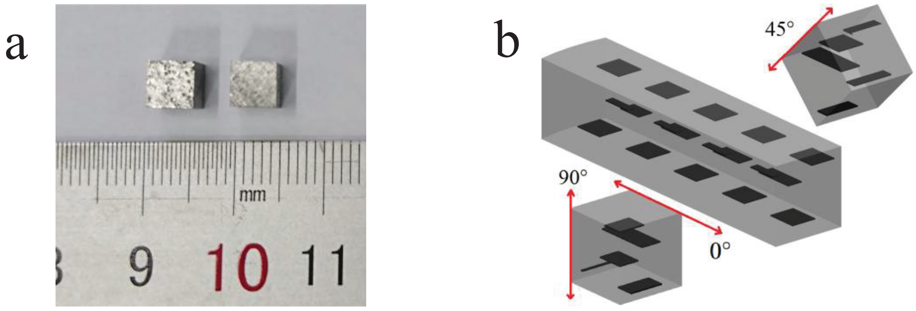

Fig. 3.3: (a) Photograph showing two specimens of the Al_F/G_f composites used for CTE measurements and (b) schematic illustration of sectioning.

Fig. 3.4 shows typical top and two side views of the Al_F/40 vol.% G_f composite with the 1D arrangement, where a model designed by SolidWorks software shows view directions. High orientation of G_f perpendicular to the pressing direction can be clearly observed from two comparable side views, which is consistent with the previous report [38].

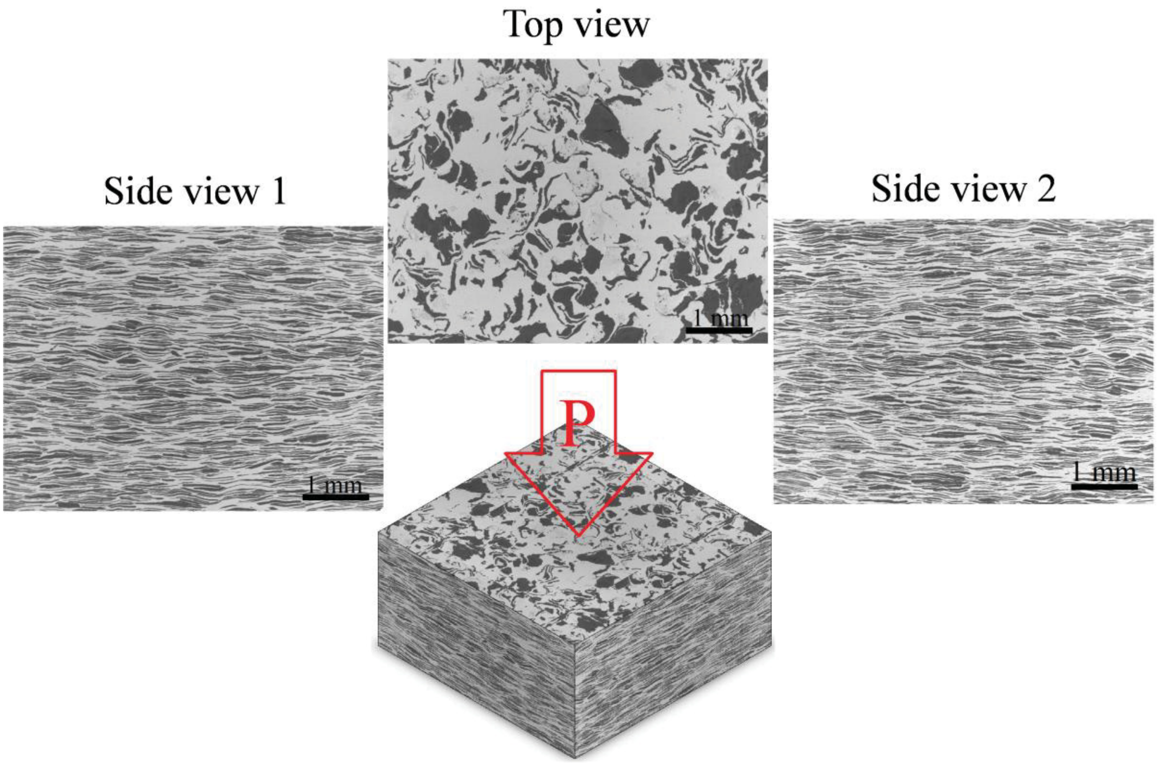

Fig. 3.4: SEM micrographs of the aligned Al_F/40 vol.% G_f composite showing one top and two side views, and a model designed by SolidWorks software.

This micrograph of side view has an area of 5.7 × 4.3 mm^2 covering two third of the sample thickness meaning that the aligned G_f spread all over the sample. Top view shows a different morphology, in which the plane of G_f can be seen. The measured relative density is around 99% indicating almost full densification after hot pressing under vacuum.

Fig. 3.5 shows the orientation distribution of G_f obtained by the image analysis of side view 1 in Fig. 3.4 (refer to chapter 2.6). The parameter $<\cos^2\theta>$ was calculated to evaluate the orientation degree of G_f in Al matrix, and its calculated value is equal to 0.94. Indeed, the same alignment level of G_f has been achieved in the Al/G_f composite using the spherical Al powder associated with step-by-step powder filling method (see Fig. 2.10 in chapter 2). However, flake powder metallurgy enables one step powder filling suggesting more effective for orienting G_f.

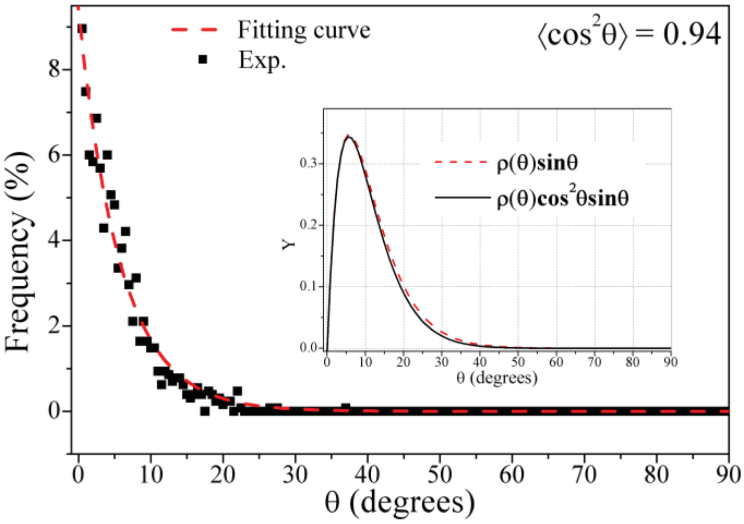

Fig. 3.5: Distribution plot of the angle θ between the graphite basal plane and the composite basal plane from side view 1 in Fig. 3.4.

3.3 Anisotropic performance of CTE in the oriented Al/G_f composites

The thermal expansion curves of the Al/40 vol.% G_f composites using the spherical and flakes Al powders are presented in Fig. 3.6a-b. Along the basal plane direction, the curves (black lines) are linear. It is clear using both powders that the curves are linear along the in-plane and nonlinear along the through-plane (i.e. pressing) directions. The nonlinear curves look like a parabola, which means the tested materials shrink first and then expand with continually increasing the temperature. The shrinking stage along the through-plane of specimen using the spherical Al powder is smaller than that using the flake Al. In other words, the symmetric axis of parabola-like curve shifts to higher temperature for the sample obtained from the flake Al powder. It should be noted that there is a visible remaining deformation (plastic effect) after each heating-cooling cycle for both composites. Besides, the curves obtained along the direction forming an angle of 45° to the basal plane also appear like a parabola, which only show the starting points of the expansion stage shift to the low temperature ranges compared to that along the through-plane direction.

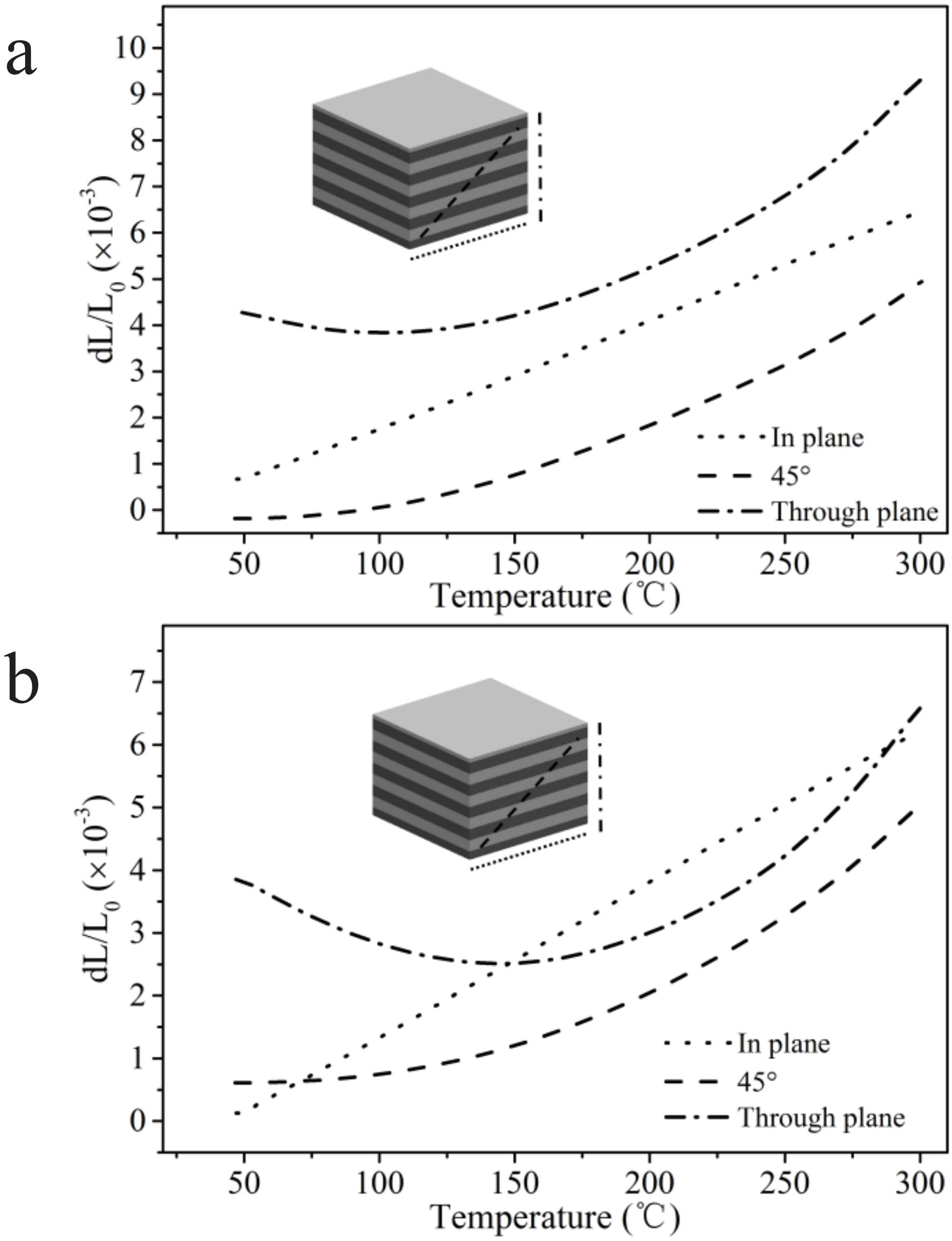

Fig. 3.6: Thermal expansion curves of the Al/40 vol.% G_f composites (a) spherical Al powder (b) flake Al powder.

Those curves can be derived from the curves parallel and perpendicular to the basal plane by means of strain transformation using the following equation [125],

$$\varepsilon_{\theta} = \varepsilon_{0^\circ}\cos^2\theta + \varepsilon_{90^\circ}\sin^2\theta \tag{3.2}$$

in which ε_θ is thermal expansion along the direction forming the angle θ with respect to the basal plane. Giving the θ of 45°, both $\cos^2\theta$ and $\sin^2\theta$ are equal to ½. Fig. 3.7 shows that the thermal expansion behaviour in the θ of 45° is the average combination of two directions parallel and perpendicular the basal plane of the composite. Furthermore, the fitting treatments using Origin software were applied to all the linear and nonlinear (parabola function) curves along the in-plane, through-plan and 45° directions. The obtained formulas are presented below:

$$\varepsilon_{0^\circ} = 24.6 \times 10^{-6}\mathrm{T} - 0.001 \tag{3.3}$$

$$\varepsilon_{90^\circ} = 1.55 \times 10^{-7}\mathrm{T}^2 - 45 \times 10^{-6}\mathrm{T} + 0.007 \tag{3.4}$$

$$\varepsilon_{45^\circ} = 0.75 \times 10^{-7}\mathrm{T}^2 - 9.5 \times 10^{-6}\mathrm{T} + 0.001 \tag{3.5}$$

$$\varepsilon'_{45^\circ} = \varepsilon_{0^\circ}\cos^2 45^\circ + \varepsilon_{90^\circ}\sin^2 45^\circ = 0.775 \times 10^{-7}\mathrm{T}^2 - 10.2 \times 10^{-6}\mathrm{T} + 0.003 \tag{3.6}$$

Their corresponding fitting curves are displayed in dash in Fig. 3.6, which agree with the experimental ones. Also, ε'_{45° calculated using equation 3.2 from the fitting equations of in-plane and through-plan directions is very approximate to the expression of 45° fitting.

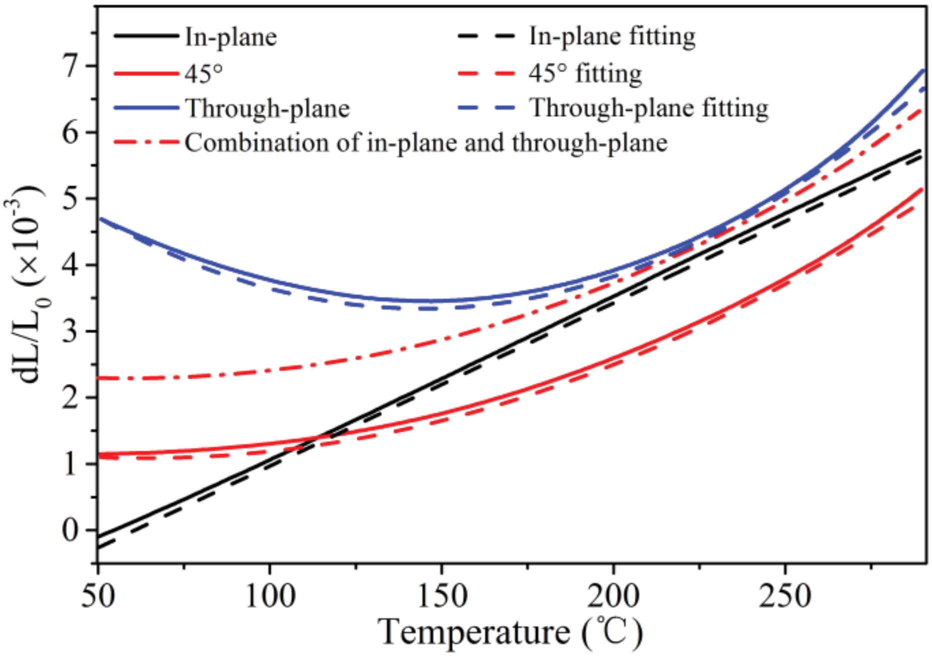

Fig. 3.7: Fitted thermal expansion curves of the Al$_F$/40 vol.% G$_f$ composites

The derivative of dilation curves processed using Origin software is regarded as dynamic CTE (D_{CTE}) as a function of temperature. For simple assessment of D_{CTE} along the different directions, the D_{CTE} curves were originated from the first cooling stage for each direction as shown in Fig. 3.8. It clearly shows a high anisotropy in thermal expansion. The CTE value is almost constant over the whole testing temperature range (40 – 300 °C) along the direction of the basal plane (black dot lines in Fig. 3.8) for both samples. Parallel to the pressing direction, CTE varies from the negative value to positive one. For the sample obtained from the spherical Al powder, it crosses the black line at around 190 °C, for the other one, it crosses at around 260 °C. As for the 45° direction, they show the similar tendency, having an average performance of the other two directions. Table 3.1 presents the average physical CTE in the temperature range of 50 – 150 °C from examined three directions of two composites. CTE along the in-plane is approximately identical for both samples using different Al powder, while the composite fabricated with the flake Al powder shows much lower value of CTE (-11 10^{-6}/K) than another one (1 10^{-6}/K) in the through-plane direction (**Table 3.1**).

Table 3.1 Average CTE values of the Al/40 vol.% Gf composites using the spherical Al and flake Al powders in the temperature range 50 – 150 °C.

	In-plane (10^{-6}/K)	**Through-plane (10^{-6}/K)**	**Calculated 45° (10^{-6}/K)**	**Measured 45° (10^{-6}/K)**
Spherical Al	22±0.1	1.5±2.2	12	10±1
Flake Al	23±0.8	-11±2	6	6.5±0.6

Additionally, measured CTE values obtained at 45° direction are 10 × 10^{-6}/K and 6.5 × 10^{-6}/K for two samples, respectively, being close to half of the sum of CTEs along the in-plane and through-plane directions calculated via strain transformation equation. Most interestingly, CTE value at 45° for sample using the flake Al powder are very close to that of alumina substrate (7 × 10^{-6}/K). Thus, it is of significance to tailor the CTE by combining the thermal expansion responds of pressing direction and its perpendicular one in order to obtain a composite showing an isotropy in thermal expansion behaviour.

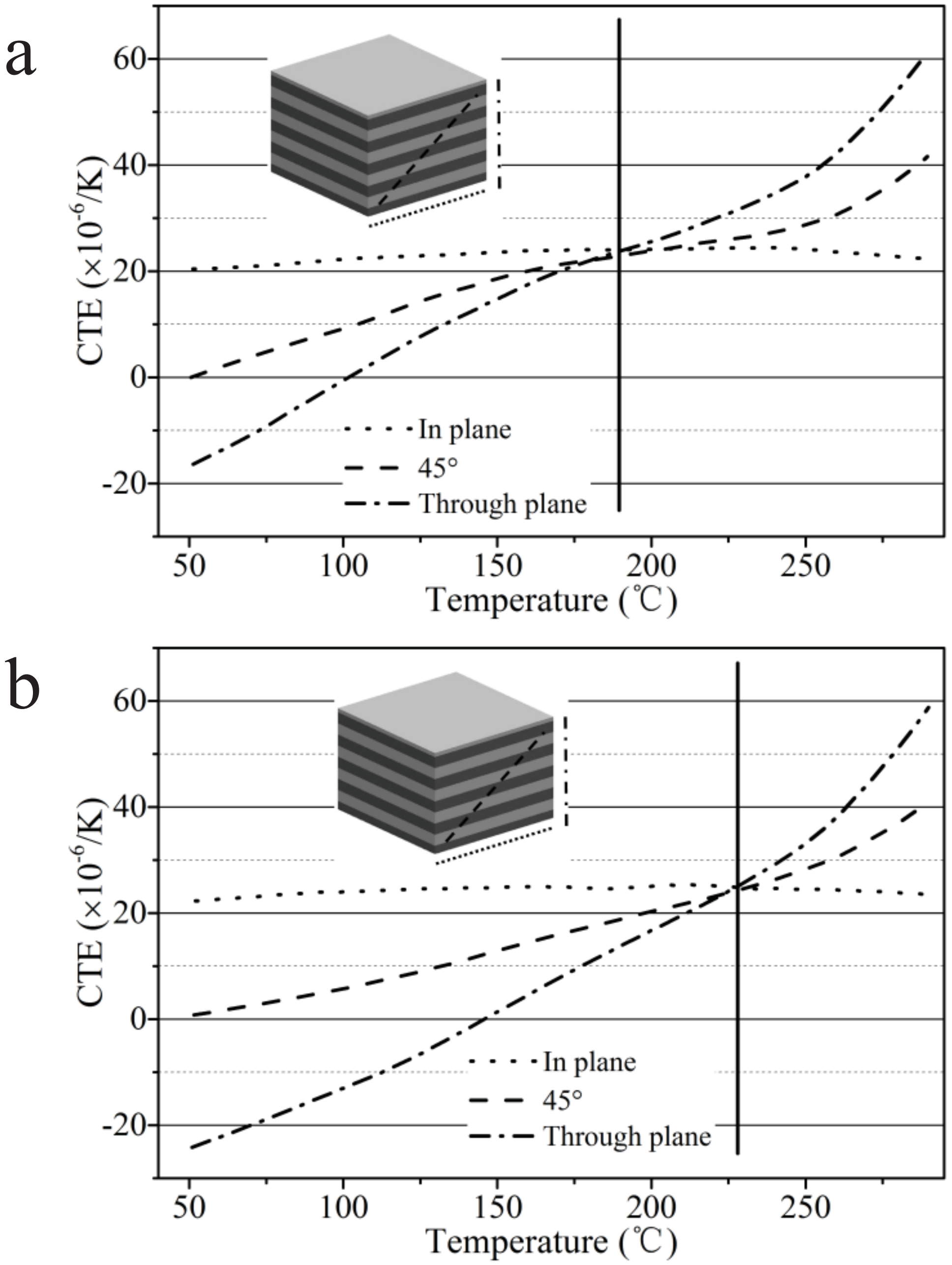

Fig. 3.8: Dynamic CTE of the Al/40 vol.% G_f composites obtained from (a) the spherical and (b) flake Al powders.

3.4 An attempt to form the 2D and 3D arrangements of G_f

3.4.1 The 2D arrangement of G_f

Convensional Al/G_f composites farbicated by either liquid [51, 103] or solid routes [28, 38] show an arrangement of G_f along the direction penpendicular to the pressing one (1D arrangement), as exhibited in the Fig. 3.9a, which exhibits a high anisotropy in both TC and CTE. Although high TC along the in-plane direction can fulfil the requirement of dissipating excess heat produced by Si chip, an anisotropy in CTE would cause the thermal stress on the surface contacting the Si chip. The thermal expansion behaviour along the 45° direction has been measured showing an average value of in-plane and through-plane directions. Thus, arraying G_f in two directions being orthogonal to each other, as shown in Fig. 3.9b, could allow the composite materials to exhibit an isotropy of CTE in a plane, whose value is equivalent to that one along the direction at 45° in the Al/G_f composites with 1D arrangement.

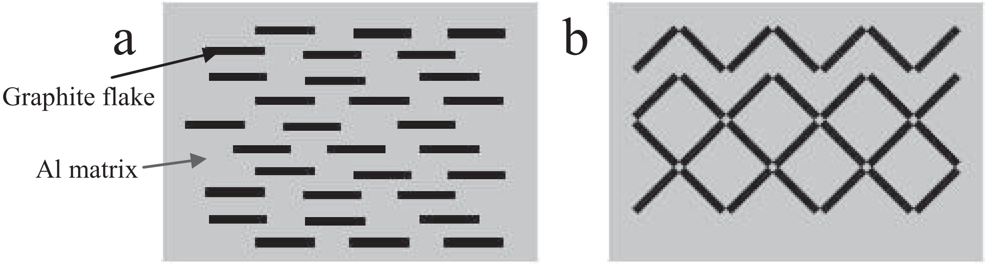

Fig. 3.9: Schematic illustrations of Al/G_f composites with the different arrangements of G_f: (a) 1D, (2) 2D.

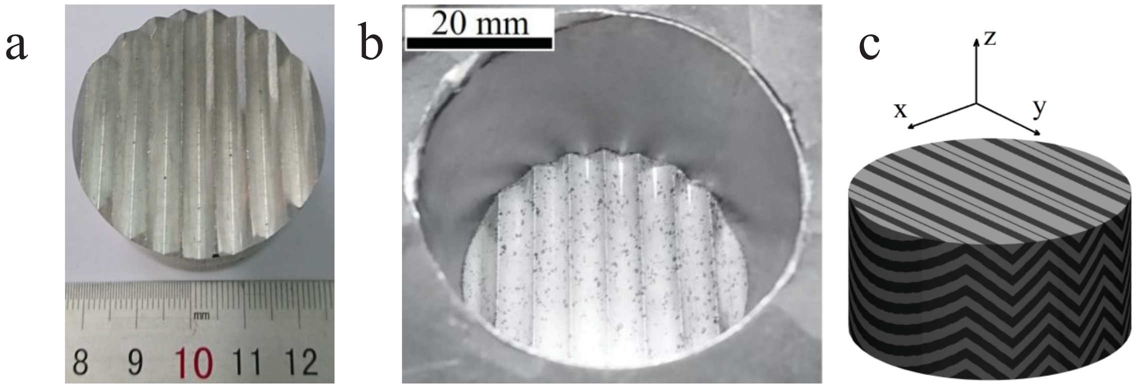

Fig. 3.10: Photographs of (a) the punch with groove used for forming the 2D arrangement of G_f, (b) morphology of the powder layer after applying such a punch, and (c) schematic illustration of the final composite (in black the G_f and gray the Al).

The 1D arrangement of G_f has been achieved in the Al/G_f composites either using spherical or flake Al powder. Nevertheless, it is necessary to apply a step-by-step powder filling method to get the high orientation of G_f using the spherical Al powder, as mentioned in section 3.4, while an identical arrangement of G_f can be obtaied using the flake Al powder merely applying the one-step powder filling process. During the step-by-step powder filling process, a cylinder punch is able to form a flat layer with the thickness of around 1 mm by controling the quantity of powder filled each time, in which the alignment of G_f is confined in the plane. To achieve the arrangement of G_f along two planes being not parallel to each other, a punch with zigzag groove was designed as shown in Fig. 3.10a. Compared to the spherical Al powder, the flake powder has the relatively lower apparent density to result in higher green strength after cold pressing. Therefore, flake Al powder mixed with G_f was selected to form the 2D arrangement of G_f. We designed and manufactured two punches with groove having the angles of groove of 90° and 60°, and the distance between each two grooves being the same of 5 mm. The precursor of Al_F + 40 vol.% G_f mixture was made via the step-by-step powder filling method using such new-designed punches. The top surface morphology of powder layer after one step cold pressing is shown in Fig. 3.10b, in which the arrangement of G_f models the contour of punch. For the final step, the conventional punch was used to form a flat morphology on the top. Then, hot pressing was carried out using the same parameters to get the final product as mentioned in section 3.2. An expected 2D arrangement of G_f is illustrated in Fig. 3.10c.

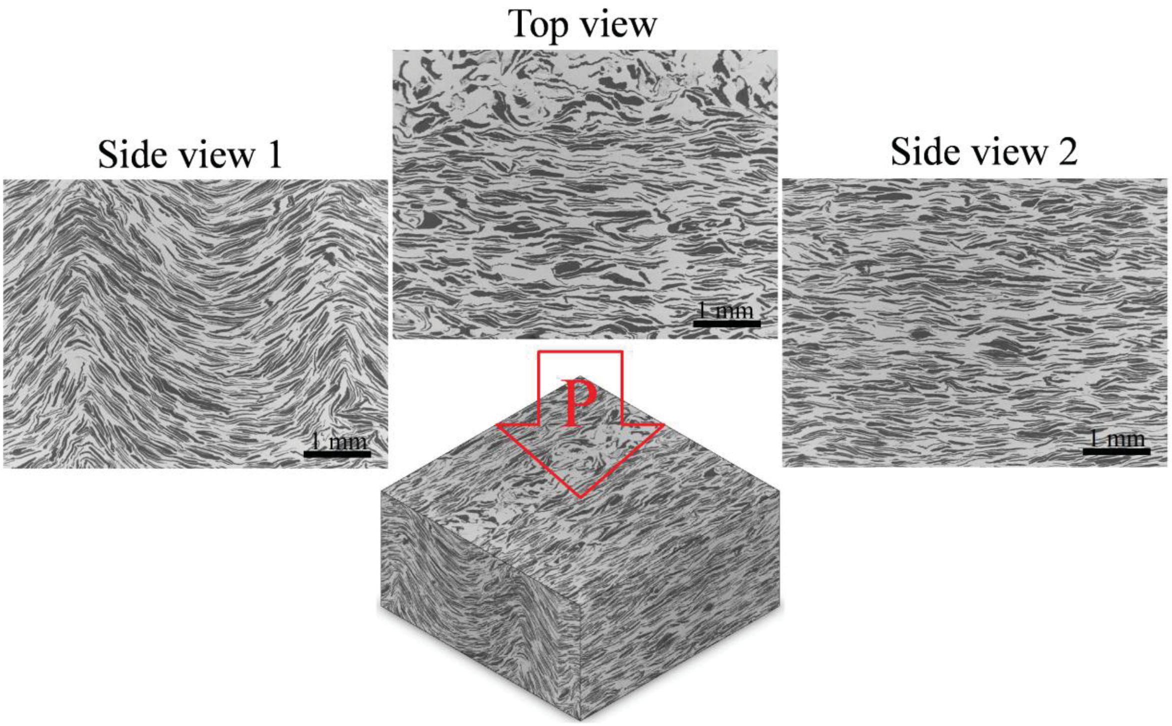

Fig. 3.11: SEM micrographs of Al_F/40 vol.% G_f composite with 2D arrangement showing the one top and two side views and a model shows view directions.

Fig. 3.11 shows the top and two side views of the Al_F/40 vol.% G_f composite fabricated using punches with groove angle of 90°. A nearly wave-like array of G_f can be observed in one side view owing to the application of the punch with zigzag groove, and the high alignment of G_f appears in top and other side view. Further, Fig. 3.12 displays G_f orientation angle distribution profiles as well as fitting curves of the Al_F/40 vol.% G_f composites prepared by punches with different groove angle (90° and 60°). Gaussian function was used to do fitting for the 2D arrangement with following equation.

$$\rho(\theta) = Ae^{\left(-\frac{(\theta - C)^2}{W^2}\right)} + y_1 \tag{3.7}$$

where A, C, W, and y_1 are the fitting parameters. $\rho(\theta)\cos^2\theta\sin\theta$ and $\rho(\theta)\sin\theta$ were substituted with the obtained fitting parameters, and the obtained curves are shown in the insets of Fig. 3.12 b and c. The orientation degree index $<\cos^2\theta>$ is the ratio of $\int\rho(\theta)\cos^2\theta\sin\theta$ and $\int\rho(\theta)\sin\theta$. The integral calculation is accomplished by calculating the area of the region bounded by the fitting curve and θ-axis using Origin software. The $<\cos^2\theta>$ values for samples fabricated using punches with 90° and 60° groove were 0.87 and 0.67, respectively, which reveals that the arrangement of G_f can be controlled more or less by the new-designed punches. Furthermore, the statistical average angle of G_f obtained via image analysis is 14° for sample using punch with 90° groove, which is smaller than that of 26° using punch with 60° groove. Although the designed average angles of G_f are expected to be 45° or 30° according to the morphology of powder layer during cold press, the micrograph observations show that those features changed after hot pressing. This can be attributed to the reoccurrence of alignment of G_f during uniaxial hot pressing.

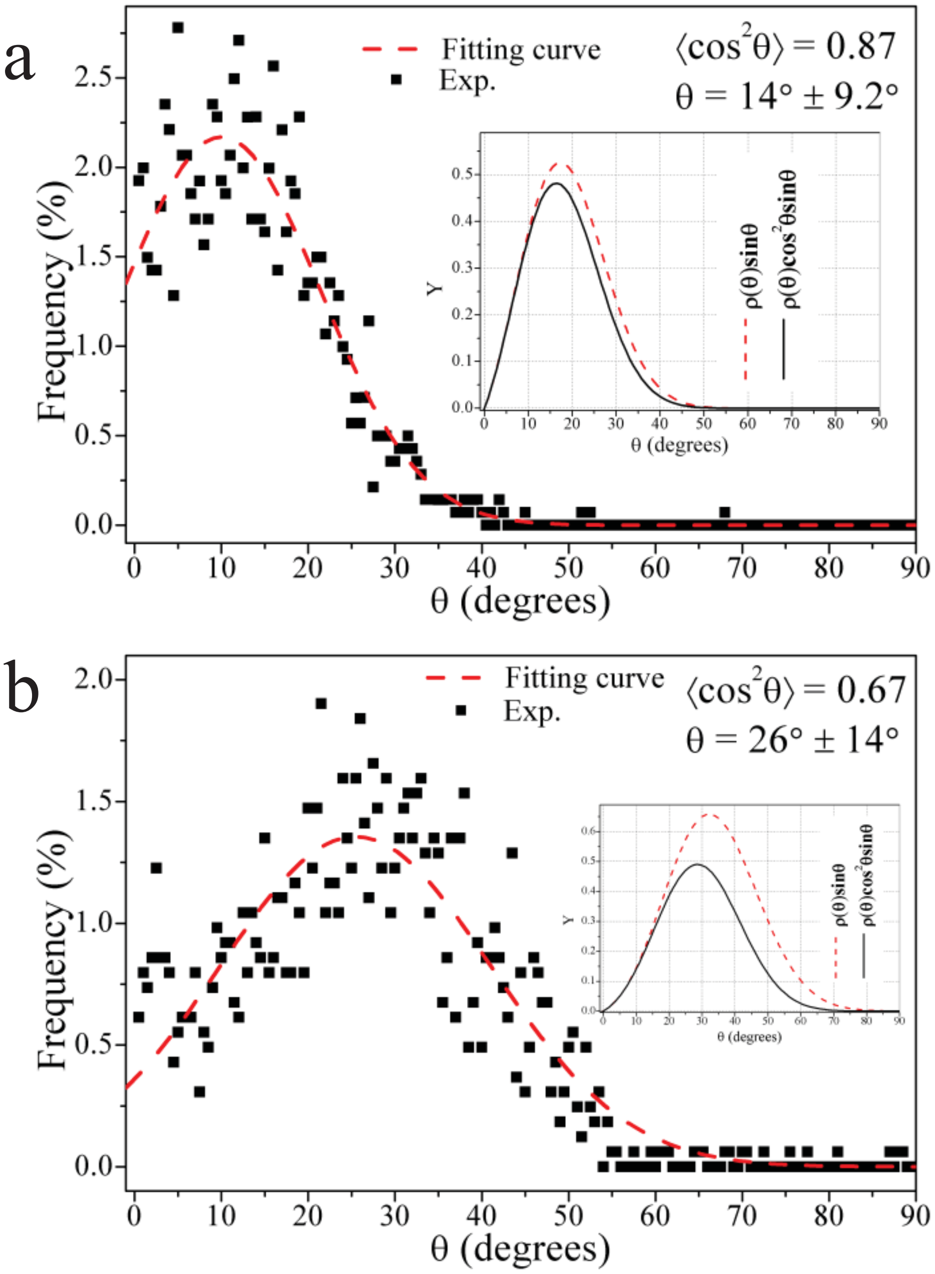

Fig. 3.12: Orientation distributions of G_f in the Al_F/40 vol.% G_f composites using the punches with groove: (a) punch with groove having angle of 90°, (b) punch with groove having angle of 60°.

To investigate the effect of 2D arrangement of G_f on CTE, the dilation behaviours of sample fabricated using the punch with 60° along the in-plane and through-plane directions was characterized and converted into dynamic CTE curves. As shown in Fig. 3.13, the distance between dynamic CTE curves along x (red solid line) and y (blue solid line) axis in 2D arrangement are a little bit smaller than of that the in-plane (black dot line) and through-plane (black dash dot line) directions in the 1D arrangement. Those results indicate that the anisotropic degree in CTE was changed to some extent by applying the 2D arrangement. However, it is still far away from the thermal expansion behaviour at 45° direction in the 1D arrangement, mainly because the average angle of G_f is smaller than 45° from the micrograph observations. Therefore, it is necessary to redesign the punch or to change the process to obtain the ideal 2D arrangement of G_f.

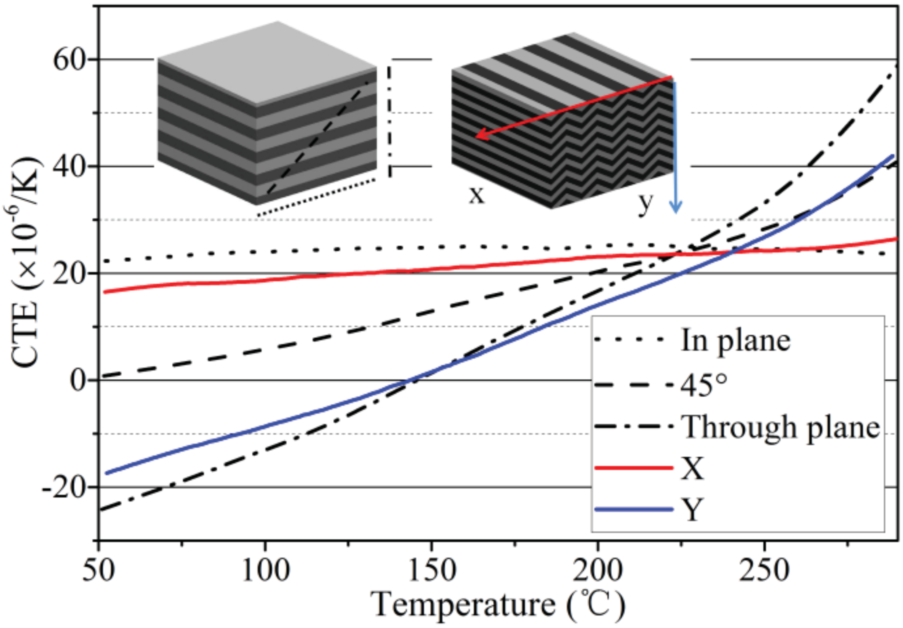

Fig. 3.13: Comparison of dynamic CTE between the Al_F/40 vol.% G_f composites manufactured using plane punch and punch with groove having the angle of 60°.

3.4.2 The 3D arrangement of G_f

As discussed previously, the high TC appears in the direction perpendicular to the pressing direction in the oriented metal/G_f composites due to the 1D arrangement of G_f. Thus, considering the heat sink applications, semiconductor device is naturally mounted on the face perpendicular to the direction beneficial from the high TC [36, 44], as demonstrated in Fig. 3.14a. However, the thickness of sample fabricated by hot pressing is generally limited to 10 mm or lower for the sake of the good densification. In this case, the thickness side of composites cannot cover the whole surface of Si chip, such as CPU or GPU (e.g. 150 mm^2 for AMD RYZEN 4000), so as not to exert effectively heat dissipation. The large surface usually appears on the top and bottom of the composite depending on the diameter of die, but the Si chip will suffer the low TC along the direction perpendicular to itself, as shown in Fig. 3.12b. So, we proposed the 3D arrangement of G_f in order to increase the TC along the pressing direction (z) as well as to keep an isotropy of CTE in x,y plane (Fig. 3.14b).

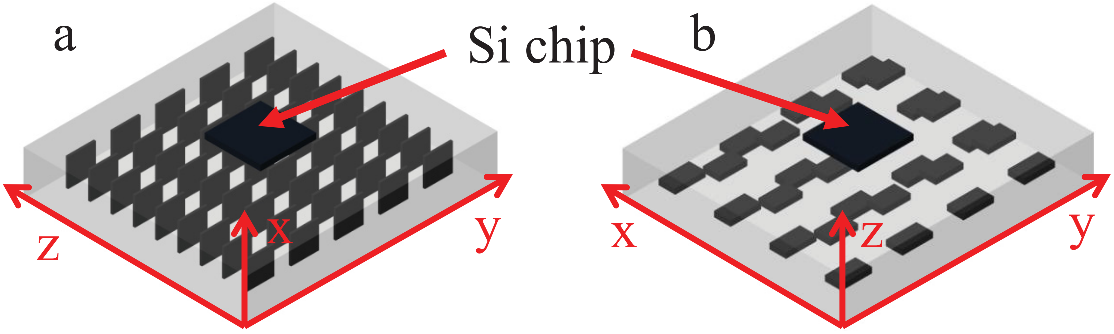

Fig. 3.14: Schematic illustrations of two typical configurations between the oriented (1D) metal/G_f composite and Si chip, (a) Si chip attaches on the face perpendicular to the in-plane direction of G_f, (b) Si chip attaches on the face parallel to the in-plane direction of G_f.

final composite.

Fig. 3.15a displays the photograph of the punch designed for the 3D arrangement. The angle between each intersecting face is 90°, so it can form a 3D isotropic arrangement of G_f in term of geometry. The same step-by-step powder filling method was used to make an Al + G_f precursor with the 3D arrangement. The top surface morphology of the powder layer after applying new-designed punch is shown in Fig. 3.15b. The arrangement of G_f in the final composite after hot pressing is illustrated in Fig. 3.15c. Fig. 3.16 shows the typical top and two side views of the Al_F/40 vol.% G_f composites fabricated using the 3D punch. The arrangement of G_f from the top view looks like an array of concentric squares, which can be predicted by the 3D model (Fig. 3.15c). The other two side views display a roughly wave-like distribution of G_f similar to that in the 2D arrangement. However, the decrease of the average angle between graphite and composite basal plane occurred after hot pressing in the 3D arrangement. This process can be illustrated in Fig. 3.17. In practice, especially in center region of the composite, the angle of G_f with respect to the basal plane close to 0°.

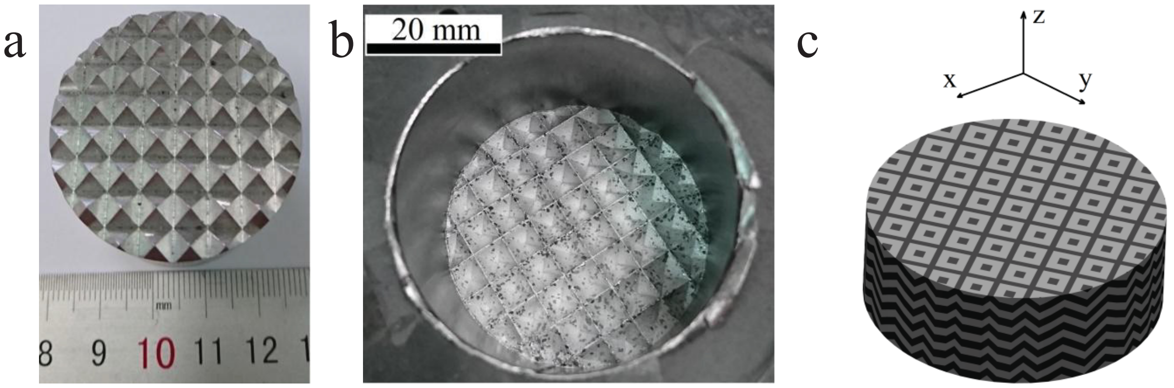

Fig. 3.15: Photographs of (a) the punch used to form the 3D arrangement of G_f and (b) morphology of powder layer after applying such a punch, and (c) schematic illustration of the final composite.

Undoubtedly, the structure built during cold pressing using either the 2D or 3D punches was not well conserved after hot pressing. Generally, the relative density of precursor compacted by uniaxial cold pressing is 70 – 85% [45], while this value can reach approximately 99% after hot pressing. There is about 25% of thickness reduction when applying uniaxial pressure during hot pressing, so the rearrangement of G_f is unavoidable. Therefore, in order to get a final product with an average angle of 45°, the angle of the groove should be at least smaller than 60°. Indeed, one more punch with groove having 50° was machined, and the same powder filling stage was repeated. However, this trial exposed a serious problem that most of powder will stick at the corner of groove when separating the punch from the die after cold pressing. Thus, it destroyed the structure being built by the punch and made the process unable to continue.

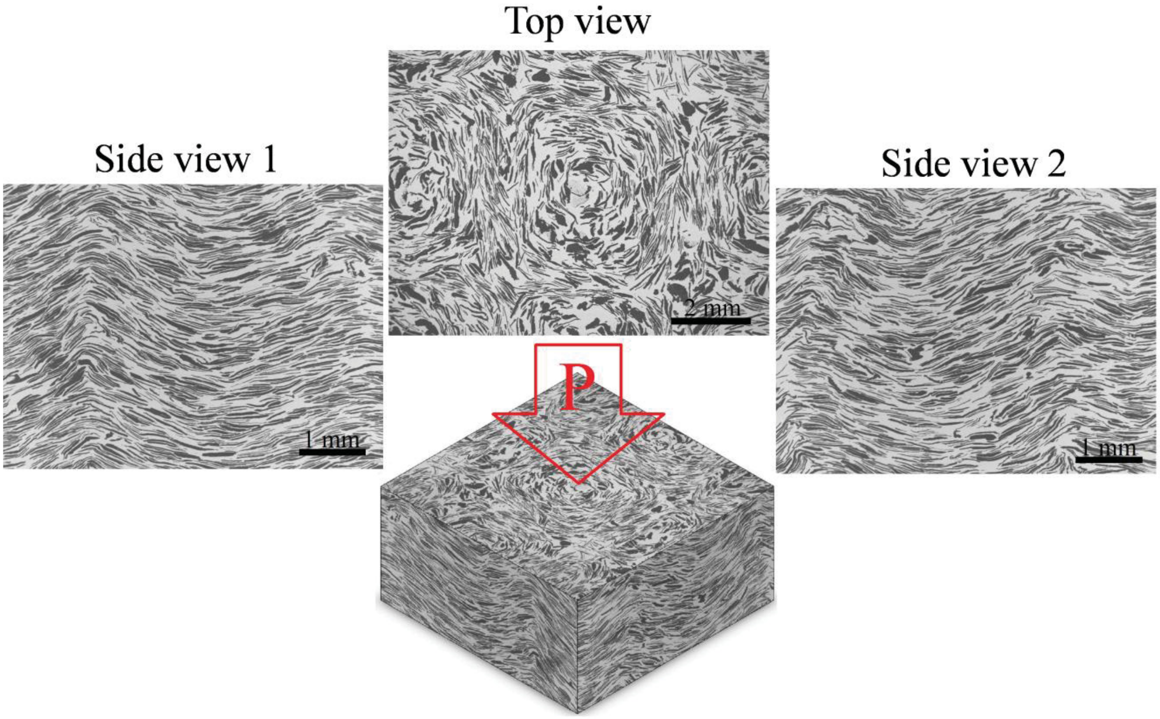

Fig. 3.16: SEM micrographs of the Al_F/40 vol.% G_f composites with 3D arrangement of G_f show one top and tow side views and a model shows view directions.

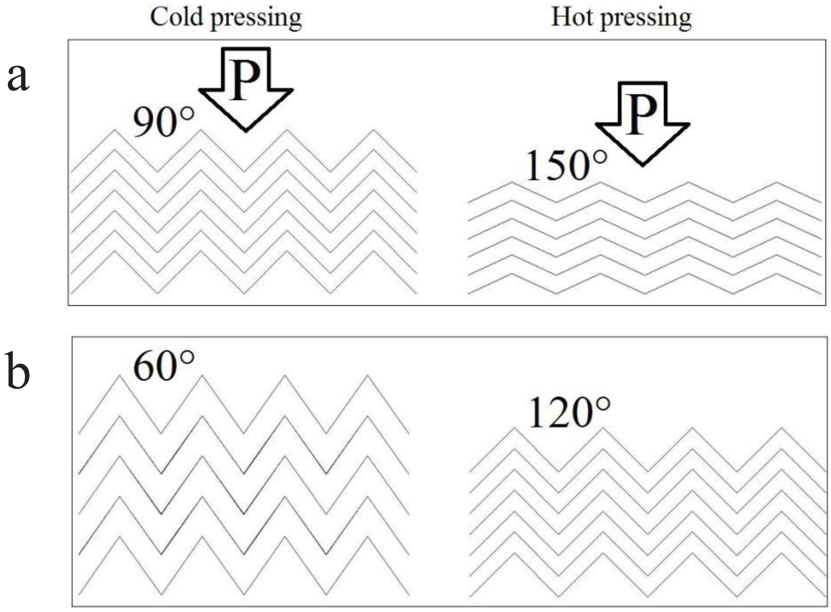

Fig. 3.17: Schematic illustrations of the arrangement of G_f during cold pressing and after hot pressing using: (a) the punch with 90° groove and (b) the punch with 60° groove.

3.5 Second attempt to form 2D and 3D arrangements of G_f

3.5.1 Change of the process to achieve controlled 2D and 3D arrangements

To solve the problem described in last section, a new approach was proposed in this section. As illustrated in Fig. 3.18, G_f are still being arrayed via a punch with zigzag-like contour during cold pressing, while, in this time, the compression direction during hot pressing is perpendicular to that during cold pressing. G_f can be arrayed in an angle large than 45°, so that it is likely to be altered to 45° after hot pressing. Besides, there is no concern about the separating issue of the punch and powder after cold pressing.

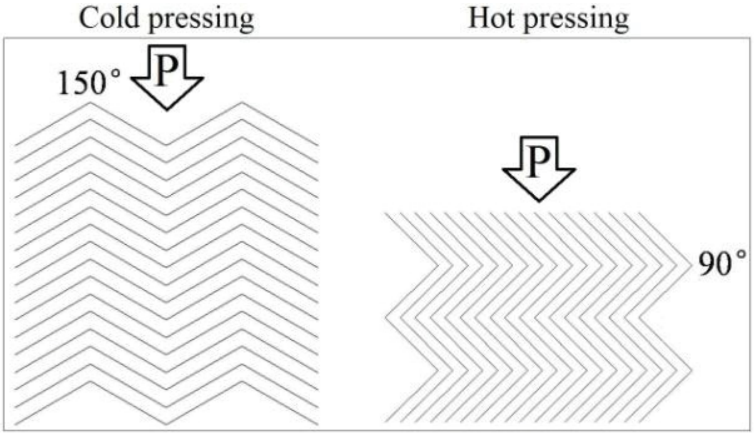

Fig. 3.18: Schematic illustration of the 2D arrangement of G_f via changing the pressing direction by 90°.

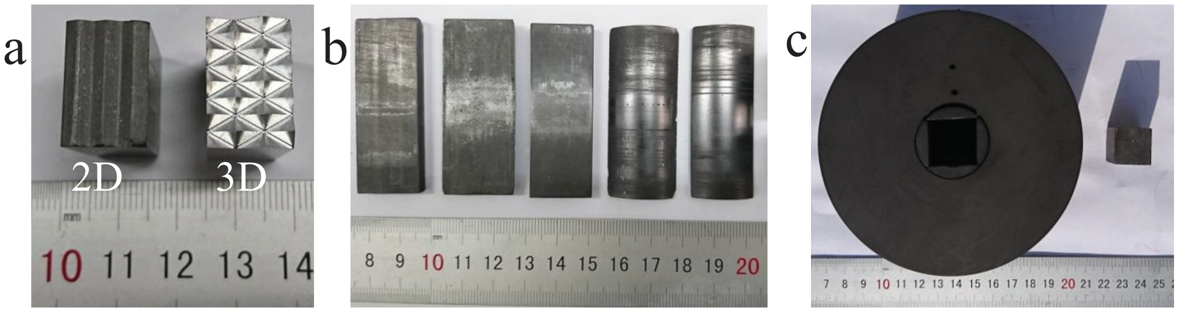

Fig. 3.19: Photographs of the mould components: (a) 2D and 3D punches, (b) graphite parts assembled to form a rectangle cavity, and (c) graphite die and punch used for fabricating a sample having the rectangle shape.

Since the pressure direction is different between cold and hot pressing, those two processes have to be carried out in the different dies, which means the sample needs to be transported from one mold to another one. Meanwhile, graphite die is required to be designed with rectangle cavity having a square cross-section. Hence, its corresponding punches with the 2D and 3D features were redesigned as shown in Fig. 3.19a. However, graphite die with square cavity is likely to cause stress concentration at the corner, making the graphite die easily to be broken when applying a high uniaxial pressure. Beyond that, the sample formed during cold pressing should be easily separated from the mold without being damaged. Finally, several graphite components, as displayed in Fig. 3.19b, were machined to assemble with a conventional graphite die to create a rectangle or square cavity through different assembled styles (Fig. 3.19c), which can be used in either cold pressing or hot-pressing stages.

It should be noted that, as schematically illustrated in Fig. 3.20, pressing can be divided into two types: single and double action pressing [126]. In a conventional hot pressing process, the pressing operation is completed by moving upper punch into the die, while the underside of lower punch is at the same level of that of die so that those two parts are both stationary. This pressing may lead to a different arrangement of G_f between the top and bottom. In double action pressing, upper and lower punches move simultaneously from above and below into the die. A homogenous arrangement of G_f on the top and bottom of sample can be ensured more or less.

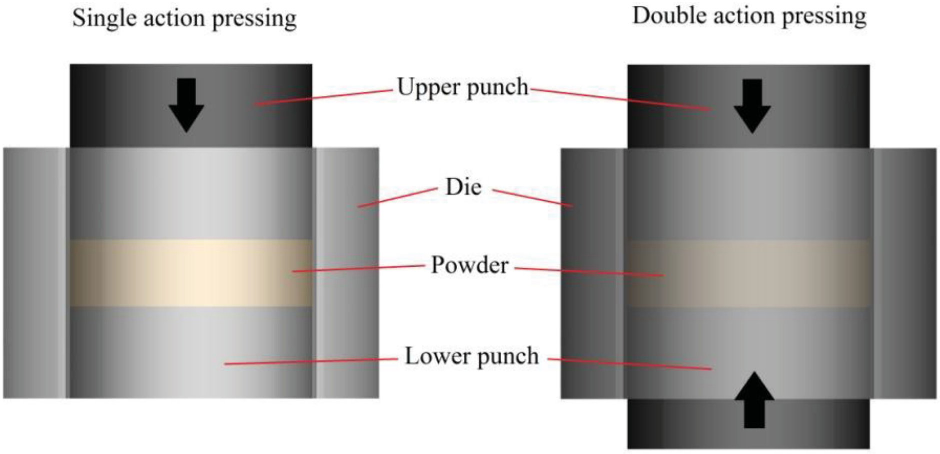

Fig. 3.20: Schematic illustrations of the single and double action pressing.

The procedure to form the 2D and 3D arrangements of G_f using the new die is illustrated in Fig. 3.21. Firstly, a precursor was formed via step-by-step powder filling manner using the specifically designed punch (Fig. 3.21a) either in 2D or 3D contours. Considering the rearrangement of G_f in hot pressing, the angle was designed larger than the final one. The top surface morphology of powder layer after one step cold pressing is displayed in Fig. 3.21b.

Then, the precursor was completely removed out of the mould and was turned 90° (Fig. 3.21c). It was then put in another reassembled mould with square cavity (20 × 20 mm^2, Fig. 3.21d) for hot sintering. It should be emphasized that double action pressing was applied in the hot pressing. In details, one lower punch with the downside parallel to the downside of the die was first applied to fix the position of the precursor in the die. Then, the lower punch was removed from the die, and another punch with height higher than the previous one was put into the die. Thus, the lower punch has the possibility to make displacement during hot pressing. The final specimen was made into a cubic-like shape (20 × 20 × 8 mm^3, Fig. 3.21e).

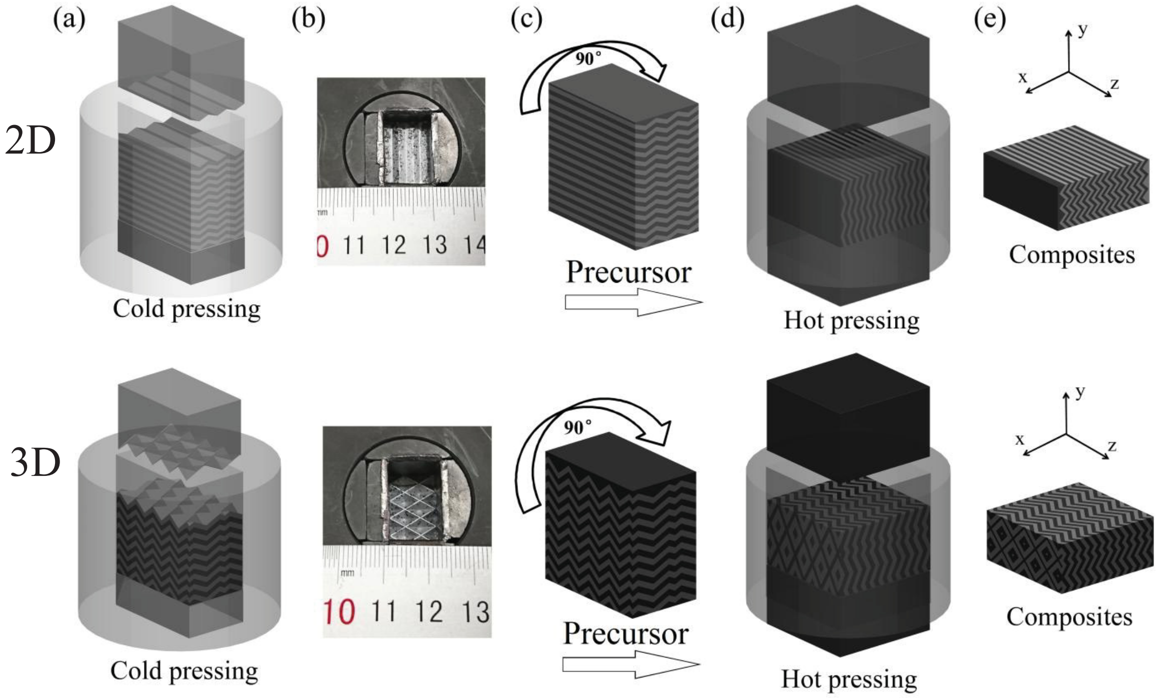

Fig. 3.21: Schematic illustrations of the fabrication processes to acquire the Al/G_f composites with the 2D and 3D arrangements: (a) cold pressing using specifically designed punches, (b) Photographs of the powder layer morphology after cold pressing, (c) the Al/G_f precursor, (d) graphite moulds used for hot pressing, (e) final products.

3.5.2 Thermal properties in the 2D arrangement

Fig. 3.22 shows one side view of the Al_F/G_f composite with 2D arrangements fabricated by new method and its corresponding orientation distribution of G_f. Applying the newly designed punch (the angle of groove is 130° and width between the groove is 4 mm) and new process achieved a nearly perfect zigzag-like distribution of G_f. In the local area between two red dash lines as indicated in Fig. 3.22a, G_fs still form a high orientation along the direction having an angle of nearly 45°. The orientation distribution is presented in the Fig. 3.22b, in which the average angle of G_f with respect to composite basal plane is around 44.6°. The $<\cos^2\theta>$ was calculated to be 0.46, which gives an approximately isotropy distribution of G_f in the 2D arrangement plane. Consequently, it proves that the arrangement of G_f can be tailored by the combination of flake powder metallurgy using the specifically designed punch and the step-by-step powder filling method.

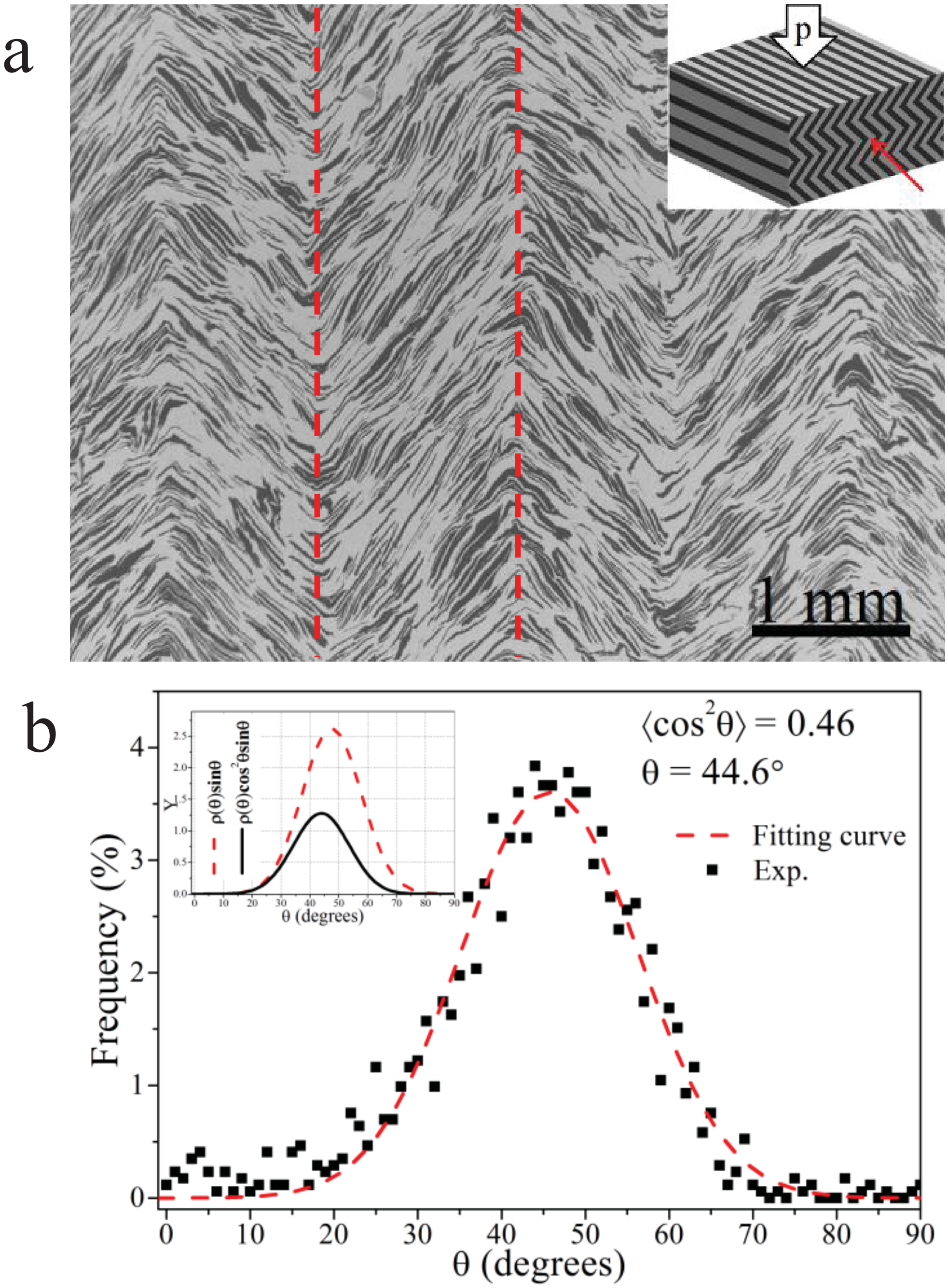

Fig. 3.22: SEM micrograph of the Al_F/40 vol.% G_f composites with the 2D arrangement of G_f using the punch with obtuse of 130° and its corresponding G_f orientation distributions

Dilatometry curves examined from the Al$_F$/40 vol.% G$_f$ composites with 2D arrangement is shown in Fig. 3.23a. Along the z axis, it shows linear expansion behaviour being similar to the in-plane direction of 1D arrangement. In other two directions, the curves are very close to parabola. Some deformation still occurred within the x axis after each thermal cycle. The impact of 2D array on CTE can be validated further through the comparison of dynamic CTE curves between 1D and 2D arrangement, as shown in Fig. 3.23b.

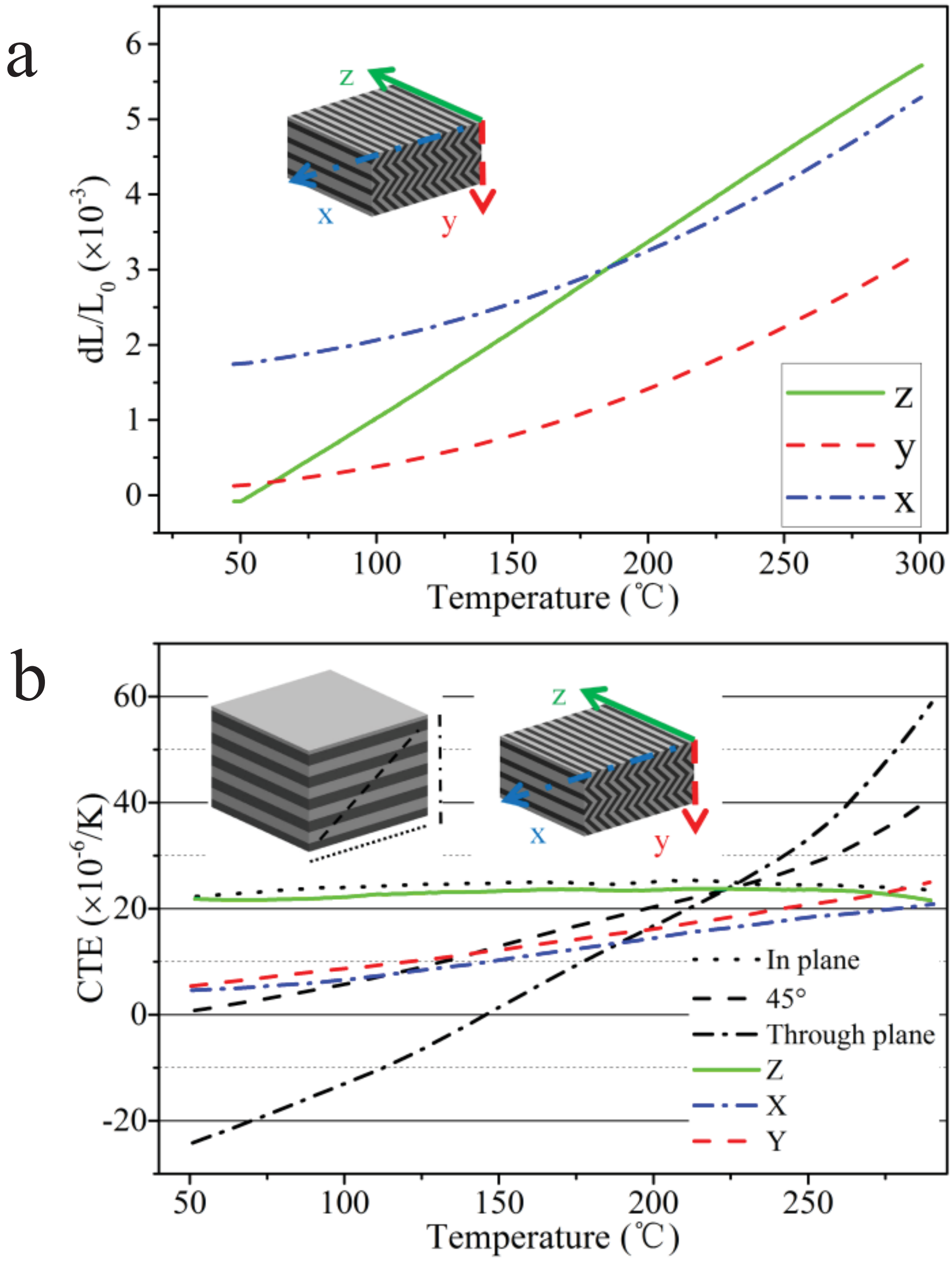

Fig. 3.23: (a) Thermal expansion curves of the Al$_F$/40 vol.% G$_f$ composites with the 2D arrangement of G$_f$ and (b) comparison of dynamic CTE vs. temperature between the 1D and 2D arrangements

The position of curves from the x and y axis in 2D array is almost located in the middle of two curves from in-plane and through-plane in 1D arrangement, meanwhile they are also very approaching to the one measured at 45° direction in 1D arrangement. The average measured TC and CTE values of the composites were given in Table 3.2. High anisotropies in the TC and CTE are clear in the sample with the conventional 1D arrangement. Applying the 2D arrangement, as a new architecture, maintained the TC (437 W/m.K) along the z direction (perpendicular to the 2D arrangement plane) as high as that (431 W/m.K) in the 1D arrangement. Further, the anisotropy degree of CTE in the 2D arrangement plane becomes small where both CTEs are as low as around 7 – 8 × 10^{-6}/K. Even though the average angle of G_f was very close to 45° regarding as an isotropy in geometry, the material still shows small anisotropy in CTE between x and y directions.

Table 3.2 Comparison of thermal properties of the Al/G_f composites between the 1D and 2D arrangements (average CTE values measured over the temperature range of 50 – 150 °C).

	1D		**2D (130° groove)**		
TC (W m^{-1} K^{-1})	z,x: 431±6	y: 40±1	x: 81±1	y: 191±1	z: 437±3
CTE (10^{-6}/K)	z,x: 23; 45°: 6	y: -11	x: 7	y: 8	z: 22

In order to examine the effect of the groove angle on the CTE, another sample was prepared using a punch having 120° groove. As Fig. 3.24 presents, the micrograph still show zigzag-like distribution of G_f, and image analysis result reveals that the average angle of G_f is around 51°. In the Fig. 3.25, the dilatometry curves measured in x and y directions have the similar profile, while the obtained dynamic CTE curves in those two directions are almost overlapped in the temperature range from 50 to 200 °C.

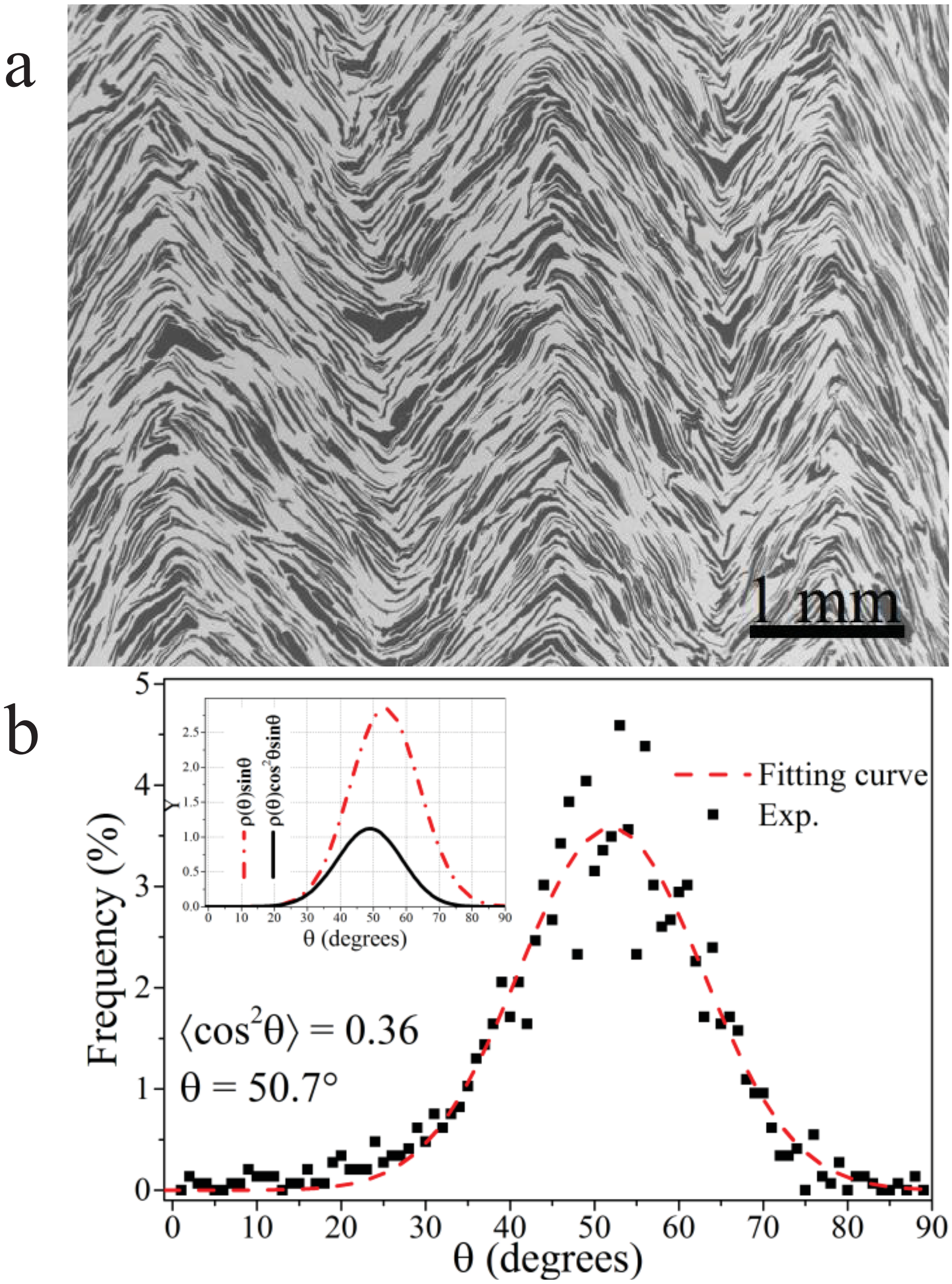

Fig. 3.24: SEM micrograph of the Al_F/40 vol.% G_f composites with the 2D arrangement of G_f using the punch with 120° groove and its corresponding G_f orientation distributions.

Moreover, the measured average CTE values given in **table 3.3** exhibits a smaller difference compared to the previous one. Above all, the CTE in the 2D arrangement plane are reduced to around 7 × 10^{-6}/K, considered as compatible with that of Si chips in the microelectronic industry. The results indicate an isotropy in geometric array of G_f may not give rise to an isotropy in properties. It also demonstrates our fabrication method is flexible enough to obtain the various 2D arrangements of G_f via changing the shape of punch.

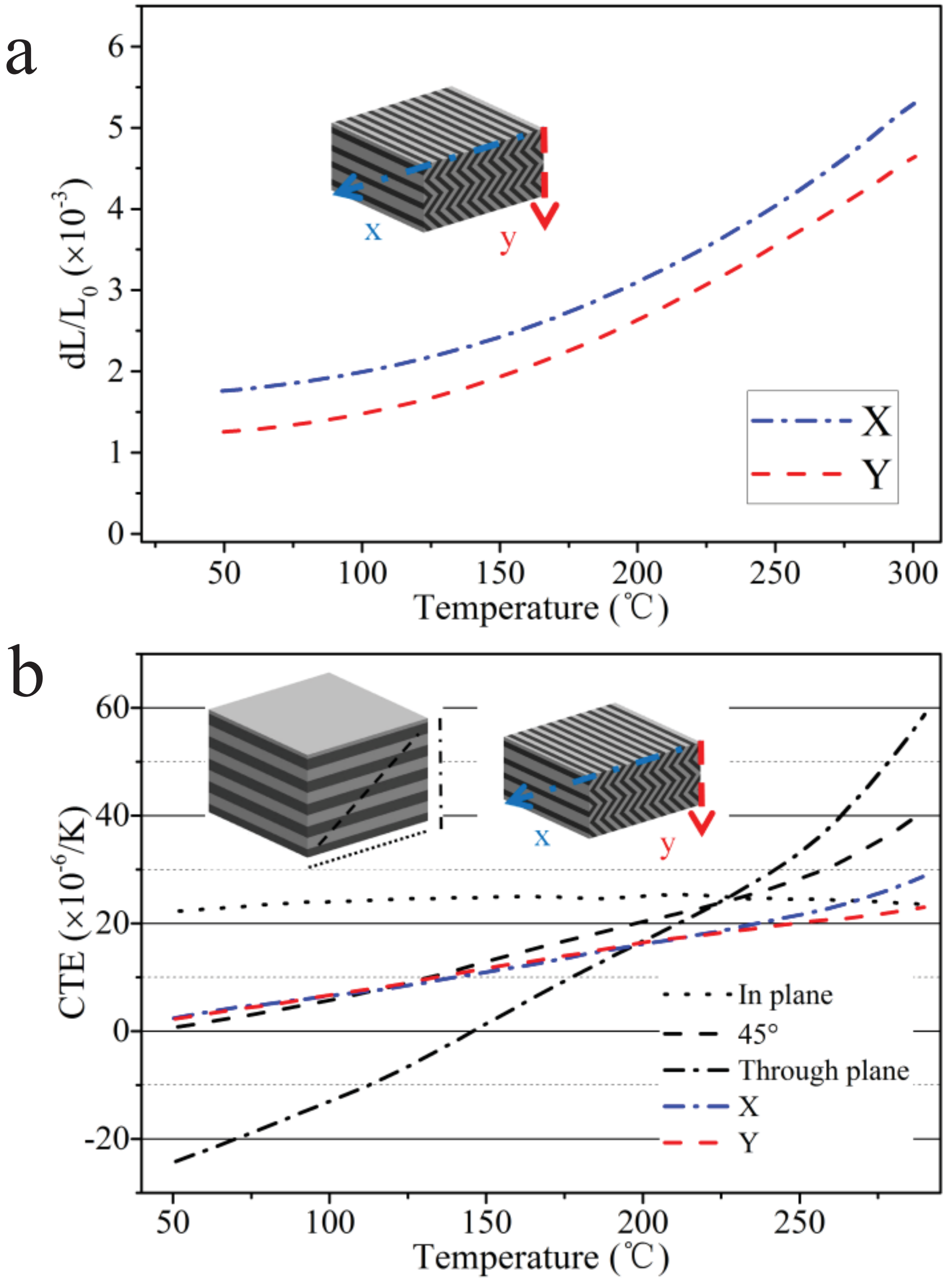

Fig. 3.25: (a) Dilation curves of the Al_F/40 vol.% G_f composites with the 2D arrangement of G_f prepared using the punch with 120° groove, (b) comparison of dynamic CTE vs. temperature between the 1D and 2D arrangements.

Table 3.3 CTE of the Al/G_f composites prepared using the punch with 120° groove (average CTE values measured over the temperature range 50 – 150 °C)

2D	**CTE (10^{-6}/K)**		
120°	x:6.5	y: 7.0	z: 22

3.5.3 New 3D arrangement

The 2D arrangement of G_f can be tailored by the angle of groove on the punch, while the 3D arrangement has to be controlled by at least three angles (α, β, and γ) as indicated in Fig. 3.26a, which determine the final arrangement of G_f in three dimensions. Four punches with different geometric features were designed and machined, donating as 30-30, 30-20, 20-20, and 17-17 as illustrated in Fig. 3.26a-d. For example, the first number of 30-30 is half of the angle α, and the second is the half of (180° - β). Fig. 3.27 show the typical top and two sides view of the Al_F/40 vol.% G_f composites fabricated using the punch 30-30. The side views present the rhombus-like and wave-like arrangements of G_f, while top view shows a less remarkable wave-like distribution. Nevertheless, compared to the Fig. 3.16, the zigzag-like distribution of G_f is more pronounced applying this new method.

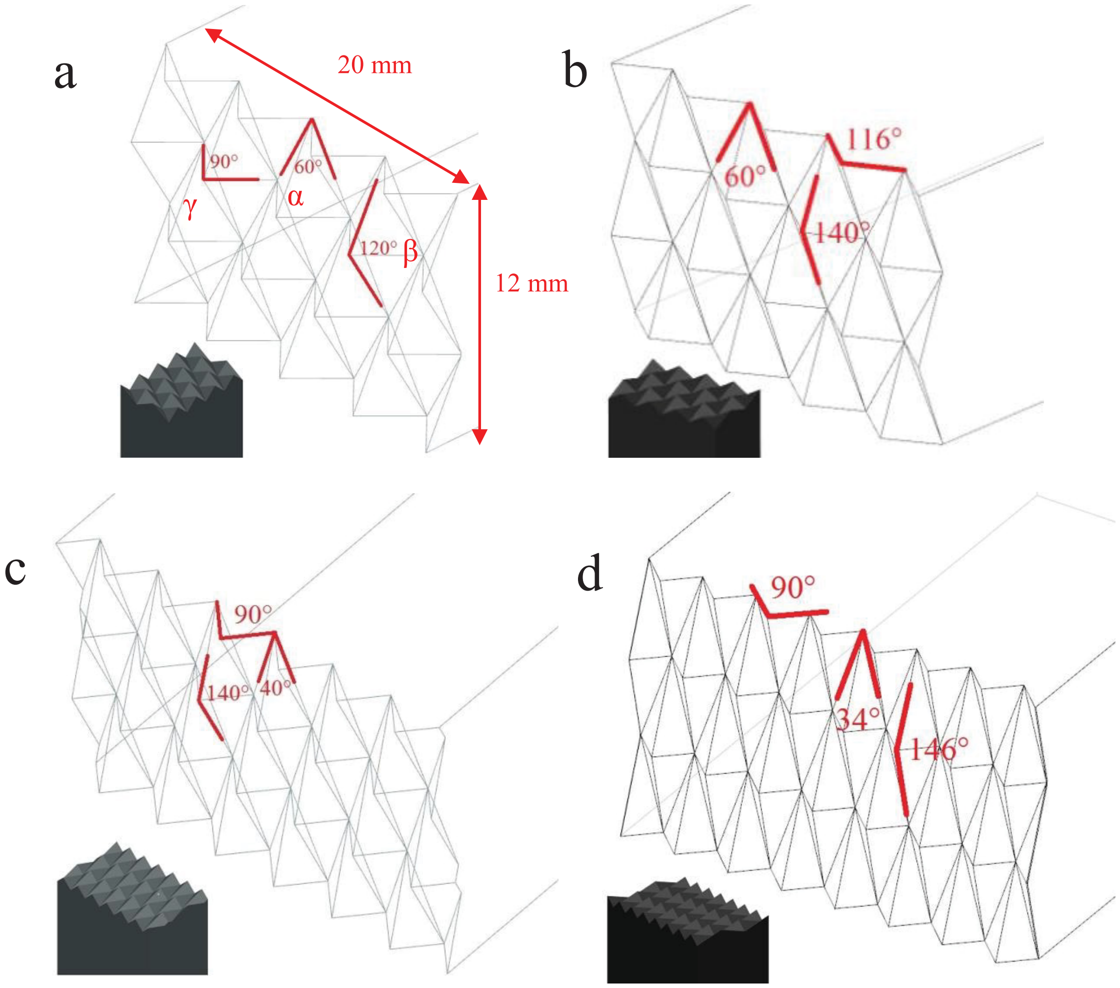

Fig. 3.26: The geometric features of the punches used for achieving the 3D arrangement: (a) 30-30, (b) 30-20, (c) 20-20, (d) 17-17.

As discussed in section 3.4.2, the arrangement feature of G_f in x-z plane was conserved after hot pressing. It suggested that there was no or negligible effect of uniaxial pressure on the orientation of G_f in the x,z plane, because this plane is perpendicular to the pressing direction. However, Fig. 3.27c shows a big change in orientation of G_f occurred after sintering compared to the model at the top right corner of the image. In addition, the angle of graphite with respect to the x-z plane formed in cold pressing changed apparently after hot pressing, which is consistent with the results in 2D arrangements.

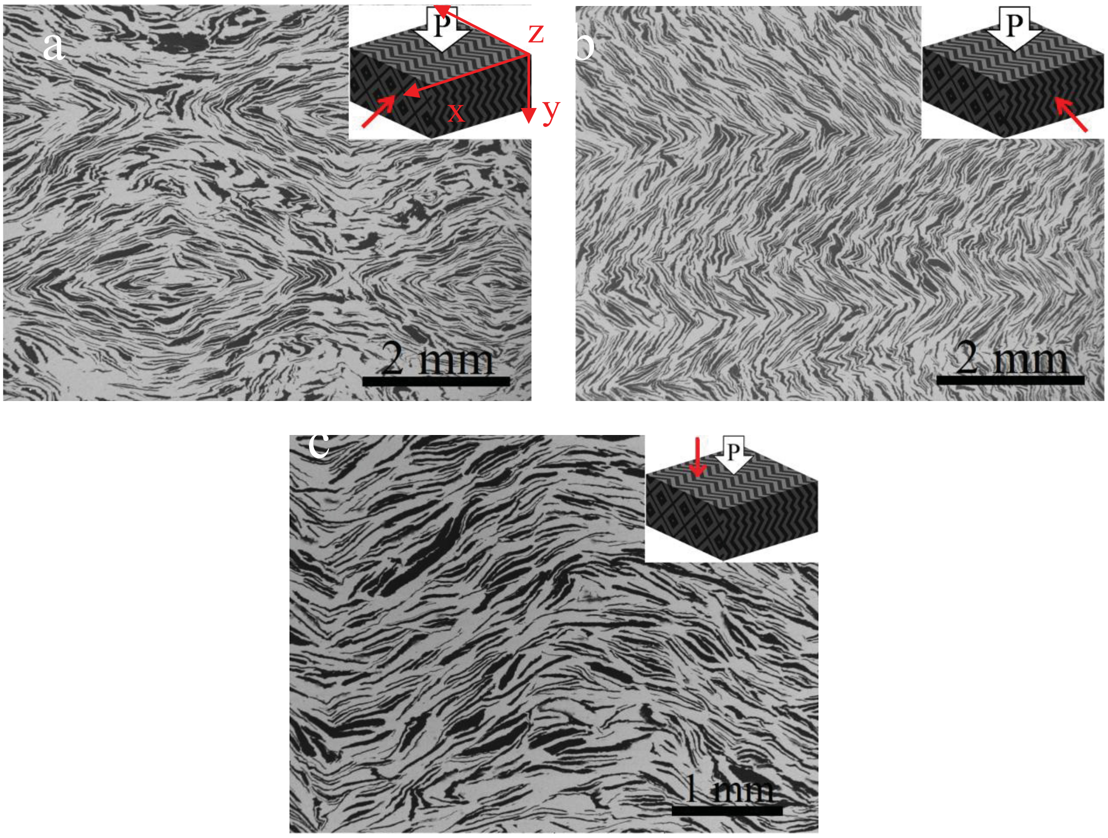

Fig. 3.27: SEM micrographs of the Al_F/40 vol.% G_f composites with the 3D arrangement of G_f using the punch 30-30: (a) side 1 view, (b) top view, and (c) side 2 view; arrows in insets show the observation direction with respect to the pressing direction

Owing to the nearly 3D arrangement of G_f, similar trends of thermal expansion behaviour measured in three directions are observed in dilatometry curves as shown in Fig. 3.28a. There is no stage contraction strain in the whole temperature range contrary to the 1D case, and the deformation after each thermal cycle becomes smaller. Further, the reduction in anisotropic degree is confirmed by dynamic CTE curves (Fig. 3.28b). The variation among the three directions becomes smaller than that 1D case.

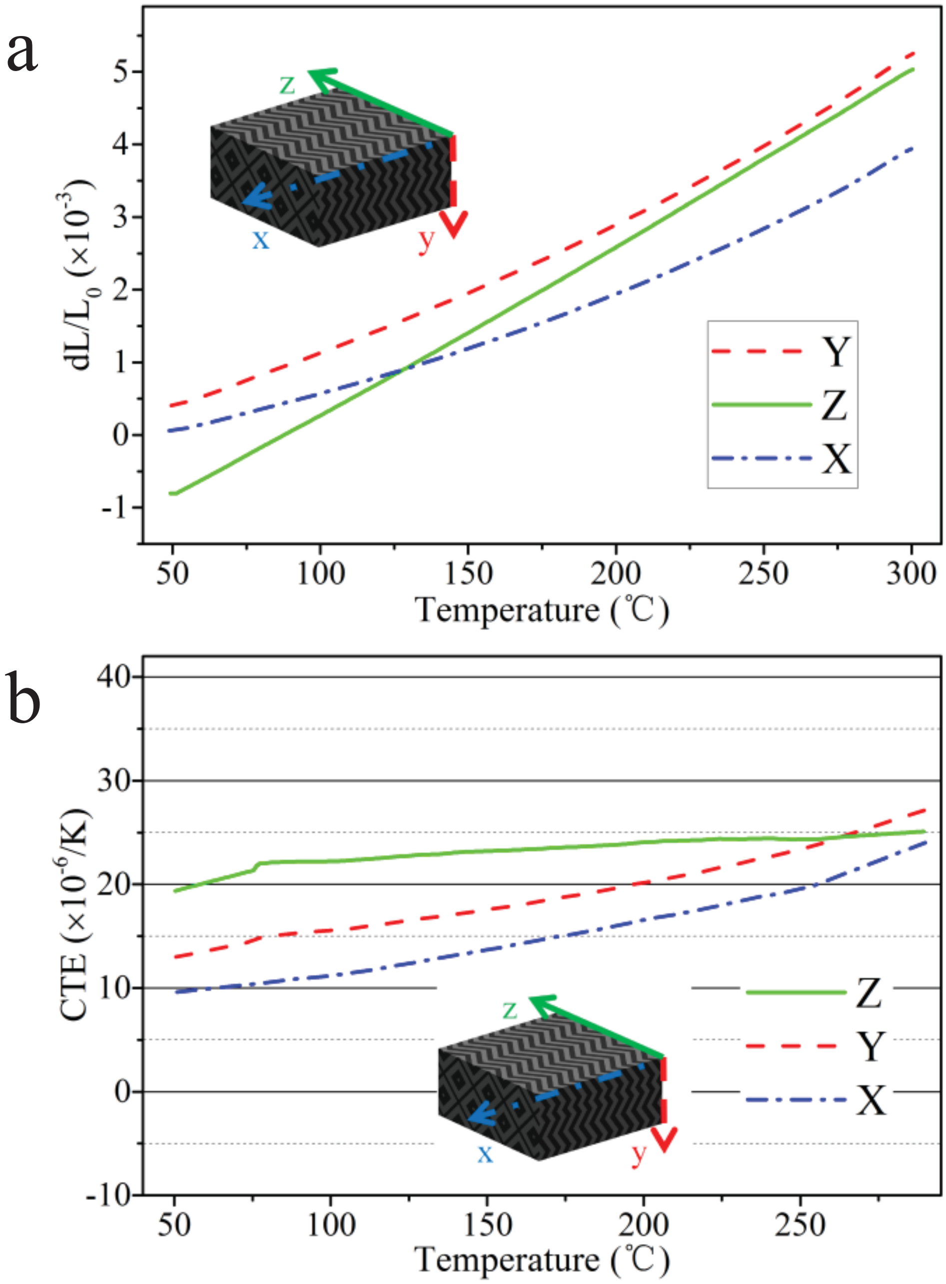

Fig. 3.28: (a) Dilation curves of the Al_F/40 vol.% G_f composites with the 3D arrangement of G_f, (b) the corresponding dynamic CTE vs. temperature.

Table 3.4 gives the average values of CTE in the temperature range from 50 °C to 150 °C measured in samples using different four types of punches, in which 30-30 displays the highest isotropy degree, but there is still a visible difference in CTE among different directions.

Table 3.4 Thermal properties of the Al/G_f composites with the 3D arrangements (average CTE values measured over the temperature range 50 – 150 °C and thermal diffusivity measured at room temperature)

	CTE (10^{-6}/K)			Thermal diffusivity (mm^2/s)			TC (W/m.K)		
	x	y	z	x	y	z	x	y	z
30-30	11.5	15.6	21.9	55	103	199	122	229	442
30-20	**8.1**	**10.7**	**20.8**	**94**	**209**	**235**	**209**	**465**	**523**
20-20	6.4	17.7	20.6	123	158	212	272	349	469
17-17	4.9	17.6	21.1	40.7	178	232	91	396	517

3.5.4 A novel approach to measure TC

It should be noticed that the sample used for TC measurement was typically prepared by machining the as-sintered sample. During this process, it is unavoidable to create some delaminated defects because of both the severe mechanical machining and weak Al-G_f interfacial strength. The materials exhibit higher strength along the plane direction than transversal one [35, 40, 51], thus, mechanical machining will leave different degree of damage in the sample from the different directions, which is not appropriate to reflect the TC of the composites. Emmanuel et al. [127] developed a new method to measure the TC of materials from the well-known laser flash technique. In this method, as illustrated in the Fig. 3.29, the front face of sample is heated periodically by a finite pulse width excitation while the temperature of rear face is recorded after each heat sequence by an infrared detector. For one measurement, the sample may undergo hundreds or even thousands of flashes different from the standard flash method with one flash. An averaging process can be conducted to reduce the noise standard deviation due to its statistical independence. Since the induced temperature variations can be small, it also suppresses the non-linear effects. The thermal diffusivity of the sample is estimated by an inverse approach including heat transfer and analog signal processing. Moreover, this method allows the sample shape to be cube, which can be prepared by diamond wire saw followed by polishing. In this way, the damage induced during preparing process can be minimized, and thermal diffusivity can be measured from different directions using one sample.

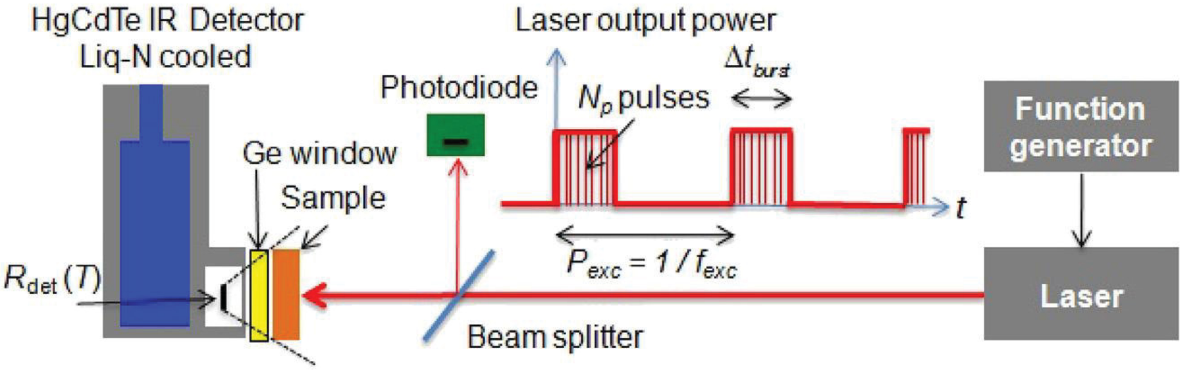

Fig. 3.29: Schematic illustration of experimental setup for TC measurement [127].

Table 3.4 gives the thermal diffusivities of the samples with the different 3D arrangements measured at room temperature via the new method and their calculated TC. Because they were fabricated using the different 3D punches, the values of TC vary as a result of the different arrangement of G_f. For all the samples, the lowest TC values appear along the x direction, the highest ones along the z direction. Fig. 3.30 shows the evolution of TC and CTE values as a function of measured angle based on the 1D arrangement, which is plotted using the plane strain and thermal transformation. It suggests that the smaller angle of graphite with respect to measured direction leads to the higher value in TC and CTE. The average angle of G_f to the z axis in Fig. 3.27c is smaller than that to the y axis in Fig. 3.27b, which corresponds to the variations in TC and CTE. Conversely, the average angle of G_f to the x axis in Fig. 3.27c is so large that it contributes to low values in TC and CTE. The experimental results indicate that the thermal properties of the Al/G_f composites are highly dependent on the arrangement of G_f at a given volume fraction of G_f.

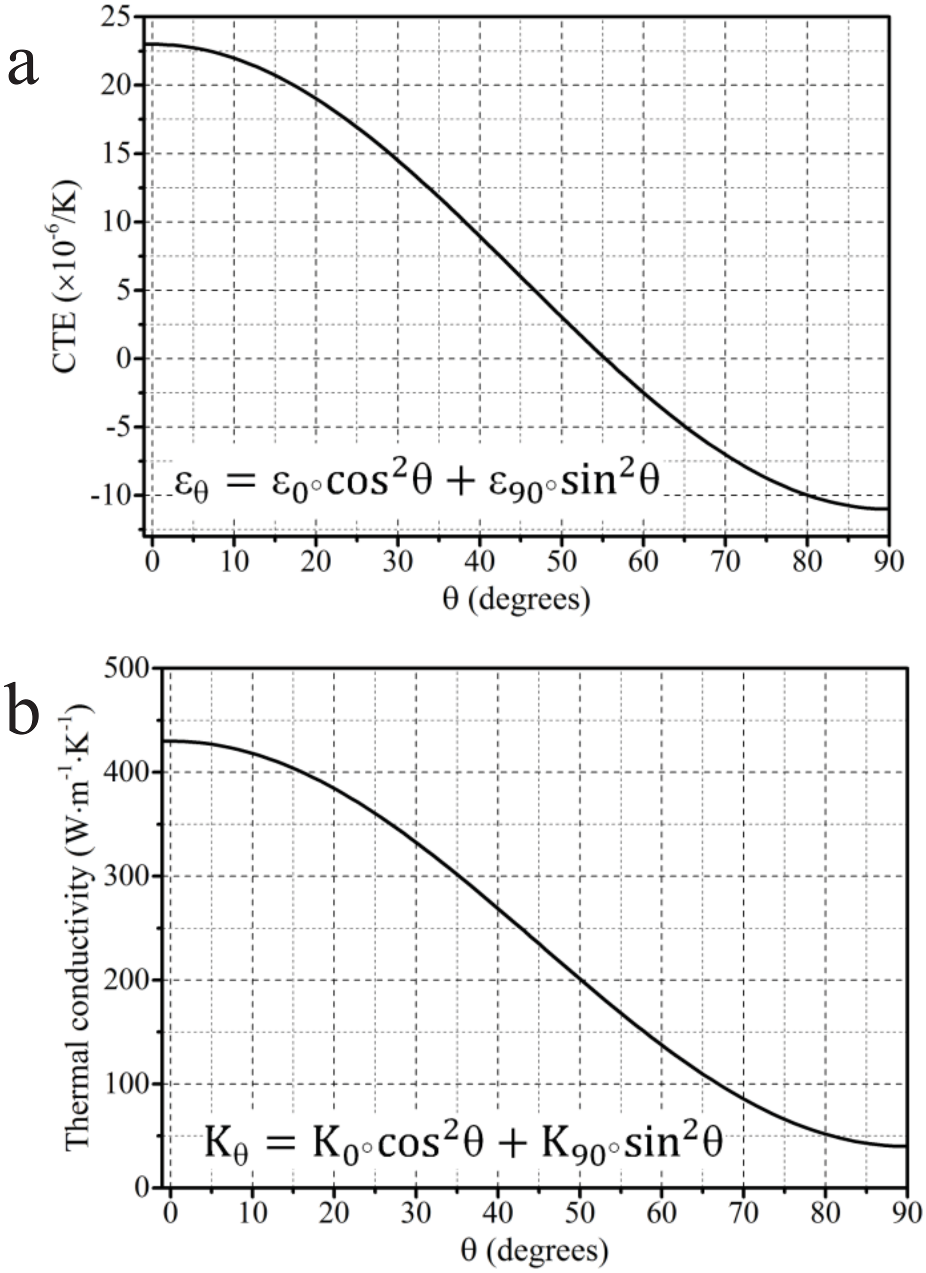

Fig. 3.30: The evolutions of (a) CTE and (b) TC as a function of measured based on the 1D arrangement (0° and 90° are the directions parallel and transversal to the graphite plane, respectively).

Nevertheless, among the results of the thermal properties, the composite made by punch 30-20 can be an appropriate candidate even if the CTE is not homogeneous in the plane (x: 8.1×10^{-6}/K and z: 20.8×10^{-6}/K) which can lead to some stresses when materials are solder paste on this composite material. For the thermal conductivity, even if there is a small difference of TC in the two directions of the plane (x: 209 W/m.K and z: 523 W/m.K), these MMC shows relative high in plane TC and large out of plane TC meaning that it can be used both in heat spreader and heat sink. It should be pointed out that the performance of thermal properties in the 3D arrangement is still anisotropic since none of the G_f arrangements is consistent with the ideal model. Therefore, how to properly design the 3D punch deserves more investigations in the future.

3.6 Conclusion

The CTE matching between heat sink and substrate materials is of importance to the reliability and life expectancy of electronic components. We propose a novel process to control the CTE performance of the Al/G_f composites via the architecture design of G_f. Both 2D and 3D arrangements of G_f in the Al matrix were successfully achieved via the step-by-step powder filling method and flake powder metallurgy using the specifically designed punches. The thermal properties of the composite with new architecture of G_f were characterized, whose typical thermal features are summarized in the Fig. 3.31. Above all, this technique opens a door of tailoring the thermal performance of the composites through the architecture design of reinforcement.

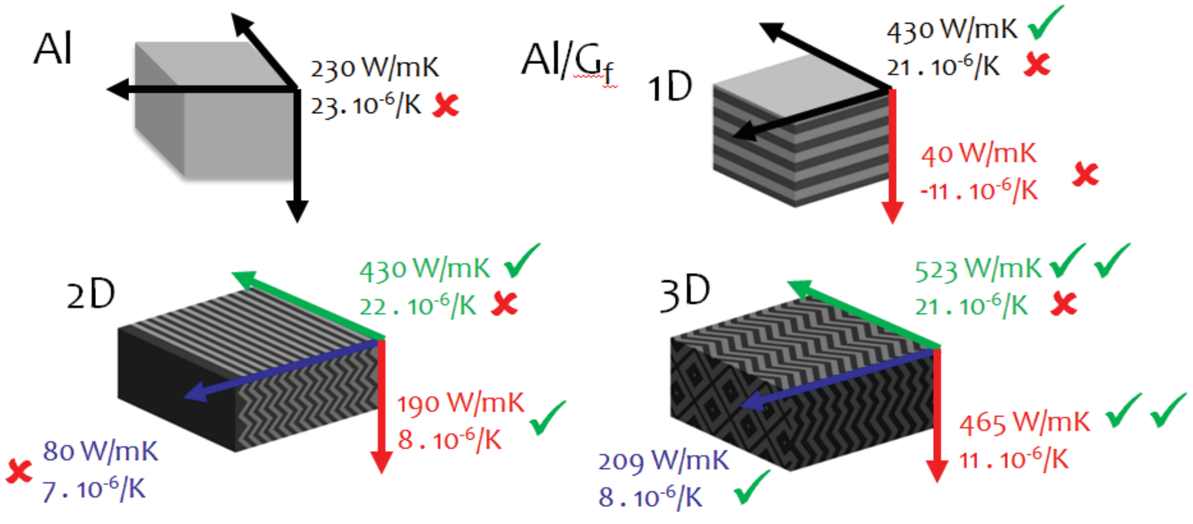

Fig. 3.31 : Thermal properties of Al and Al/40 vol.% G_f composites with 1D, 2D, and 3D arrangements of G_f.

Chapter 4

Ex-situ, in-situ and bio-mimetic routes to improve mechanical properties of the Al/G_f composite materials

4.1 Introduction

As discussed in chapter 2, the in-plane TC of the oriented Al/G_f composites has been improved with increasing volume fraction of G_f. For example, the TC can reach more than 400 W/m.K in the Al/40 vol.% G_f composite, better than that of pure Cu [28]. However, the strength of the composites became very low at the same time as a result of the brittle nature of G_f itself (e.g. flexural strength about 28 MPa along the in-plane direction for the Al/50 vol.% G_f composite [51]). Such low strength of the Al/G_f composite makes it impossible to be used in electronic packaging industry. In the past decades, most of the studies have focused on the fabrication, improvement of TC, tailoring CTE and investigation of the interfacial state between the matrix and reinforcement [25, 28, 33, 34, 37, 51, 53]. A few researchers have attempted to increase the strength of the composites by enhancing the interfacial bonding [35, 39-41, 59]. However, how to improve strength while maintaining a high TC is still an open question in the Al/G_f composite.

Since Al alloys have lower TC than pure Al, alloying route to enhance the strength was ruled out in this study for the sake of maintaining the TC of the Al matrix. To attain a higher strength and maintain ductility of the composite, nano-sized ceramic particles were often used to reinforce the metal matrix, so called nanocomposite [74]. It also has a limited influence on the degradation of TC of the pure Al matrix due to very small quantity of the added nano-sized particles. In general, ex-situ and in-situ routes are used to add nano-reinforcement inside metallic matrix. In-situ route is achieved by in-situ reaction with the metallic matrix to precipitate second phase of nano-size particles, while nanoparticles are added, during the mixing process, to the metallic powders for the ex-situ route. For the ex-situ route, it is commonly hard to get a uniform dispersion of nano-reinforcements in the metallic matrix as they easily form agglomerates. Ultrasonic treatment and ball milling processes have been identified as effective to get the uniform dispersion of nanoparticles by eliminating reinforcement agglomerations [76, 85, 94]. In addition to these composite approaches, creation of bio-mimetic nacre's nano-structure has been proved to be another effective way to enhance the strength of MMCs [45, 128]. Flake powder metallurgy applying on the Al powder with native Al_2O_3 skins was a simple and quick approach to produce Al/Al_2O_3 nanolaminated composites with improved mechanical properties [129].

In this chapter, we tried to improve mechanical properties of the Al/G_f composites by strengthening the Al matrix. A nano-sized silicon carbide (nano-SiC) was selected to reinforce the Al matrix using the ex-situ route, because it has the advantages of low cost and easy availability. Several dispersion methods were attempted in order to achieve a uniform distribution of nano-SiC in the Al matrix aiming at increasing its strength, including a novel mechanical mixing using a resonant acoustic mixer (RAM), ultrasonic treatment of nano-SiC in water and ball milling process. Semi liquid process was also used in order to add a small quantity of liquid phase to the solid metallic powder and the nano-sized reinforcement. AlSi10Mg alloy, which has a melting point close to 580 °C [55], becomes the liquid phase when vacuum hot pressing of Al + AlSi10Mg + nano-SiC is conducted at 620 °C. This technique was considered to be helpful for rapid densification of the composite producing a strong bonding between the matrix and reinforcement [33, 130]. For the in-situ route, commercial AlSi10Mg/nano-TiB_2 composite powder was used. Further, the effect of flake powder metallurgy on mechanical property of the nanocomposites was also investigated. 3-point bending test was applied to measure the mechanical property of the composites, and SEM was used to analyse the microstructure of the composites and the distribution of the nanoparticles.

4.2 Flexural strengths of the Al (or Al + AlSi alloy)/G_f composites

The Al/G_f composites were prepared using the same procedure as described in chapter 2. The volume fraction of G_f in the composites was fixed at 10, 20, 30 and 40%. In addition, 5 vol.% Al-12 wt.% Si alloy powder, with an average diameter of 50 μm (Fig. 4.1), was added to spherical Al powder and then mixed with 10, 20, 30 and 40 vol.% of G_f. For comparison, a sample was also prepared using spherical Al (Al_S) powder without any reinforcement and Al-Si alloy. The as-sintered sample was cut using a diamond wire saw for preparing the bending test sample, and the manner of sectioning is illustrated in Fig. 4.2a. The dimension of the bending test sample was 2 × 7 × 40 mm^3 designed according to ASTM Standard D790 [131]. The final sample (Fig. 4.2a) was obtained by mechanical polishing using 500-grip SiC paper. The 3-points bending test was carried out using a universal testing system (Instron® 3369, Fig. 4.3a) with a loading rate of 0.01 mm/sec at room temperature. The bending test process including the used parameters is illustrated in Fig. 4.3b. Three bending tests were repeated for each sample to obtain reproducible result. After testing, the exporting load-displacement data was converted into flexural stress-strain curve via the following equation.

$$\sigma_f = \frac{3PL}{2bt^2} \tag{4.1}$$

$$\varepsilon_f = \frac{6Dt}{L^2} \tag{4.2}$$

where σ_f and ε_f represent the flexural stress and strain, respectively. P is the load, D is the maximum deflection of the center of the beam, and L is support span. b and t are width and thickness of the beam, respectively. Herein, L was fixed at 30 mm. b and t were measured using micrometer.

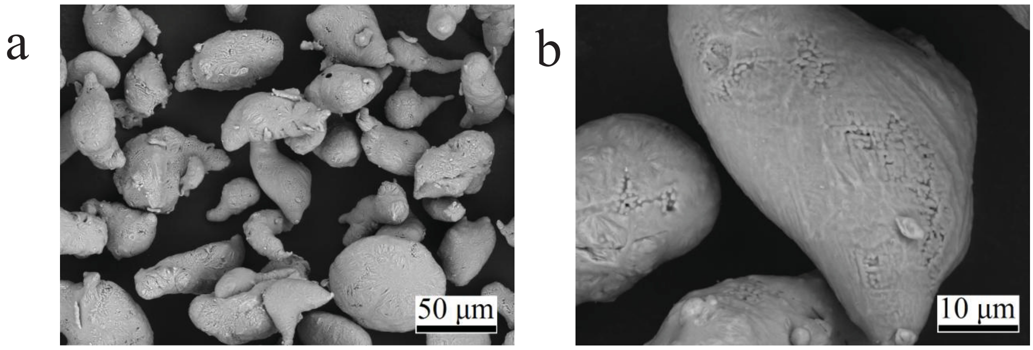

Fig. 4.1: (a) low- and (b) high-magnification SEM micrographs of the AlSi alloy powder.

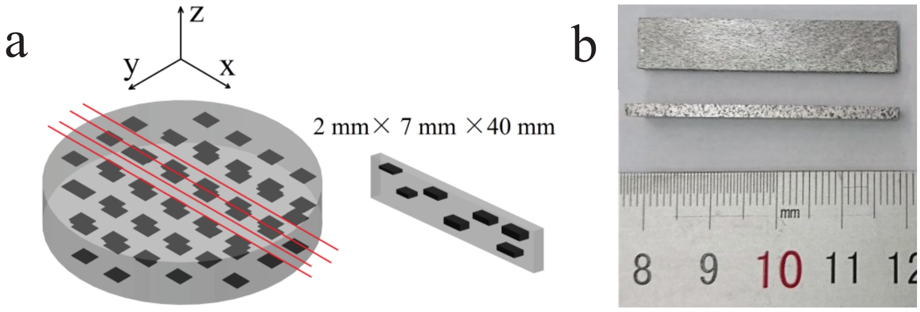

Fig. 4.2: (a) Schematic illustration of sectioning the as-sintered sample for bending test and (b) photograph of the final bending test samples.

Typical flexural stress strain curves of the tested specimens are shown in Fig. 4.4. Both yield strength and ductility decreased with increasing the content of G_f, which is accordance with the previous results [51]. Additionally, with the addition of 5 vol.% AlSi in the Al matrix, MMCs shows a small increase in flexural stress compared with those without AlSi. The highest strength and excellent ductility is shown for the pure Al sample. Herein, the flexural strength of pure Al was determined by the stress at 5% strain as it didn't break during the test [131].

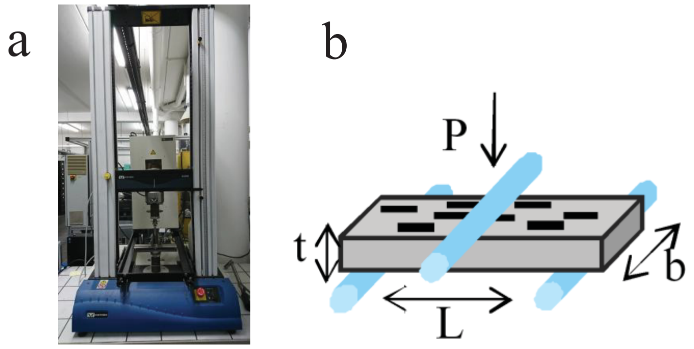

Fig. 4.3: (a) Photograph of the bending test machine and (b) schematic illustration of bending test.

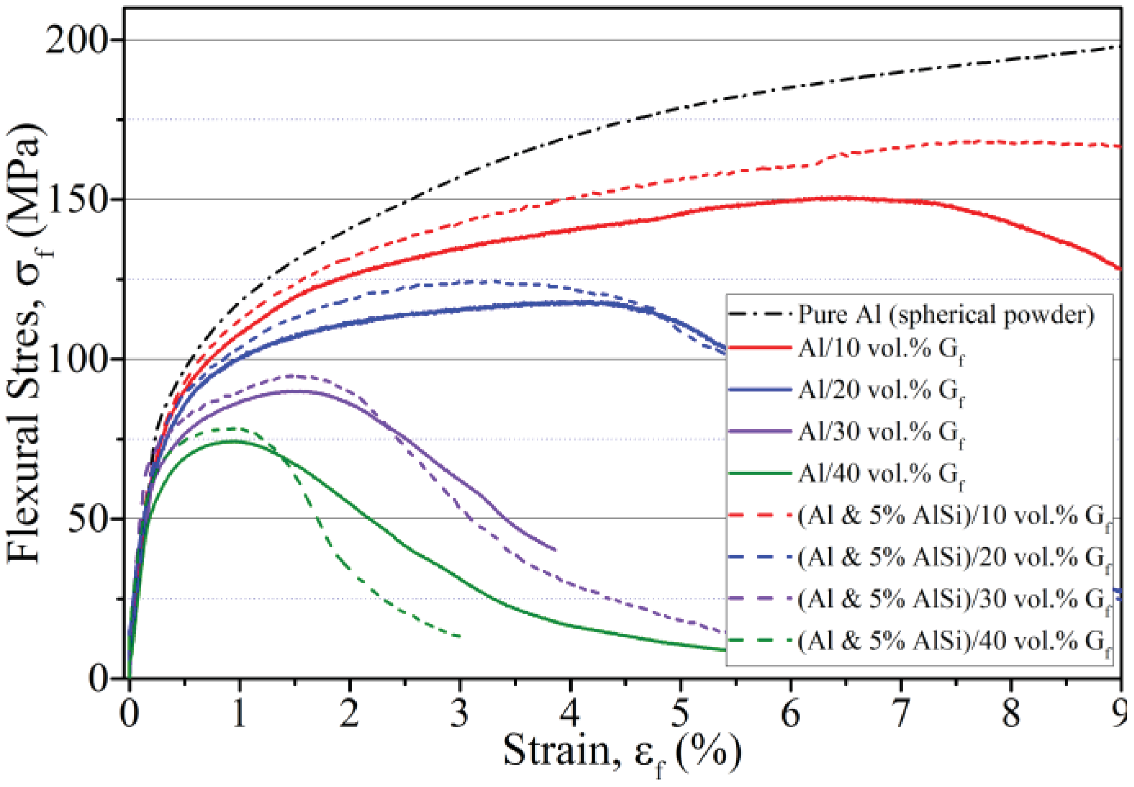

Fig. 4.4: Flexural stress strain curves of the pure Al and Al (or Al+5 vol.% AlSi)/G_f composites with different volume fractions of G_f.

4.3 Enhanced strength in the Al/G_f composite using flake powder metallurgy

4.3.1 Al/Al_2O_3 composite with a lamellar structure

Al powder naturally has an Al_2O_3 skin covering its surface, thus, the bulk material after consolidation can be regarded as an Al/Al_2O_3 composite. In this work, Al/Al_2O_3 laminated composite was fabricated by vacuum hot pressing (VHP) using the flake Al (Al_F) powder obtained by ball milling of the spherical Al (Al_S) powder (refer to chapter 3). Al_F powder with a two-dimensional flat morphology was an ideal building block for assembly into a bulk lamellar structure [128] and the relatively low apparent density facilitated the alignment of the Al_F powder during compaction. The measured density of Al_F/Al_2O_3 composite was 2.72 g/cm^2 being higher than that obtained from the Al_S powder (2.70 g/cm^3), which can attribute to the increase of alumina content as a result of enlargement of surface area from sphere to flake [38].

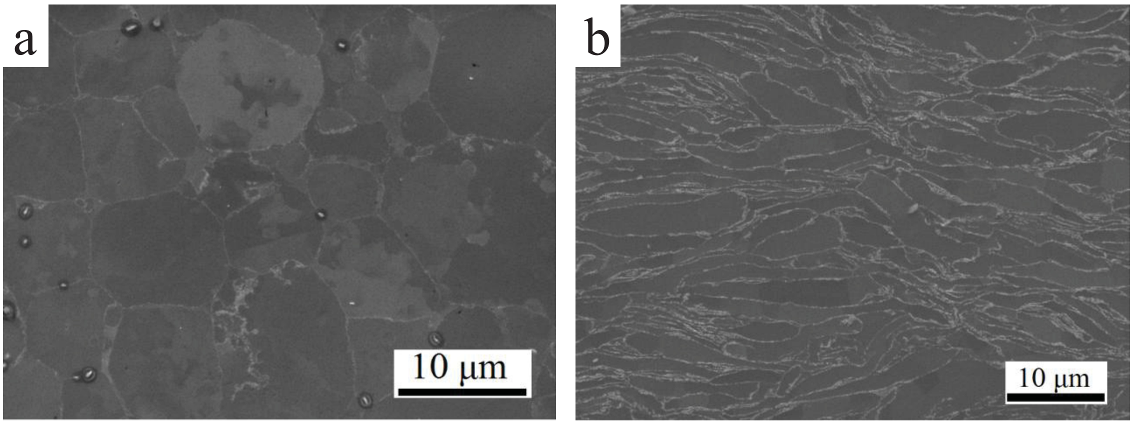

Fig. 4.5: SEM micrographs of the pure Al specimens fabricated by vacuum hot pressing using: (a) the spherical and (b) flake Al powders.

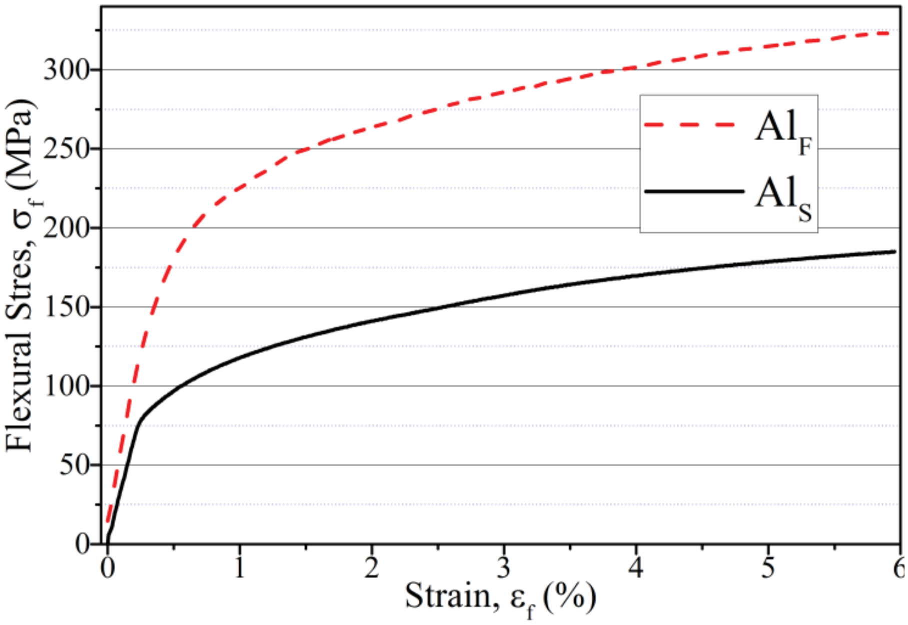

Fig. 4.6: Flexural stress strain curves of the pure Al specimens obtained from the spherical and flake Al powders.

Fig. 4.5 shows the SEM micrographs of the samples obtained from the Al_S and Al_F powders. Due to the use of water at the last stage of polishing, the Al matrix was slightly etched at the grain boundaries between the Al grains. The sample sintered using Al_S powder has a homogeneously equiaxed grain structure (Fig. 4.5a), while the other one exhibits a lamellar structure (Fig. 4.5b) due to the characteristic of soft micro grained Al lamellae embedded in the hard Al_2O_3 lamella matrix. The microstructure analysis is in accordance with the previous report [38]. For both of them, the microstructures were highly linked with the initial morphology of the powders (quasi absence of grain deformation during the uniaxial densification process). The measured TC of the Al_F sample was 211 ± 1 W/m.K being a little bit lower than that of the Al_S sample (219 ± 2 W/m.K), while a 70% increase in bending strength was achieved for the Al_F sample (315 MPa at 5% strain) comparing with the Al_S one (179 MPa at 5% strain) as shown in Fig. 4.6. Wu et al. [132] indicated that such a high strength originates from the development of high back stress during heterogeneous yielding, which was known as back-stress hardening. Therefore, the lamellar structure formed using Al_F powder can be an effective method to strengthen Al/G_f composite materials.

4.3.2 Flexural strength of the Al_F/40 vol.% G_f composite

A maximum flexural strength of 107 MPa at 1.14% strain was obtained for the Al_F/40 vol.% G_f composite; this value is higher than that of the Al_S/40 vol.% G_f one (74 MPa at 0.95% strain) as shown in Fig. 4.7. The strengthening effect of the lamellar structure is thus clear, even though the presence of G_f degraded the overall mechanical properties compared to the pure Al matrix.

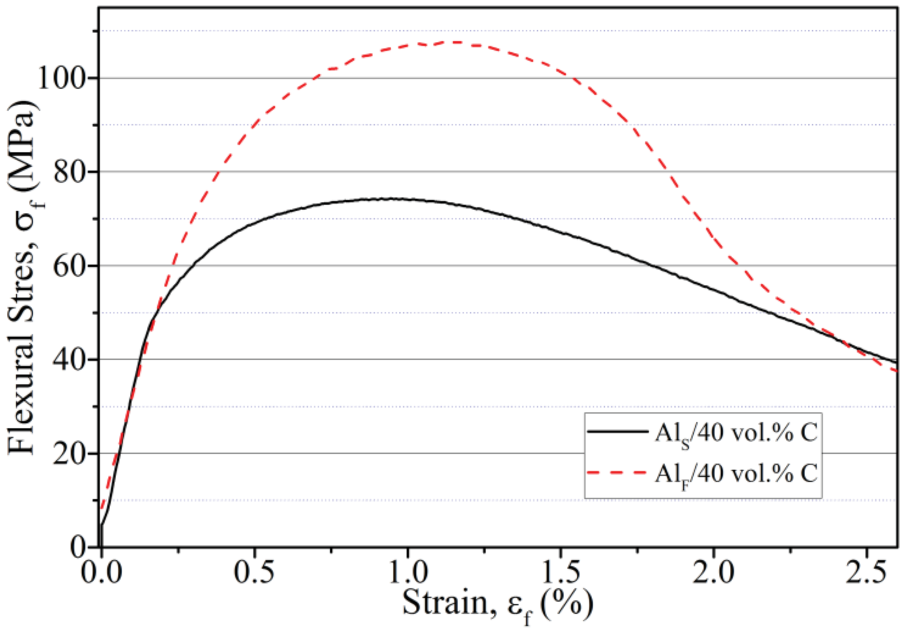

Fig. 4.7: Flexural stress strain curves of the $\mathrm{Al_S}$/40 vol.% $\mathrm{G_f}$ and $\mathrm{Al_F}$/40 vol.% $\mathrm{G_f}$ composites.

Fig. 4.8 revealed that massive dimples are distributed on the fracture surfaces for both composite samples, while a more uniform distribution and smaller size of equiaxed dimples can be observed in the $\mathrm{Al_F}$ matrix compared to the $\mathrm{Al_S}$ matrix. This peculiar behaviour indicates that $\mathrm{Al_F}$ matrix presents a highly ductile fracture behaviour [92]. It has to be noticed that the use of flake or spherical Al powder do not change the overall TC of the composite materials; TC is equal to 431 ± 6 W/m.K for the $\mathrm{Al_F}$/40 vol.% $\mathrm{G_f}$ composite whereas TC of the $\mathrm{Al_S}$/40 vol.% $\mathrm{G_f}$ is equal to 439 ± 2 W/m.K.

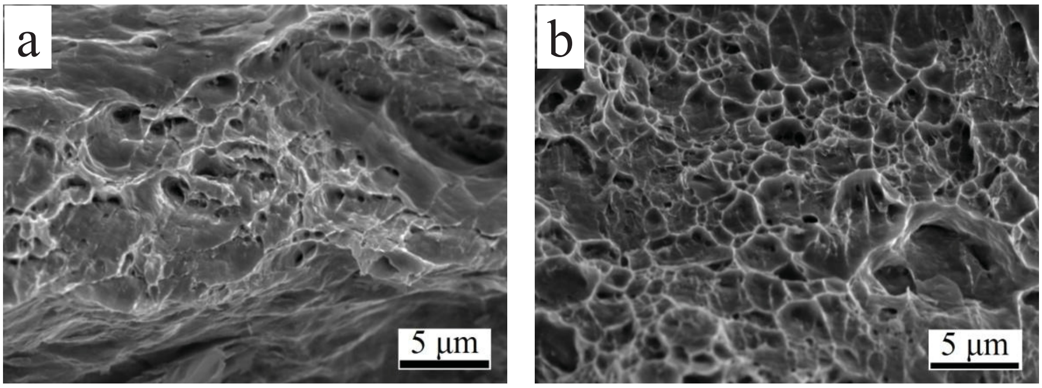

Fig. 4.8: SEM micrographs showing the fracture surfaces of (a) the $\mathrm{Al_S}$ and (b) $\mathrm{Al_F}$ matrices.

4.4 Al nanocomposites reinforced with in-situ $\mathrm{TiB_2}$ nanoparticles

A specially designed nano-$\mathrm{TiB_2}$ decorated AlSi10Mg powder with the average particle size of 40 µm was fabricated by in-situ reaction of $\mathrm{K_2TiF_6}$ and $\mathrm{KBF_4}$ in aluminium melt followed by gas atomization [92, 133]. The chemical composition of the AlSi10Mg/TiB_2 composite powder is 9.8 wt.%, 0.32 wt.% Mg, 7 wt.% TiB_2 (around 4.3 vol.%) with Al balance [133]. As shown in Fig. 4.9a, this composite powder exhibits a globular shape with attached satellites. Apart from a few residual agglomerations as marked by red circles in Fig. 4.9b, most of fine TiB_2 particles are uniformly distributed at the equiaxed grain boundaries within the particle. The melt point of this composite powder is 569 °C; this temperature was measured via a differential scanning calorimetry (DSC, 8000 Pyris Diamond PERKIN ELMER).

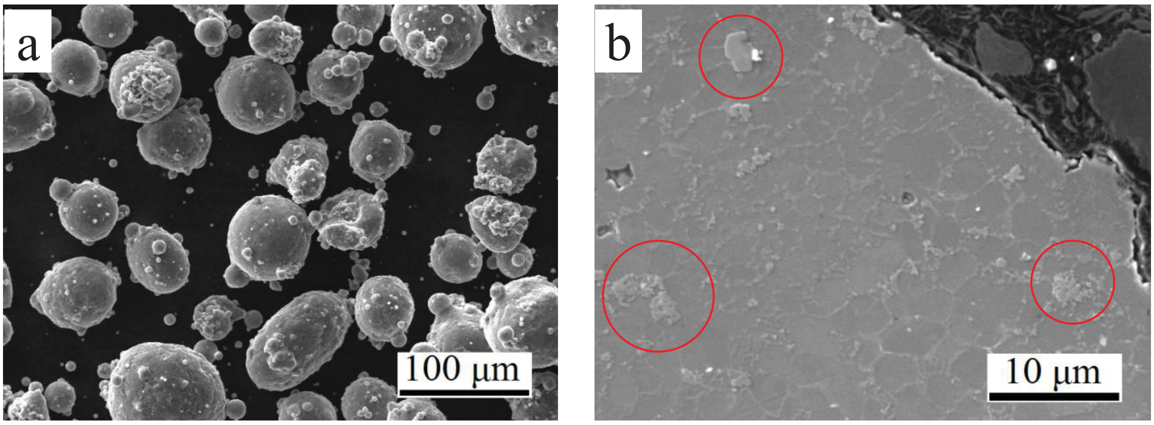

Fig. 4.9: SEM micrographs of the TiB_2/AlSi10Mg composite powder: (a) particles, and (b) cross-sectional morphology of a particle.

Al (sphere or flake) powder was mixed with 5 vol.% of the AlSi10Mg/TiB_2 composite powder or the pure AlSi10Mg alloy powder, in which the volume fraction of TiB_2 in the mixture powder was around 0.2 vol.%. The mixture powders were consolidated by VHP at 620 °C, where the AlSi10Mg alloy was liquid. Fig. 4.10a shows the microstructure of the Al_S/5 vol.% AlSi10Mg&TiB_2 composite. The agglomerations of TiB_2 (marked by red circles) are distributed separately and randomly all around the Al matrix, and a high magnification micrograph (Fig. 4.10b) shows the diameter of agglomeration region approximate to the size of the AlSi10Mg/TiB2 powder. However, the agglomerations of TiB_2 became more intense comparing to its initial distribution within the initial particle, and there is almost no trace of TiB_2 apart from the agglomeration region.

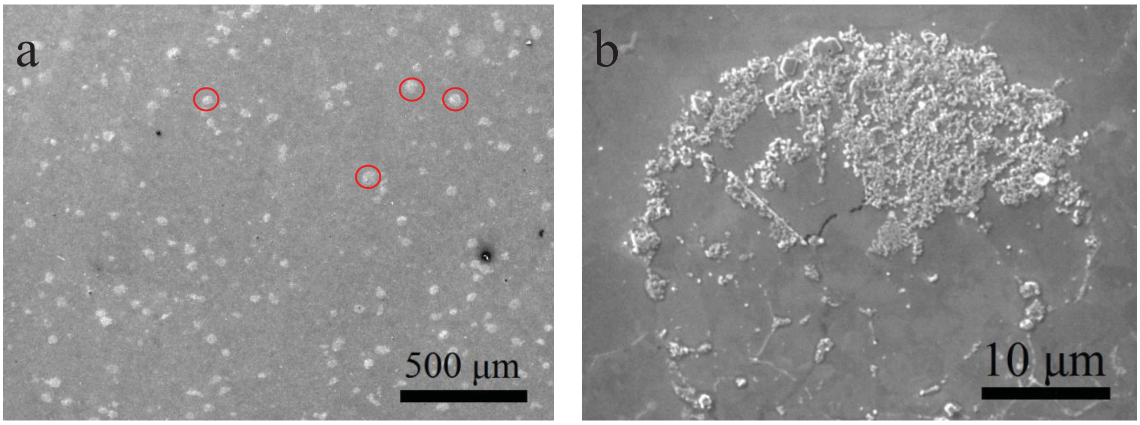

Fig. 4.10: (a) SEM micrographs of Al_S/5 vol.% AlSi10Mg&TiB_2 composite (b) TiB_2 agglomeration region.

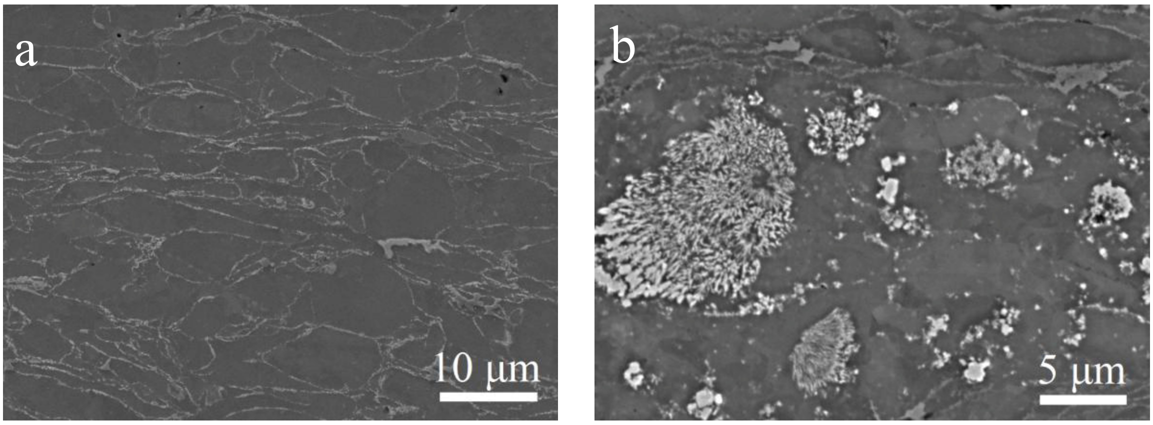

Fig. 4.11: SEM micrographs of Al_F/5 vol.% AlSi10Mg&TiB_2 composite: (a) region without TiB_2 and (b) agglomeration of TiB_2.

A similar phenomenon can be observed in the Al_F/5 vol.% AlSi10Mg&TiB_2 composite (Fig. 4.11). This can be the consequence of melt/solidification process, in which the liquid phases tend to fuse together due to the surface tension and the front of liquid push nano-TiB_2 and formed much bigger agglomerations at the end of solidification. The results suggest that semi-liquid process is not helpful for the dispersion of in-situ nanoparticles.

As exhibited in Fig. 4.12, a small increase in flexural strength, by adding 5 vol.% of AlSi10Mg/TiB_2 powder in the Al_S matrix, was measured. It has to be mentioned that similar effect can be observed if we use AlSi10Mg powder instead of AlSi10Mg/TiB_2 one. The enhanced strength in the Al_S matrix can be attributed to the addition of AlSi10Mg alloy, while the contribution from TiB_2 is very limited. On the other hand, an opposite tendency can be observed for Al_F matrix. Particularly, the addition of 5 vol.% of AlSi10Mg/TiB_2 powder in A_F matrix resulted in larger extent of decrease in strength comparing to that using the pure

AlSi10Mg powder. The AlSi10Mg phase may soften the Al_F matrix leading to a decrease of the overall strength, and the agglomeration, after the sintering process, of the TiB_2 nanoparticles may further weaken the overall strength of the composite materials.

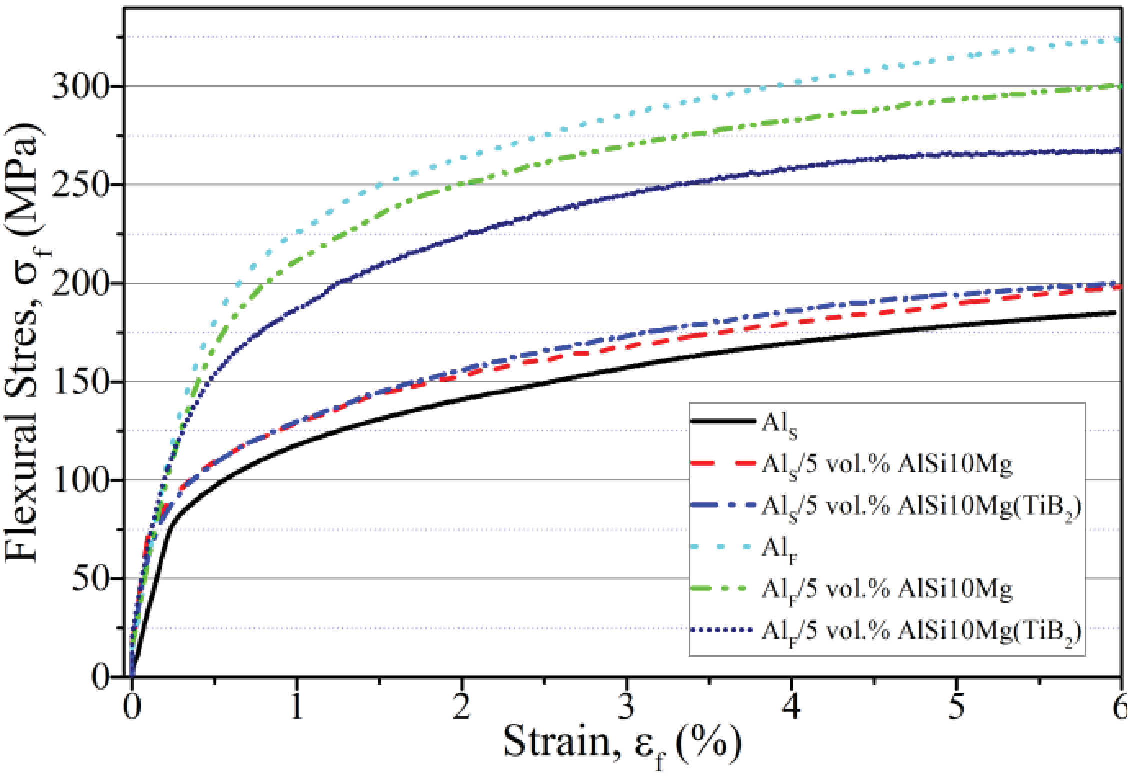

Fig. 4.12: Typical flexural stress strain curves obtained from the different materials: Al_F/(5 vol.% AlSi10Mg&TiB_2); Al_S/(5 vol.% AlSi10Mg&TiB_2); Al_F/(5 vol.% AlSi10Mg); Al_S/(5 vol.% AlSi10Mg). (Pure Al specimens obtained from the spherical and flake Al powders act as the references)

Thus, as this strategy was employed in the Al/G_f composites for improving its strength, a comparable result was obtained. As shown in Fig. 4.13, the addition of AlSi10Mg/TiB_2 powder had very limited effect on the improvement of flexural strength of the Al_S matrix and worsen the strength of the Al_F matrix. There was no obvious difference in ductility among the samples. Fig. 4.14 shows that a ductile fracture mode presented in both samples, whose features are similar to Fig 4.8. Additionally, TiB_2 nanoparticles or clusters are visible at the bottoms of the dimples (marked by red arrow in the Fig. 4.14b) suggesting the ductile rupture was started by debonding from the of Al-TiB_2 interface [133]. Consequently, such a route of introducing TiB_2 in the Al matrix aimed to improve the mechanical properties of the G_f/Al composites is not recommended.

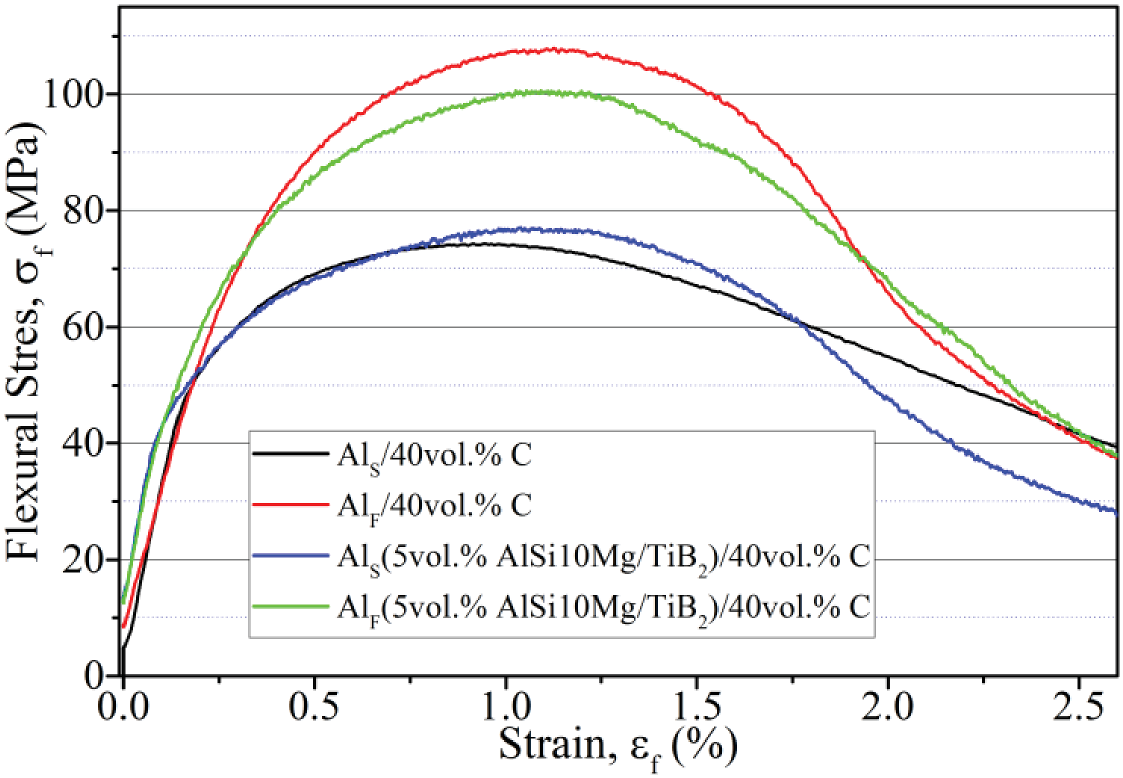

Fig. 4.13: Flexural stress strain curves of the (Al_S + 5 vol.% AlSi10Mg&TiB_2)/40 vol.% G_f and (Al_F + 5 vol.% AlSi10Mg&TiB_2)/40 vol.% G_f composites (the curves from the Al_S/40 vol.% G_f and Al_F/40 vol.% G_f composites act as the references).

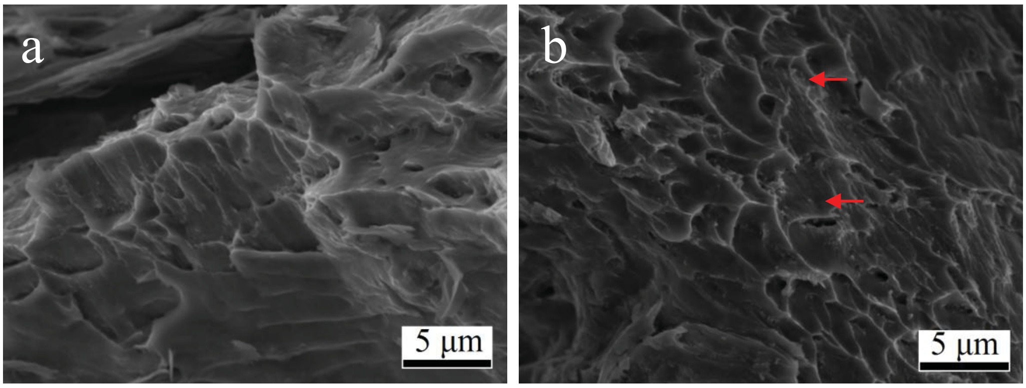

Fig. 4.14: SEM micrographs showing the fracture surfaces of (a) the Al_S/5 vol.% TiB_2/AlSi10Mg and (b) Al_F/5 vol.% AlSi10Mg&TiB_2 matrices.

4.5 Incorporation of nanosized SiC in the Al matrix via the ex-situ route

4.5.1 Dispersion of nanosized SiC

4.5.1.1 Mechanical mixing using a RAM

As received SiC powder with β structure was purchased from US Research Nanomaterials Inc. The grain size range and density of SiC are 45 - 65 nm and 3.216 g/cm^3, respectively, provided by the supplier. Fig. 4.15a shows the SEM micrograph of as received SiC, in which big agglomerations was found with some sizes more than 10 μm. RAM was used to disperse nano-SiC in Al powder since it can generate high intensity acoustic field facilitating the movement of the powder and inducing mixing.

Spherical Al powder (refer to chapter 2 for more information) was mixed 1 vol.% of as received nano-SiC using a RAM with an acceleration of 90 g for 20 s. Fig. 4.15b shows that Al particle was covered with some nano-SiC particles. However, SiC agglomeration still appeared in the mixture after mixing (marked by red arrow in Fig. 4b). Further, the mixture powder was consolidated via VHP. Big porosity was found in the microstructure (pointed out by red circles in Fig. 4.16a), and there is no solid cohesion for some particles in the porosity region (Fig. 4.16b), which is detrimental to the densification of the material. This trial indicates that it is hard to eliminate or break the agglomeration of nano-SiC via mechanical mixing process using a RAM.

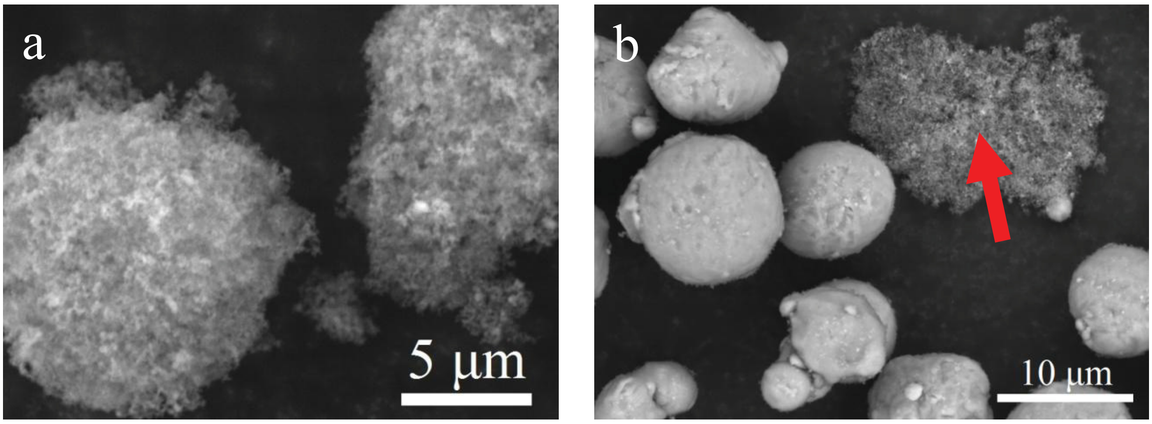

Fig. 4.15: SEM micrographs of (a) the as received nano SiC and (b) mixture of Al powder and as-received nano SiC using a RAM.

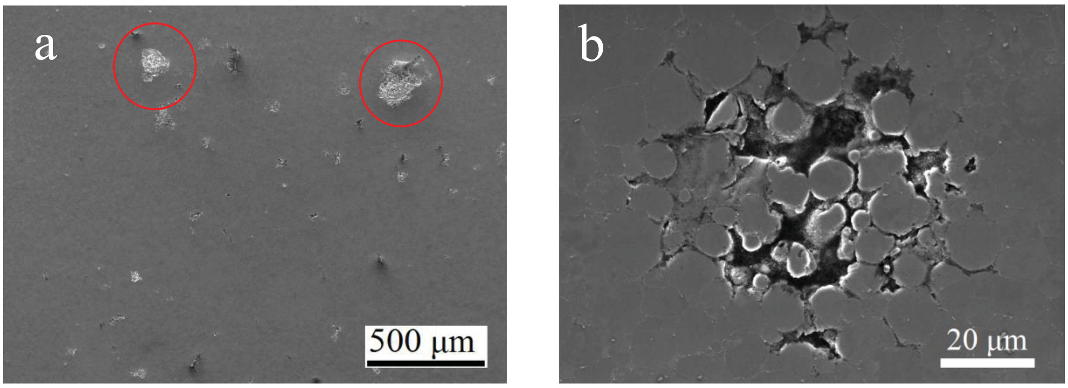

Fig. 4.16: SEM micrographs of the Al/1 vol.% nano-SiC (as received) composite fabricated by VHP showing the porosities in the composite: (a) low- and (b) high-magnification.

4.5.1.2 Ultrasonic processing of nano-SiC in an aqueous medium

Generally, ultrasonic wave was applied to break nanoparticle agglomerations in the liquid medium [75]. Distilled water was used to disperse nano-SiC as it is easily available. Fig. 4.17a illustrates the procedure of adding nano-SiC into the Al powder assisted with ultrasonic treatment. To prepare 25 g of Al/nano-SiC mixture with 1 vol.% of nano-SiC, 0.3 g of as received nano-SiC was put in a beaker containing 200 ml of water and stirred for a while. Then, a titanium waveguide coupled with an ultrasonic converter (BANDELIN® Sonopuls HD 2200, BANDELIN) was dipped into the suspension for ultrasonic processing for 1 hour. Then, the suspension was centrifuged to obtain a SiC slurry (Fig. 4.17b), and the sediment was reused to repeat ultrasonic processing to break the rest of agglomerations. The SiC slurry was added in the Al powder by specific quantity with the level of liquid equal to the top of Al powder. Then, the Al powder immersed with the SiC slurry was dried in an oven at 100 ℃. This step was repeated in order to use up all the SiC slurry. However, it was predicted that it would take more than 1000 cycles to consume all the SiC slurry, and it was failed to complete it. In order to check the dispersion of nano-SiC after drying, several droplets of SiC slurry were dropped on a graphite sheet then underwent the same drying process. Fig. 4.18 shows the SEM micrograph of nano-SiC on the graphite sheet after evaporating the water. Most of nano-SiC particles accumulated and formed clusters, and big agglomeration being shown in Fig 4.15 was not found. Thus, ultrasonic treatment followed by centrifugal process can remove big agglomeration in the as received nano-SiC, but the re-agglomeration of nano-SiC took place during the drying process.

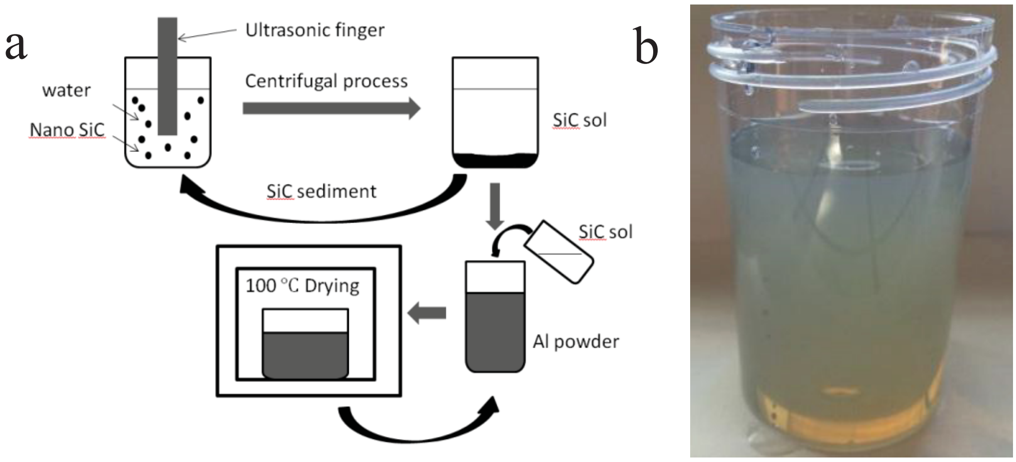

Fig. 4.17: (a) Schematic illustration of adding nano-SiC in the Al powder and (b) photograph of the nano-SiC slurry.

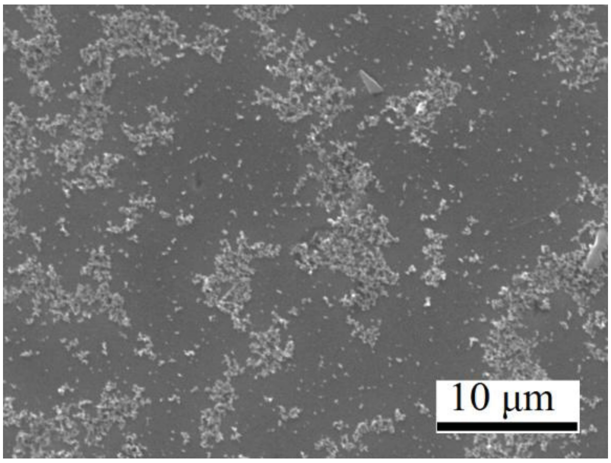

Fig. 4.18: SEM micrograph of the nano-SiC ultrasonically treated in the aqueous medium followed by drying on a graphite sheet.

4.5.1.3 Mixing of nano-SiC with the Al powder using a hetero-agglomeration method

The previous study has pointed out the existence of silica on the surface of nano-SiC particles make it hard to break the agglomerations, and hydrofluoric acid (HF) solution was used to remove this layer in order to achieve de-agglomeration [134]. In our experiment, each time, 0.05 g of as-received nano-SiC was put in 20 ml of HF solution with concentration of 0.1 mol/L, and stirred for 1 hour then, the suspension was centrifuged to separate the liquid from solid. The HF treated nano-SiC was rinsed with distilled water for three times. Such nano-SiC was treated by ultrasound further in the water to make nano-SiC slurry.

The as-obtained SiC slurry after ultrasonic treatment was still turbid after 2 days of resting indicating that the SiC particles had formed stable colloid in the aqueous medium. It has been reported that SiC nanoparticles take negative charge in water [81]. In addition, Al powder has a layer of alumina on its surface naturally. Mehdi [135] reported that alumina takes positive charges in water. Therefore, SiC and Al powder suspension can be mixed in the aqueous medium by applying a hetero-agglomeration effect [136]. The hetero-agglomeration effect refers to electrostatic attraction of two types of particles taking opposite charges.

The zeta potential measurements were carried out to confirm the charges of the SiC and Al powder particles in the aqueous medium. 0.02 g SiC and 2 g Al powders were dispersed in 200 ml of distilled water to obtain the corresponding slurry, which were used for zeta potential measurements. Aqueous solutions of 0.1 M sodium hydroxide and 0.1 M hydrochloric acid were used to adjust the pH of SiC slurries and Al powder suspension. A pH meter was used to measure the pH values. The zeta potential was measured as a function of pH. The result is shown in Fig. 4.19. Both SiC and Al particles take positive charge in the base range. Al powder takes positive charge in the solution with pH value lower than 7, while SiC shows negative charge in the pH range 5 – 7. It is noted that the distilled water in the Lab shows a pH around 6. Therefore, hetero-agglomeration of nano-SiC and Al powder can be achieved in the as-obtained aqueous suspension.

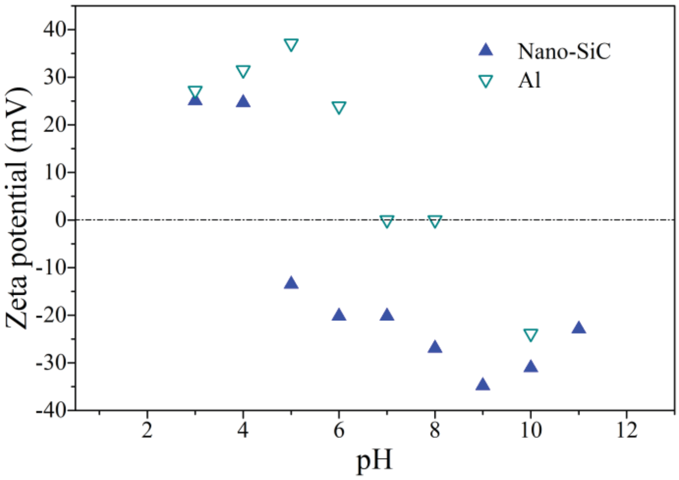

Fig. 4.19: Zeta potential of the Al powder and nano-SiC in water as a function of pH values.

A schematic illustration of this processing method is shown in Fig. 4.20. At first, the nano-SiC slurry was prepared using the same parameters as used for the zeta potential measurement (0.02 g nano-SiC in 200 ml of water) followed by ultrasonic treatment for 30 min, and Al powder dispersed in water via stirring. Next, the nano-SiC/water suspension was once poured into the Al powder/water suspension while stirring. Then, the excess water was separated from the mixture suspension by a filtration setup. It should be noticed that the removed water may not be totally transparent especially when the volume fraction of nano-SiC in Al powder is more than 1% indicating some nano-SiC still existed in water after hetero-agglomeration mixing. Finally, the obtained mixture powder was dried in a vacuum chamber at room temperature.

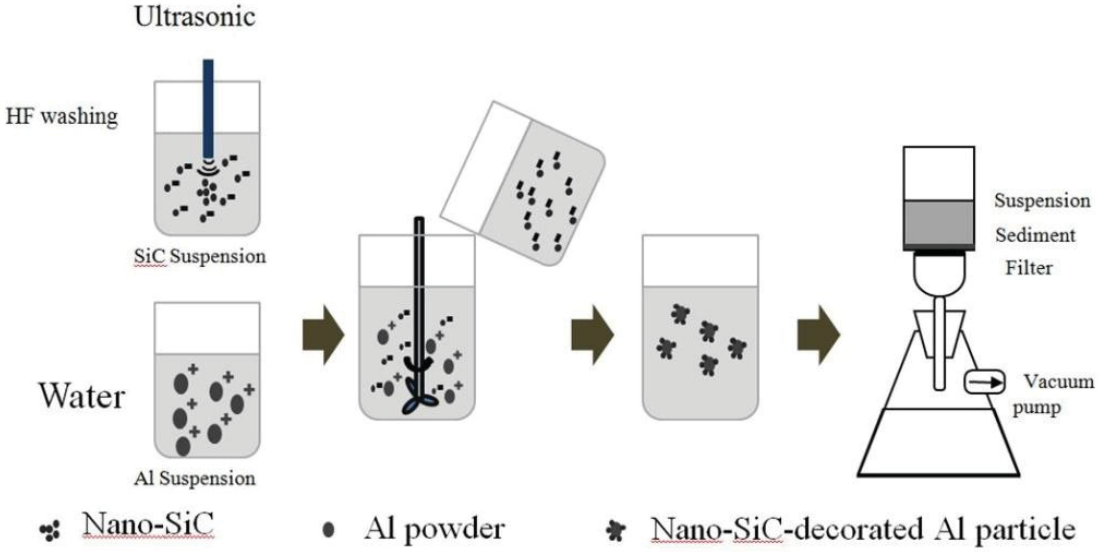

Fig. 4.20: Schematic illustration of the processing method employed to mixing the nano-SiC and Al powders.

Fig. 4.21 shows the morphology of Al/1 vol.% nano-SiC composite powder, where the surface of Al particles was decorated with nano-SiC compared with the pure Al powder (Fig. 2.1a in the chapter 2). However, some small agglomerations of nano-SiC was distributed on the surface of Al particles (Fig. 4.21b), and some big nano-SiC clusters remained. The formation of the agglomerates may be attributed to the drying processing. Another reason may be that the nano-SiC/water suspension was mixed with the Al/water suspension in a short time, which may quickly change the pH condition of the suspension so that the clustering of nano-SiC particles could occur. Therefore, mixing process could be carried out more gently in order to avoid this occurrence.

A peristaltic pump (Masterflex® L/S® model 77390-00) was used to deliver the SiC/water suspension to the Al particles/water suspension drop by drop. But after filtering process, the transparency of the filtered liquid seemed similar compared with that of as-prepared suspension. This means that not all the nano-SiC particles were absorbed by Al powder even if the volume fraction of nano-SiC was as low as around 1%. Thus, this gentle mode of adding is not effective to trigger massive of hetero-agglomeration mixing.

Nevertheless, Fig. 4.22 shows that some small agglomerates of nano-SiC (indicated by black arrows) were still distributed on the surface of Al particles. Therefore, in order to make Al powder fully absorb the nano-SiC, the hetero-agglomeration process need to be completed once and the content of nano-SiC in the Al powder should be controlled lower than 1 vol.%, although some nano-SiC agglomerations would be delivered into the final powder mixture.

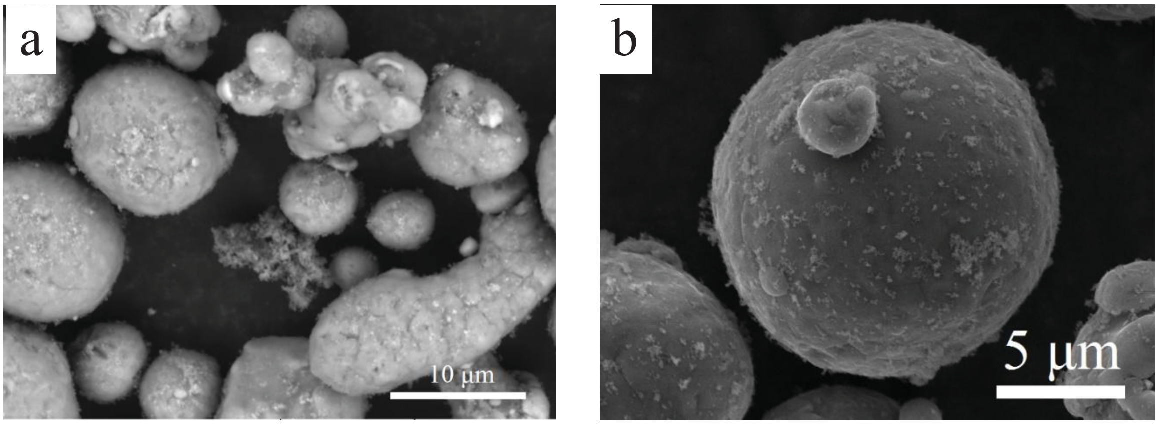

Fig. 4.21: SEM micrographs of the (a) morphology and (b) surface of the Al/nano-SiC composite powder prepared using the hetero-agglomeration method.

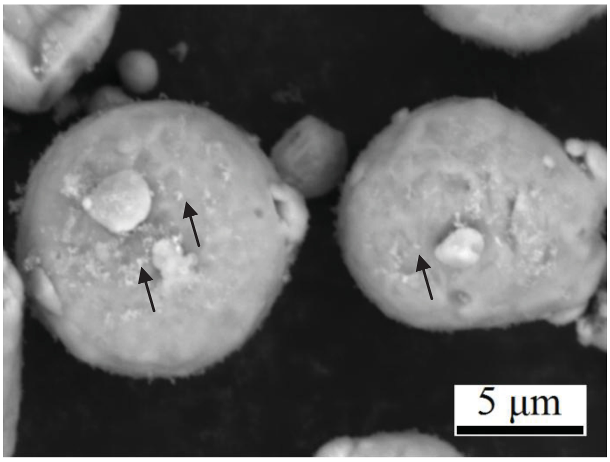

Fig. 4.22: SEM micrograph of the Al/nano-SiC composite powder prepared with the aid of peristaltic pump.

4.5.1.4 Ball milling process

The methods described above achieved the dispersion of nano-SiC on the surface of Al particles, and re-agglomeration of nano-SiC may still occur during the processing process. However, ball milling process can obtain a homogenous distribution of nanoparticles in the Al matrix, meanwhile and also avoid the occurrence of re-agglomeration [85]. In this section, ball milling process was applied to homogeneously distribute nano-SiC particles onto Al powders. Firstly, as-received nano-SiC was washed by HF, then, it was dispersed in isopropanol via ultrasound. The ball milling parameter was the same as mentioned in chapter 3. The content of nano-SiC in Al powder was fixed at 0.5 and 1 vol.%. Fig. 4.23 shows the surface morphology of the Al powder mixed with the different content of nano-SiC where the black arrows point out the distributed nano-SiC particles. The number and size of agglomeration on the surface of the Al powder became less and smaller, respectively, compared to the results in the section 4.5.1.3. With increasing the volume fraction of nano-SiC, apparently, there were more visible nano-SiC particles attached on the surface of the Al powder. Certainly, the initial spherical Al powder became the flake shape after ball milling process.

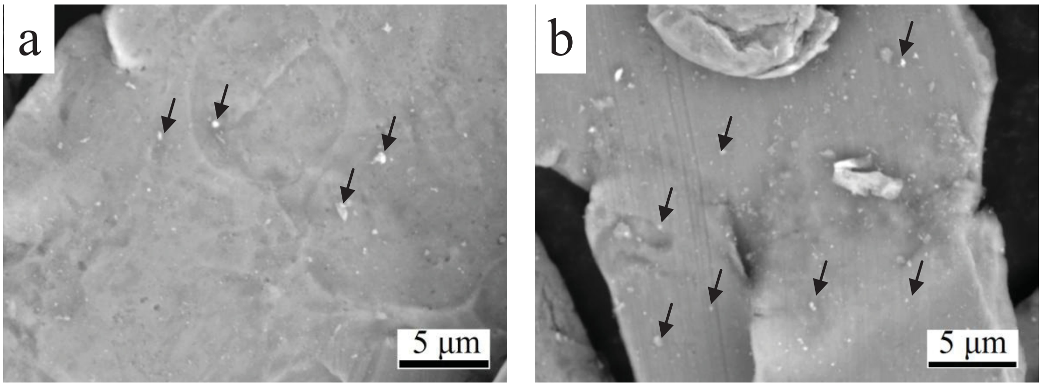

Fig. 4.23: SEM micrographs of the Al powder mixed with (a) 0.5 and (b) 1.0 vol.% nano-SiC via ball milling process (nano-SiC nanoparticles are pointed out by black arrows).

4.5.2 Flexural strength of the (Al/nano-SiC)/G_f composites

Regardless of the existence of small nano-SiC agglomerations on the surface of Al powder, the Al/SiC composite powder prepared by both hetero-agglomeration and ball milling processes were used to fabricate the (Al/SiC)/40 vol.% G_f composite parts in order to study their effects on final mechanical properties. Figs. 4.24a and b show the micrographs of the (Al/1 vol.% SiC)/G_f composites with the Al_S and Al_F matrices, respectively. The matrix microstructures are similar to those shown in Fig. 4.3 in size and architecture (i.e., equiaxed grain structure for the Al_S matrix and lamellar structure for the Al_F matrix). The SiC nanoparticles or agglomerations are distributed along the interparticle boundaries for both samples, and none of SiC is found within the grains.

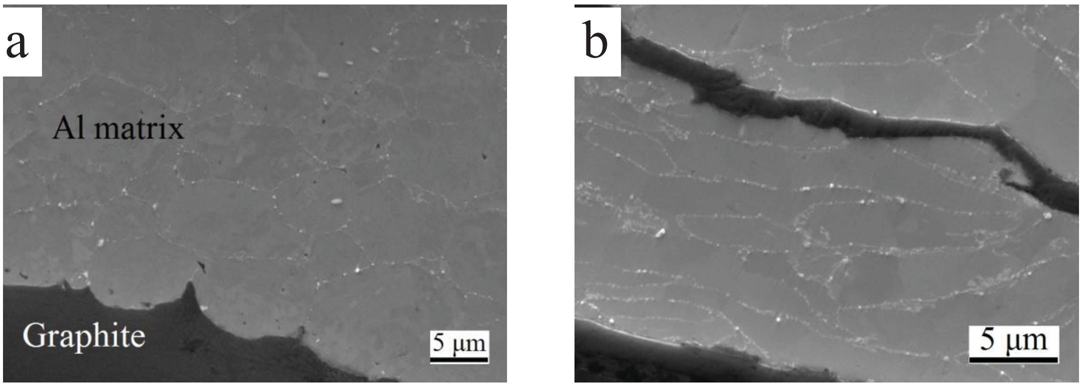

Fig. 4.24: SEM micrographs of the (Al/1 vol.% SiC)/40 vol.% G_f composites: (a) the Al_S and (b) Al_F matrices.

The effect of the addition of nano-SiC into the Al matrix on the mechanical properties of the composites was clarified on the flexural stress-strain curves. As shown in Fig. 4.25, the flexural strengths decrease a little bit or didn't change after incorporating 1 vol.% nano-SiC in the Al_S matrix with and without 5 vol.% AlSi, and the elongation decreased for both samples. The relative density for both samples was around 98% being a little bit lower than that of the Al/G_f composite without SiC (99%).

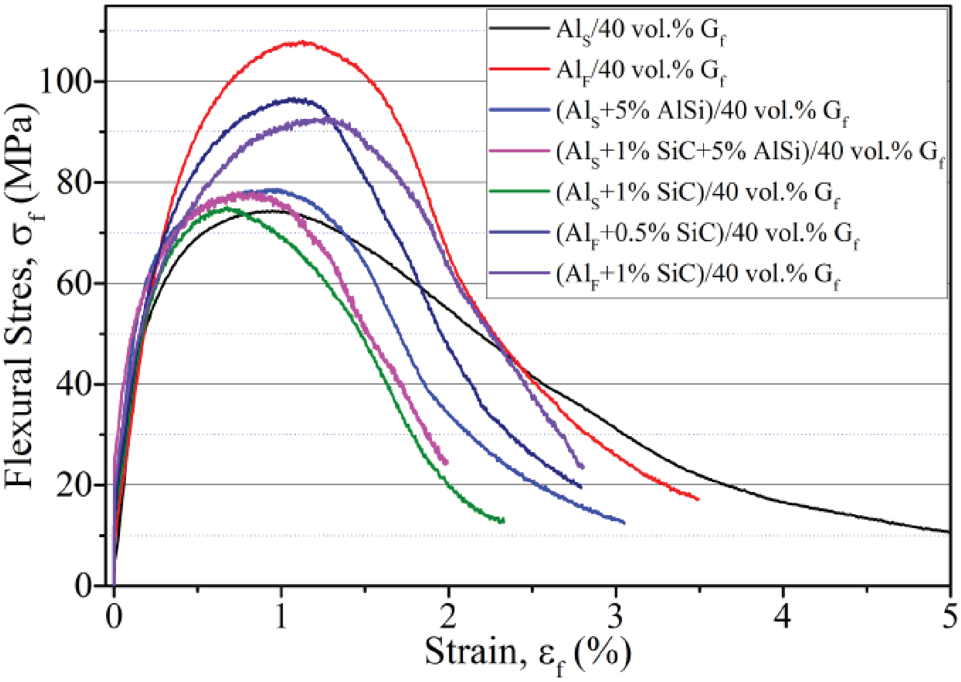

Fig. 4.25: Flexural stress strain curves of the (Al_S+1 vol.% SiC)/40 vol.% G_f, (Al_S+1 vol.% SiC+5% vol.% AlSi)/40 vol.% G_f, (Al_F +0.5 vol.% SiC)/40 vol.% G_f and (Al_F +1 vol.% SiC)/40 vol.% G_f composites (the curves from Al_S/40 vol.% G_f, Al_F/40 vol.% G_f and (5% vol.% AlSi/Al_S)/40 vol.% G_f composites act as the references).

Fig. 4.26 shows the side view of the fractured Al/G_f composites without and with 1 vol.% nano-SiC in the Al_S matrix. A transgranular fracture was observed in the Al matrix without nano-SiC. However, cracks occurred along the boundaries in the Al matrix with nano-SiC, and even some was distributed inside the matrix as pointed out by red circles. It suggests that the presence of SiC nanoparticles or clusters at the Al/Al interface decreases its load-bearing ability, thus, making it difficult to increase the mechanical strength.

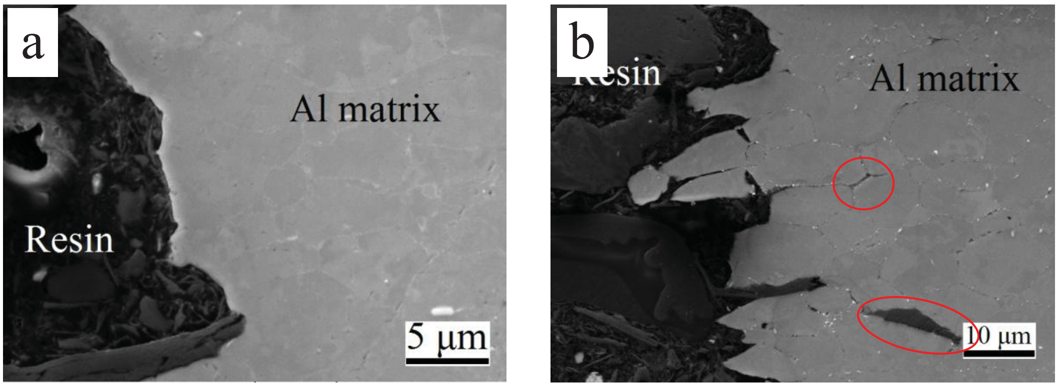

Fig. 4.26: SEM micrographs of side view of fracture in the Al/G_f composites: (a) Al_S/40 vol.% G_f, and (b) (Al_S+1 vol.% SiC)/40 vol.% G_f.

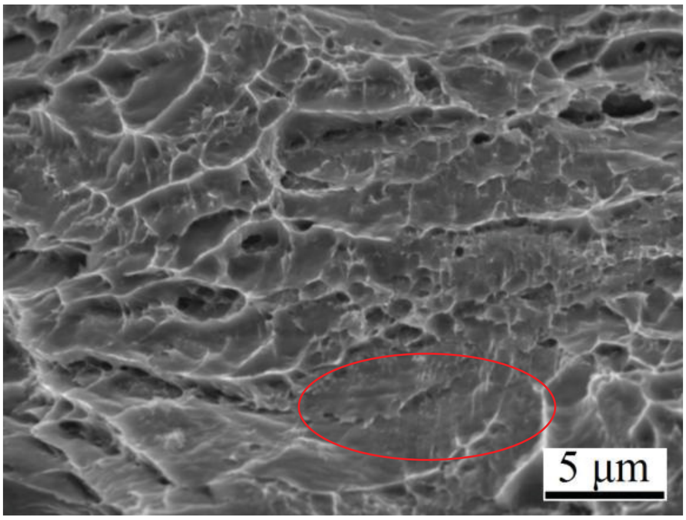

Fig. 4.27: SEM micrographs showing the fracture surfaces of the A_F matrix with 1 vol.% nano-SiC.

On the other hand, the presence of nano-SiC decreased the flexural strength of Al_F matrix compared with that of the pure Al_F matrix. Moreover, decrease the volume fraction of nano-SiC from 1 vol.% to 0.5 vol.% made it better in strength, but still lower than that of the pure Al_F matrix. Dimples was found in the fracture surface of (Al_F + 1 vol.% SiC)/40 vol.% G_f composite, while brittle fracture appeared in some region as indicated by red circle (Fig. 4.27).

4.6 Discussion

The above results show that the Al_F/G_f composite has the best mechanical performance, which benefits from the lamellar structure. According to our results, any addition of nanoparticles (SiC or TiB_2) into the Al_F matrix would weaken the mechanical strength to some extent. As for the in-situ nano-TiB_2, in fact, it was the dispersion of TiB_2 agglomeration other than individual nano-TiB_2 particles in the Al matrix, which decreases the effectiveness of the Orowan strengthening. Even though ball milling process can achieve the uniform dispersion of SiC nanoparticles, it was merely distributed along the interparticle boundaries and may decrease interfacial strength due to the existence of small agglomeration. On the other hand, lamellar structure can be regarded as an ideal model to achieve high strength and ductile, and any involvement of other phases may damage its integrity so as to affect its hardening mechanism. In fact, the nano-SiC was embedded in the Al_2O_3 lamella matrix, that would increase its brittleness as two materials are ceramics.

The addition of nano-SiC in the Al_S matrix had very limited or negative strengthening effect. One reason may be that the volume fraction of nano-SiC was too high to avoid local formation of agglomeration. In addition, the ex-situ route only disperses the nano-SiC on the surface of Al powder. When the Al particles coated by nano-SiC compacted for sintering, it is actually the densification of SiC nanoparticles at the interface zones, where the sintering temperature of 620 °C is insufficient to complete this process. Thus, it leads to brittle interfacial regions at the boundaries, and no strengthening can be expected.

4.7 Conclusion

Several strategies were attempted for improving the mechanical strength of the Al/G_f composites. Flake powder metallurgy was the most effective method to improve the strength of the Al matrix as it formed the unique lamellar structure compared with the other approaches, as shown in the **table 4.1**. Due to the agglomeration of nanoparticles during the process, it was proved that any addition of nanoparticles (SiC and TiB_2) in the Al_F matrix would decrease its strength.

Table 4.1 Flexural stresses of Al samples, Al/40 vol.% G_f composites, and Al (reinforced with nano-TiB_2 or nano-SiC)/40 vol.% G_f composites.

	Processes	**Flexural stress (MPa)**
Spherical Al	As sintered	179
Flake Al	As sintered	**315**
Al_S/5 vol.% AlSi10Mg&TiB_2	As sintered	192
Al_F/5 vol.% AlSi10Mg&TiB_2	As sintered	263
Al_S/40 vol.% G_f	As sintered	74
Al_F/40 vol.% G_f	As sintered	**107**
Al_S (AlSi10Mg&TiB_2)/40 vol.% G_f	As sintered	75
Al_F (AlSi10Mg&TiB_2)/40 vol.% G_f	As sintered	100
Al_F (0.5 vol.% nano-SiC)/40 vol.% G_f	Ball milling	95

Chapter 5

General conclusions and perspectives

5.1 General conclusions

The main objective of this thesis work was to develop G_f reinforced Al matrix composites (Al/G_f) with high TC, matched CTE with respect to the microelectronic chips, and enough strength to support the electronic component for potential thermal management applications in the microelectronic industry.

The Al/G_f matrix composites were fabricated using vacuum uniaxial hot pressing. It was found that the high in-plane TC of the oriented Al/G_f composites is linked to the fact that G_f has high TC along the in-plane direction (in the order of 1000 W/m.K). When a spherical Al powder was used as the matrix material, it was found that misalignment of G_f in the Al/G_f composites, prepared by the one-step powder filling, and applying uniaxial pressure leads to the relatively low in-plane TC of the composite. A step-by-step powder filling method was proved to be effective to achieve high alignment of G_f in the Al matrix whatever the shapes (sphere or flake) of the Al powder particles used. The orientation degree $<\cos^2\theta>$ of G_f, obtained by image analysis, was as high as 0.94, which is identical to that of the Al/G_f composite prepared by flake powder metallurgy.

It was also found that the in-plane TC of the 1D composite was increased by increasing the sintering temperature until 640 °C maintaining the high orientation degree of G_f ($<\cos^2\theta> = 0.94$). Also, the use of G_f, heat-treated in Ar + H_2 atmosphere, tends to increase TC of the composite material compare with those fabricated with non-treated G_f. The fact that the lattice parameter d_{002} of G_f maintains constant after heat treatment in Ar + H_2 atmosphere tend to prove that the intrinsic TC of G_f keeps unchanged by the heat treatment. The positive effects of both increase sinter temperature and use of treated G_f on TC of the Al/G_f composite materials are attributed to the optimization of the interfacial thermal conductance (ITC) between the Al matrix and G_f. The highest TC of the Al/40 vol.% G_f composite fabricated using our optimized condition is around 452 W/m.K, which is very close to the highest TC (456 W/m.K) theoretically predicted by EMA model considering the orientation degree of G_f (0.94), the intrinsic TC of the Al matrix (220 W/m.K) and G_f (1000 W/m.K), the geometry parameter of G_f (500 μm in diameter and 30 μm in thickness), and ideal thermal conductance

(4.6×10^9 W/m^2.K). Thus, for anisotropic reinforcement, both the orientation and interfacial states are critical to obtain a high TC of the MMC in preferred direction.

Conventionally, the 1D arrangement of G_f in the Al matrix has been established, while this composite exhibit high anisotropy in both TC and CTE unsuitable for heat sink applications. The CTE along the 45° direction was measured, which represents average performance of those along the in-plane and through-plane directions. We proposed a new architecture design (2D or 3D arrangements) of G_f in the Al matrix and achieved it via a novel processing method. This process combines fake powder metallurgy, specifically designed punch and step-by-step powder filling process. Use of flake Al powder enables the local arrangement of G_f as it has relatively low apparent density. In the 2D arrangement plane, the CTE values was tailored as low as $6 - 7 \times 10^{-6}$/K, and the TC along the direction perpendicular to the 2D arrangement plane is maintained as high as that of in-plane TC in the 1D arrangement. Thus, we can control the thermal performance (TC and CTE) of the Al/G_f composite in three dimensions by architecture design of G_f.

Finally, ex-situ, in-situ and bio-mimetic routes was attempted to improve the mechanical properties of the Al/G_f composite for meeting the needs of potential applications in the electronic packaging industry. Lamellar structure in the Al matrix established by fake powder metallurgy exhibited the best strengthening effect compared with the ex-situ and in-situ routes, where flexural strength can reach 107 MPa for the Al/40 vol.% G_f composite.

5.2 Perspectives

5.2.1 Measurement of interfacial thermal conductance

In chapter 2, the in-plane TC has been improved further by both increasing the sintering temperature and using heat treated G_f. This improvement is linked to the ITC, while its mechanism is still unclear. One should find an appropriate method to measure ITC of the Al/G_f composites fabricated at the different sintering temperatures, and this value can be useful for theoretical predication. On the other hand, in-depth interface analysis of the Al/G_f composites can be carried out to advance the understanding of the relationship between interface structure and ITC, again still unclear so far.

5.2.2 Thermal cycling test of the Al/G_f composites

In service, the thermal management material will experience thermal cycling and the thermal properties may degrade after long time of use. It is thus of importance to examine the thermal performance of the Al/G_f composites after thermal cycling.

The temperature range of thermal cycle can be -45 °C – 150 °C, and the cycle is repeated 100, 200, 500, and 1000 times. After each series, thermal diffusivity will be measured to determine the evolution of TC of the composites. Moreover, a de-lamination at the Al-G_f interface may occur after thermal cycling due to the poor bonding state between the matrix and reinforcement. Thus, it is interesting to find this local proof by microstructure characterization and try to enhance interface strength in order to increase the lifetimes (e.g. using semi-liquid route process).

5.2.3 Numerical simulation of CTE behaviours of the Al/G_f composites

Until now, there have been no reliable models to predict counterintuitive CTE behaviours of the Al/G_f composite. Numerical technique provides a solution to predict the physical behaviour of the composites using the finite element method. Comsol Multiphysics, as a commercial software package, has various modules covering a wide range of physical analyses. One of those modules can be used to study thermal stress distribution in the Al/G_f composite during heating and cooling.

5.2.4 Architecture design of G_f

Thermal design of heat sink materials focuses on increasing the TC along the direction perpendicular to the semiconductor chip surface and keeping the low CTE matching that of the semiconductor chip surface. However, the present 2D arrangement achieved isotropic CTE in x-z plane and high TC along the y direction (Fig. 5.1a), while the area of x-z plane is usually unable to cover the normal Si chip on the CPU (e.g. 150 mm^2 for AMD RYZEN 4000). Regarding this issue, the punch should be designed to array the G_f along the pressing direction to form the zigzag distribution of G_f on the x,y plane, as shown in Fig. 5.1b. Although G_f would rearrange during hot pressing, the extent of this rearrangement can be controlled in a small range via the design of punch. Thus, both high TC along the pressing direction and the isotropy in CTE in the x,y plane can be obtained, and the area of the x-y plane can cover the common Si chip. In addition, 3D arrangement can be fabricated via changing the orientation direction of groove on the punch, as illustrated in Fig. 5.2. It need to be noticed that the pressing process should be symmetrical with one of directions in order to keep the stress balanced. Moreover, we could fabricate multi-type materials, in which we can change the geometry, thickness, and material selections of each layer, as shown in Fig. 5.3. Thus, it is necessary to establish the relationship between the properties and multi-type materials applying macro numerical simulation. It would open a new door to fabricate materials using powder metallurgy.

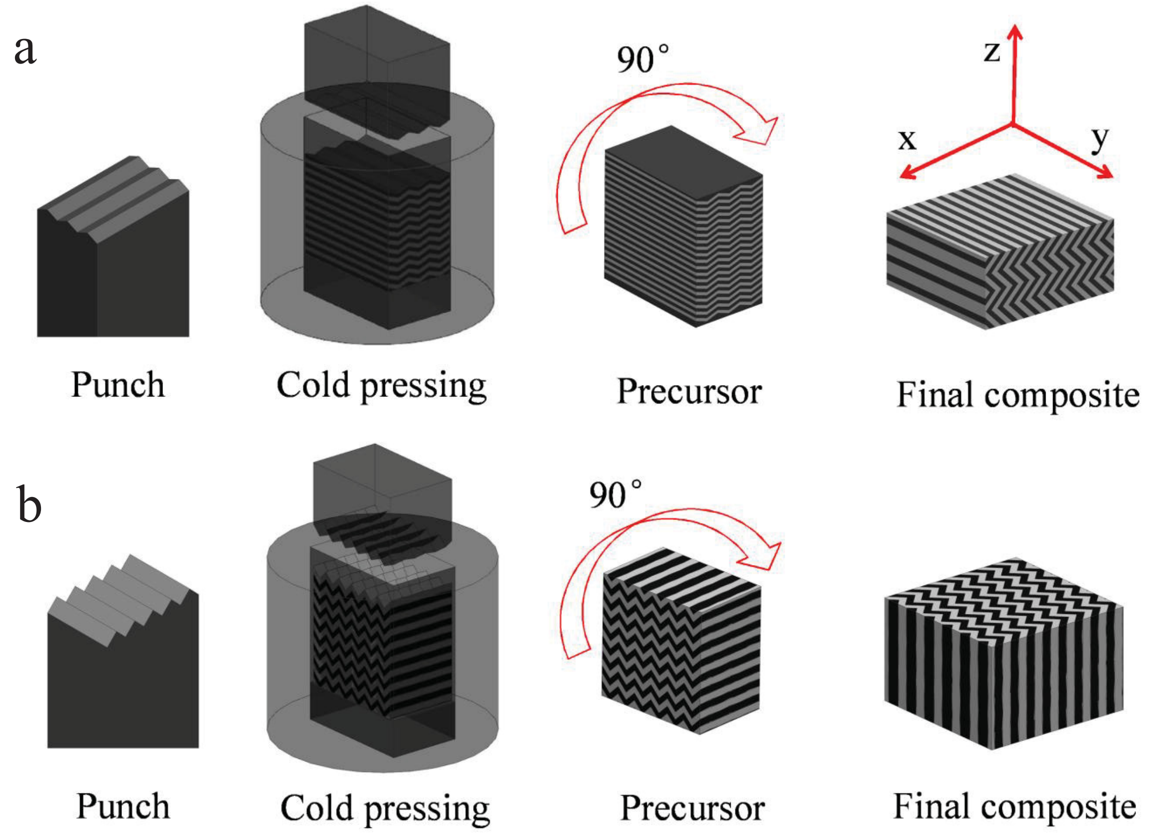

Fig. 5.1: Schematic illustrations of proposed process in controling the arrangement of G_f: (a) perpendicular to pressing direction, (b) along the pressing direction.

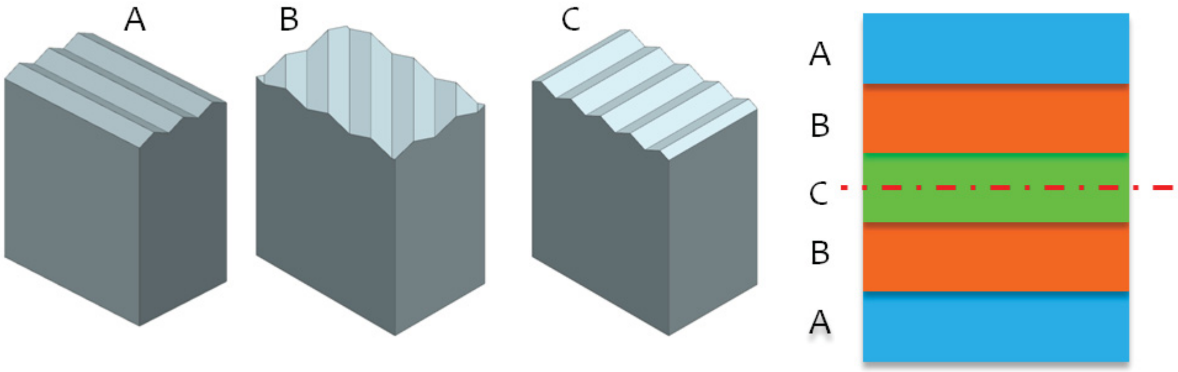

Fig. 5.2 : Schematic illustrations of proposed process in controling the arrangement of G_f by changing the alignment of groove on the punch.

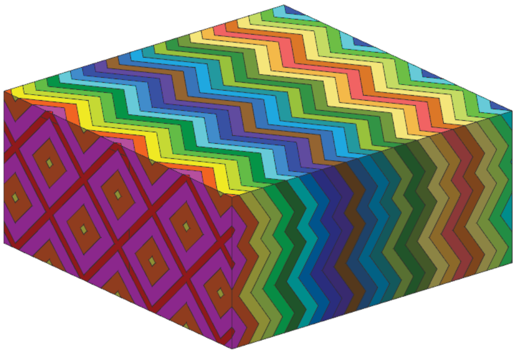

Fig. 5.3 : One possible design of multi-type materials (different colors represent different materials, such as Al/G_f, Cu/G_f, Al/CF, and Cu/CF).

References

[1] Burks A, Burks A. The First Electronic Computer: University of Michigan Press, 1988.

[2] Moore GE. Electronics 1965;38.

[3] Waldrop MM. Nature 2016;530:144.

[4] Viswanath R, Wakharkar V, Watwe A, Lebonheur V. 2000.

[5] Ball P. Nature 2012;492:174.

[6] Hannemann RJ. Thermal control of electronics: Perspectives and prospects. 2004.

[7] Fuller SH, Millett LI. Computer 2011;44:31.

[8] Prasher R. Proc. IEEE 2006;94:1571.

[9] Hamidnia M, Luo Y, Wang XD. Appl. Therm. Eng. 2018;145:637.

[10] Hanif A, Yu Y, DeVoto D, Khan F. IEEE Trans. Power Electron. 2019;34:4729.

[11] Ciappa M. Microelectron. Reliab. 2002;42:653.

[12] Che FX. IEEE Trans. Device Mater. Reliab. 2017;17:298.

[13] Tong XC. Advanced Materials for Thermal Management of Electronic Packaging: Springer, 2011.

[14] George E. Totten DSM. Handbook of Aluminum Volume 2: Alloy Production and Materials Manufacturing: CRC Press, 2003.

[15] Pickens JR. Journal of Materials Science 1981;16:1437.

[16] Ünal A. Powder Metall. 2013;33:53.

[17] PK Samal JN. ASM Handbook, Volume 7: Powder Metallurgy: ASM International, 2015.

[18] Ricks RA, Adkins NJE, Clyne TW. Powder Metall. 1986;29:27.

[19] Ünal A. Mater. Sci. Technol. 2013;3:1029.

[20] Molina JM, Piñero E, Narciso J, García-Cordovilla C, Louis E. Curr. Opin. Solid State Mater. Sci. 2005;9:202.

[21] Zhu Z, Kuang X, Carotenuto G, Nicolais L. Journal of Materials Science 1997;32:1061.

[22] Khalid FA, Beffort O, Klotz UE, Keller BA, Gasser P. Diamond Relat. Mater. 2004;13:393.

[23] Prieto R, Molina JM, Narciso J, Louis E. Scr. Mater. 2008;59:11.

[24] Prieto R, Molina JM, Narciso J, Louis E. Composites Part A: Applied Science and Manufacturing 2011;42:1970.

[25] Zhou C, Ji G, Chen Z, Wang M, Addad A, Schryvers D, Wang H. Materials & Design 2014;63:719.

[26] Clyne TW. 2018:188.

[27] Etter T, Schulz P, Weber M, Metz J, Wimmler M, Löffler JF, Uggowitzer PJ. Materials Science and Engineering: A 2007;448:1.

[28] Chen JK, Huang IS. Composites Part B: Engineering 2013;44:698.

[29] Lalet G, Kurita H, Miyazaki T, Kawasaki A, Silvain J-F. Journal of Materials Science 2014;49:3268.

[30] Murakami M, Nishiki N, Nakamura K, Ehara J, Okada H, Kouzaki T, Watanabe K, Hoshi T, Yoshimura S. Carbon 1992;30:255.

[31] Fu Q, Yang J, Chen Y, Li D, Xu D. Appl. Phys. Lett. 2015;106:031905.

[32] Nelson JB, Riley DP. Proceedings of the Physical Society 1945;57:477.

[33] Kurita H, Miyazaki T, Kawasaki A, Lu Y, Silvain J-F. Composites Part A: Applied Science and Manufacturing 2015;73:125.

[34] Jang J-H, Park H-K, Lee J-H, Lim J-W, Oh I-H. Composites Part B: Engineering 2020;183:107735.

[35] Chen J, Ren S, He X, Qu X. Carbon 2017;121:25.

[36] Firkowska I, Boden A, Boerner B, Reich S. Nano Lett. 2015;15:4745.

[37] Zhang C, He X, Liu Q, Ren S, Qu X. J. Compos. Mater. 2014;49:3323.

[38] Chamroune N, Mereib D, Delange F, Caillault N, Lu Y, Grosseau-Poussard J-L, Silvain J-F. Journal of Materials Science 2018;53:8180.

[39] Wang C, Bai H, Xue C, Tong X, Zhu Y, Jiang N. RSC Advances 2016;6:107483.

[40] Xue C, Bai H, Tao PF, Wang JW, Jiang N, Wang SL. Materials & Design 2016;108:250.

[41] Zhu Y, Bai H, Xue C, Zhou R, Xu Q, Tao P, Wang C, Wang J, Jiang N. RSC Advances 2016;6:98190.

[42] Liu Q, He X-B, Ren S-B, Zhang C, Ting-Ting L, Qu X-H. J. Alloys Compd. 2014;587:255.

[43] Zhang R, He X, Chen H, Qu X. J. Alloys Compd. 2019;770:267.

[44] Cao H, Tan Z, Fan G, Guo Q, Su Y, Li Z, Xiong D-B. Composites Part B: Engineering 2020;191:107965.

[45] Kai XZ, Li ZQ, Fan GL, Guo Q, Xiong DB, Zhang WL, Su YS, Lu WJ, Moon WJ, Zhang D. Materials Science and Engineering: A 2013;587:46.

[46] Nan C-W, Birringer R, Clarke DR, Gleiter H. J. Appl. Phys. 1997;81:6692.

[47] Sohn Y, Han T, Han JH. Carbon 2019;149:152.

[48] Reich S, Thomsen C. Philosophical transactions. Series A, Mathematical, physical, and engineering sciences 2004;362:2271.

[49] Bai H, Xue C, Lyu JL, Li J, Chen GX, Yu JH, Lin CT, Lv DJ, Xiong LM. Composites Part A: Applied Science and Manufacturing 2018;106:42.

[50] Xue C, Bai H, Tao PF, Jiang N, Wang SL. J. Mater. Eng. Perform. 2016;26:327.

[51] Li W, Liu Y, Wu G. Carbon 2015;95:545.

[52] Truong HV, Zinsmeister GE. Int. J. Heat Mass Transfer 1978;21:905.

[53] Oddone V, Boerner B, Reich S. Sci. Technol. Adv. Mater. 2017;18:180.

[54] Lacom W, Degischer HP, Schulz PA. Key Eng. Mater. 1996;127-131:679.

[55] Chamroune N, Delange F, Caillault N, Morvan F, Lu Y, Kawasaki A, Silvain J-F. Met. Mater. Int. 2019;26:155.

[56] Morvan A, Grosseau-Poussard J-L, Caillault N, Delange F, Roure S, Lepretre P, Silvain J-F. Composites Part A: Applied Science and Manufacturing 2019;124:105474.

[57] Ren S, Chen J, He X, Qu X. Carbon 2018;127:412.

[58] Liu B, Zhang D, Li X, He Z, Guo X, Liu Z, Guo Q. J. Alloys Compd. 2018;766:382.

[59] Zhang R, He X, Chen Z, Qu X. Vacuum 2017;141:265.

[60] Zhao Y, Ren S, Liu Q, Chen J, He X, Qu X. J. Alloys Compd. 2020;815:152425.

[61] Torquato S. Int. J. Solids Struct. 2000;37:411.

[62] Swartz ET, Pohl RO. Rev. Mod. Phys. 1989;61:605.

[63] Hasselman DPH, Johnson LF. J. Compos. Mater. 1987;21:508.

[64] Yang Y, Huang Y, Wu H, Fu H, Zong M. J. Mater. Res. 2016;31:1723.

[65] Tavangar R, Molina JM, Weber L. Scr. Mater. 2007;56:357.

[66] Hiroshi H, Minoru T. Int. J. Eng Sci 1986;24:1159.

[67] McCullough RL. Compos. Sci. Technol. 1985;22:3.

[68] Oddone V, Wimpory RC, Reich S. Journal of Materials Science 2018;54:1267.

[69] Kerner EH. Proc. Phys. Soc. London, Sect. B 1956;69:808.

[70] Turner PS. Journal of Research of the National Bureau of Standards 1946;37:239.

[71] Schapery RA. J. Compos. Mater. 2016;2:380.

[72] Oddone V, Reich S. physica status solidi (RRL) - Rapid Research Letters 2017;11:1700090.

[73] Oddone V, Segl J, Prakasam M, Hartmann MT, Silvain J-F, Edtmaier C, Reich S. Journal of Materials Science 2018;53:10910.

[74] Kumar N, Gautam G, Gautam RK, Mohan A, Mohan S. Journal of The Institution of Engineers (India): Series D 2015;97:233.

[75] Yang Y, Lan J, Li X. Materials Science and Engineering: A 2004;380:378.

[76] Lan J, Yang Y, Li X. Materials Science and Engineering: A 2004;386:284.

[77] Cao G, Kobliska J, Konishi H, Li X. Metallurgical and Materials Transactions A 2008;39:880.

[78] Chen LY, Xu JQ, Choi H, Pozuelo M, Ma X, Bhowmick S, Yang JM, Mathaudhu S, Li XC. Nature 2015;528:539.

[79] Zeng X, Liu W, Xu B, Shu G, Li Q. Metals 2018;8:253.

[80] Hou Y, Hu P, Han WB. Key Eng. Mater. 2012;512-515:779.

[81] Barick P, Prasad Saha B, Mitra R, Joshi SV. Ceram. Int. 2015;41:4289.

[82] Yang L, Wu X, Weng D. Colloids Surf., A 2006;287:16.

[83] Kurita H, Kwon H, Estili M, Kawasaki A. Mater. Trans. 2011;52:1960.

[84] Suryanarayana C. Prog. Mater Sci. 2001;46:1.

[85] Tang F, Hagiwara M, Schoenung JM. Materials Science and Engineering: A 2005;407:306.

[86] Kollo L, Leparoux M, Bradbury CR, Jäggi C, Carreño-Morelli E, Rodríguez-Arbaizar M. J. Alloys Compd. 2010;489:394.

[87] Mazahery A, Shabani MO. Transactions of Nonferrous Metals Society of China 2012;22:275.

[88] Yao X, Zhang Z, Zheng YF, Kong C, Quadir MZ, Liang JM, Chen YH, Munroe P, Zhang DL. Journal of Materials Science & Technology 2017;33:1023.

[89] Tjong S. Materials Science and Engineering: R: Reports 2000;29:49.

[90] Lakshmi S, Lu L, Gupta M. J. Mater. Process. Technol. 1998;73:160.

[91] Huang M, Li X, Yi H, Ma N, Wang H. J. Alloys Compd. 2005;389:275.

[92] Li XP, Ji G, Chen Z, Addad A, Wu Y, Wang HW, Vleugels J, Humbeeck JV, Kruth JP. Acta Mater. 2017.

[93] Prasad Reddy A, Vamsi Krishna P, Narasimha Rao R, Murthy NV. Materials Today: Proceedings 2017;4:3959.

[94] Carreño-Gallardo C, Estrada-Guel I, López-Meléndez C, Martínez-Sánchez R. J. Alloys Compd. 2014;586:S68.

[95] Tayeh T, Douin J, Jouannigot S, Zakhour M, Nakhl M, Silvain J-F, Bobet J-L. Materials Science and Engineering: A 2014;591:1.

[96] Liu X, Liu Y, Huang D, Han Q, Wang X. Materials Science and Engineering: A 2017;705:55.

[97] Orowan E. Institute of Metals, London 1948;451.

[98] Reddy MP, Shakoor RA, Parande G, Manakari V, Ubaid F, Mohamed AMA, Gupta M. Progress in Natural Science: Materials International 2017;27:606.

[99] Tan Z, Li Z, Fan G, Kai X, Ji G, Zhang L, Zhang D. Composites Part B: Engineering 2013;47:173.

[100] Lalet G, Kurita H, Heintz J-M, Lacombe G, Kawasaki A, Silvain J-F. Journal of Materials Science 2013;49:397.

[101] Kurita H, Feuillet E, Guillemet T, Heintz J-M, Kawasaki A, Silvain J-F. Acta Metallurgica Sinica (English Letters) 2014;27:714.

[102] Kang Q, He X, Ren S, Liu T, Liu Q, Wu M, Qu X. Mater. Charact. 2015;105:18.

[103] Molina JM, Louis E. Mater. Charact. 2015;109:107.

[104] Kai X, Li Z, Fan G, Guo Q, Tan Z, Zhang W, Su Y, Lu W, Moon W-J, Zhang D. Scr. Mater. 2013;68:555.

[105] Veillère A, Sundaramurthy A, Heintz JM, Douin J, Lahaye M, Chandra N, Enders S, Silvain JF. Acta Mater. 2011;59:1445.

[106] Azina C, Roger J, Joulain A, Mauchamp V, Mortaigne B, Lu Y, Silvain J-F. J. Alloys Compd. 2018;738:292.

[107] Tan Z, Li Z, Fan G, Guo Q, Kai X, Ji G, Zhang L, Zhang D. Materials & Design 2013;47:160.

[108] Osorio JG, Muzzio FJ. Powder Technol. 2015;278:46.

[109] Iwashita N, Park CR, Fujimoto H, Shiraishi M, Inagaki M. Carbon 2004;42:701.

[110] Badenhorst H. Carbon 2014;66:674.

[111] Howe JY, Rawn CJ, Jones LE, Ow H. Powder Diffr. 2012;18:150.

[112] Adams PM, Katzman HA, Rellick GS, Stupian GW. Carbon 1998;36:233.

[113] Maslova OA, Ammar MR, Guimbretière G, Rouzaud JN, Simon P. Phys. Rev. B 2012;86.

[114] Ferrari AC, Robertson J. Phys. Rev. B 2000;61:14095.

[115] Eckmann A, Felten A, Mishchenko A, Britnell L, Krupke R, Novoselov KS, Casiraghi C. Nano Lett. 2012;12:3925.

[116] Ferrari AC. Solid State Commun. 2007;143:47.

[117] Tuinstra F, Koenig JL. The Journal of Chemical Physics 1970;53:1126.

[118] Parker WJ, Jenkins RJ, Butler CP, Abbott GL. J. Appl. Phys. 1961;32:1679.

[119] Klemens PG, Pedraza DF. Carbon 1994;32:735.

[120] Chu K, Wang X-h, Wang F, Li Y-b, Huang D-j, Liu H, Ma W-l, Liu F-x, Zhang H. Carbon 2018;127:102.

[121] Zhou C, Huang W, Chen Z, Ji G, Wang ML, Chen D, Wang HW. Composites Part B: Engineering 2015;70:256.

[122] Etter T, Kuebler J, Frey T, Schulz P, Löffler JF, Uggowitzer PJ. Materials Science and Engineering: A 2004;386:61.

[123] Kuniya K, Arakawa H, Kanai T, Yasuda T. IEEE Transactions on Components, Hybrids, and Manufacturing Technology 1983;6:467.

[124] Nye JF. Physical Properties of Crystals: Their Representation by Tensors and Matrices, 1985.

[125] Strife JR, Prewo KM. J. Compos. Mater. 1979;13:264.

[126] Upadhyaya GS. POWDER METALLURGY TECHNOLOGY: Cambridge Int Science Publish, 1997.

[127] Ruffio E, Pradere C, Sommier A, Batsale J-C, Kusiak A, Battaglia J-L. Int. J. Therm. Sci. 2018;129:385.

[128] Jiang L, Li Z, Fan G, Zhang D. Scr. Mater. 2011;65:412.

[129] Fan G, Xu R, Tan Z, Zhang D, Li Z. Acta Metallurgica Sinica (English Letters) 2014;27:806.

[130] Mizuuchi K, Inoue K, Agari Y, Morisada Y, Sugioka M, Tanaka M, Takeuchi T, Tani J-i, Kawahara M, Makino Y. Composites Part B: Engineering 2011;42:825.

[131] Standard Test Methods for Flexural Properties of Unreinforced and Reinforced Plastics and Electrical Insulating Materials. ASTM D790-03. West Conshohocken: ASTM International, 2003

[132] Wu X, Yang M, Yuan F, Wu G, Wei Y, Huang X, Zhu Y. Proc Natl Acad Sci U S A 2015;112:14501.

[133] Xie X, Chen C, Chen Z, Wang W, Yin S, Ji G, Liao H. Composites Part B: Engineering 2020;202:108404.

[134] Wildhack S, Aldinger F. Key Eng. Mater. 2006;314:33.

[135] Estili M, Kawasaki A. Scr. Mater. 2008;58:906.

[136] Estili M, Kawasaki A, Sakamoto H, Mekuchi Y, Kuno M, Tsukada T. Acta Mater. 2008;56:4070.

Publication

Z. Shen, G. Ji, J.-F. Silvain, From 1D to 2D arrangements of graphite flakes in an aluminium matrix composite: Impact on thermal properties, Scripta Materialia 183(2020) 86-90. Doi:10.1016/j.scriptamat.2020.03.022